Graduate Theses and Dissertations   Graduate School

11-13-2017

Development MEMS Acoustic Emission Sensors

Adrian Enrique Avila Gomez
University of South Florida, aeavilag@gmail.com

Follow this and additional works at: https://scholarcommons.usf.edu/etd

Part of the Electrical and Computer Engineering Commons, and the Mechanical Engineering Commons

Development MEMS Acoustic Emission Sensors

by

Adrian Enrique Avila Gomez

A dissertation submitted in partial fulfillment
of the requirements for the degree of
Doctor of Philosophy
Department of Electrical Engineering
College of Engineering
University of South Florida

Co-Major Professor: Jing Wang, Ph.D.
Co-Major Professor: Rasim Guldiken, Ph.D.
Shengqian Ma, Ph.D.
Arash Takshi, Ph.D.
Sylvia Thomas, Ph.D.

Date of Approval:
November 7, 2017

Keywords: Microelectromechanical Systems, Damping, Capacitive, Simulation,
Modeling, Microfabrication

DEDICATION

First and foremost, I would like to dedicate this dissertation to God for giving me strength throughout this program. I also dedicate this work to my wife Viviana Sampayo who has encouraged me all the way during this long process, and to my precious daughter, Antonella Avila-Sampayo for bringing relief and joy to my life.

ACKNOWLEDGMENTS

TABLE OF CONTENTS

LIST OF TABLES

LIST OF FIGURES

ABSTRACT

The purpose of this research is to develop MEMS based acoustic emission sensors for structural health monitoring. Acoustic emission (AE) is a well-established nondestructive testing technique that is typically used to monitor for fatigue cracks in structures, leaks in pressurized systems, damages in composite materials or impacts. This technology can offer a precise evaluation of structural conditions and allow identification of imminent failures or minor failures that can be addressed by planned maintenances routines. AE causes a burst of ultrasonic energy that is measured as high frequency surface vibrations (30 kHz to 1 MHz) generated by transient elastic waves that are typically emitted from growing cracks at the interior of the structure.

The AE sensor marketplace is currently dominated by bulky and expensive piezoelectric transducers that are wired to massive multichannel data acquisition systems. These systems are complex to operate with the need of signal conditioning units and near proximity pre-amplifiers for each sensor that demands a fairly complicated wiring requirements. Furthermore, due to the high prices of conventional AE sensors and associated instrumentation, and the current requirements in sensor volumes for smart transportation infrastructure, it is undeniable that new AE technology is required for affordable structural health monitoring. The new AE technology must deliver comparable performance at one or two orders of magnitude lower cost, size and weight. MEMS acoustic emission (AE) sensors technology has the potential to resolve several of these

traditional sensor's shortcomings with the advantage of possible integration of on-chip preamplifier while allowing substantially cost reduction due to the batch processing nature of MEMS technology.

This study will focus on filling some of the major existing gaps between current developments in MEMS acoustic emission sensors and commercial piezoelectric sensors, such as sensor size, signal-to-noise ratio (SNR), cost and the possibility to conform to sharply curved surfaces. Basically, it is proposed to develop a new class of micro-machined AE sensors or sensor arrays through strategic design of capacitive and piezoelectric MEMS sensors, which will focus on optimizing the following performance aspects:

• Creating geometric designs to manipulate the sensor resonant frequency and to optimize Q factor under atmospheric pressure and ambient environment.

• Developing a strategic selection of materials according to its acoustic impedance as insulator, structure and backing material.

• Developing strategies to improve the signal to noise ratio SNR with and without integrated amplification/signal processing.

• Performing a comparison between MEMS and commercial piezoelectric sensors.

CHAPTER 1: INTRODUCTION

1.1 Objective

This study aims to develop novel batch-producible MEMS acoustic emission (AE) sensors with comparable performance to that of traditional piezoelectric sensors, while offering reduced cost, size and weight and improved versatility. Consequently, this next generation AE technology could provide the asset owners with a powerful monitoring tool for real-time assessment of structural integrity by detecting the formation of cracks or corrosion issues.

The main objective of this research is to develop a set of micromachining process steps to produce capacitive MEMS AE sensors, within a frequency range between 100 kHz and 1 MHz. To accomplish this goal, this study designed and developed arrays of out-of-plane MEMS electrostatic resonators with narrow gap capacitive transducers and well-tailored operation (resonance) frequencies.

The performance of the proposed sensors will be benchmarked against the latest AE MEMS sensor developments that are available in the literature and as well as commercial piezoelectric sensors, using the reported AE parameters and damping behavior as the key figure of merit.

In order to optimize the performance of the proposed sensor, the following aspects will be studied:

- Geometric designs to manipulate the sensor resonance frequency.

• Multiplexed sensor arrays to boost the electric signal and strategic MEMS processing approach to reduce the intrinsic noise.

• Analysis of the intrinsic damping of out-of-plane capacitive electrostatic resonator on its performance as an AE sensor.

1.2 Motivation

Structural Health Monitoring (SHM) is the main structural engineering tool to prevent and mitigate premature structural damages. The potential ability of SHM systems to provide useful information that can avoid a catastrophic failure will have an important impact on public safety and economic investments. Modern sensing technologies can supply an enormous amount of information of structures conditions, but the added expenses need to be balanced with the benefits so that the owners and structures operators could agree to invest in these technologies.

One of the most popular tools for SHM of structures is the utilization of acoustic emission to determine if cracks are growing at the interior of a structure or to monitor its degree of deterioration.   Acoustic emissions are elastic waves of short duration and high-frequency content that are caused by emerging micro fractures in solids and other confined events like chemical corrosion and pressure leaks. Common AE transducers are piezoelectric, fiber optics sensor and laser interferometers which have the advantage of being contactless. However, none of them can compete with piezoelectric acoustic emission sensing systems widely utilized by field engineers regarding the cost.

MEMS technology and its inherent low-cost mass production characteristics have the potential to batch-produce AE sensors that are tailored for end applications in

2

structural health monitoring of concrete, steel, and composite structures and rotating machinery.

1.3 Overview

This work is divided into five chapters and two appendices. In Chapter 1 is the dissertation topic and the motivation for this research are introduced. In Chapter 2, the pertinent background on AE sensors is presented. Chapter 3 shows the modeling and simulation strategy for capacitive MEMS acoustic emission transducers; the results are validated by comparing the simulated response with the experimental behavior of a device from the literature. Chapter 4 describes the details of the AE sensor fabrication and the experimental results are presented in Chapter 5. Lastly, concluding remarks and recommendations for future work are given in Chapter 6.

CHAPTER 2: BACKGROUND

AE has drawn greater attention over other non-destructive testing (NDT) techniques due its capability to simplify data acquisition accompanied with its high sensitivity. This technology is able to detect AE events caused by micro-cracking in solid materials like metals and concrete as well as fiber breakage or matrix cracking in composite materials. The waveforms that are acquired contain information about the size, type, orientation and location of the AE sources. Hence, if this information is correctly analyzed and processed, it's possible to establish the amount and the type of damages within the structure. Furthermore, if this analysis is used to provide inputs for fracture mechanics models, then is possible to estimate the remaining life of the structure.

The first documented research regarding AE was done by Kaiser in 1950 [1], who reported that several metals that he examined have exhibited an emission phenome on. He concluded that the source of these acoustic vibrations was originated in the boundary interfaces of grains, that an amplitude and frequency spectrum exists and was correlated to the stress level. Subsequently, the potential of AE was recognized, and investigations to correlate it with plastic deformation and crack propagation were reported by Tatro and Liptay [2] [3]. By this time, the research on AE was limited to low frequencies in the 60 kHz range. Dunegan *et.al*, extended these studies into the 100 kHz to 1 MHz range, which was a significant breakthrough as it facilitated the practical application of AE by eliminating the need of sound proof facilities to acquire the acoustic signals [4].

2.1 Acoustic Emissions Testing Overview

Physically, an acoustic emission signal is a transient elastic wave that is produced by a release of energy from one or several localized sources [5]. As shown in Figure 1, an acoustic emissions measurement system requires at least two fundamental constituents: a) a material that undergoes sudden stress redistribution as a consequence of a material deformation, which act as a source; and b) transducers that gather the stress wave and generates a correlated electrical signal.
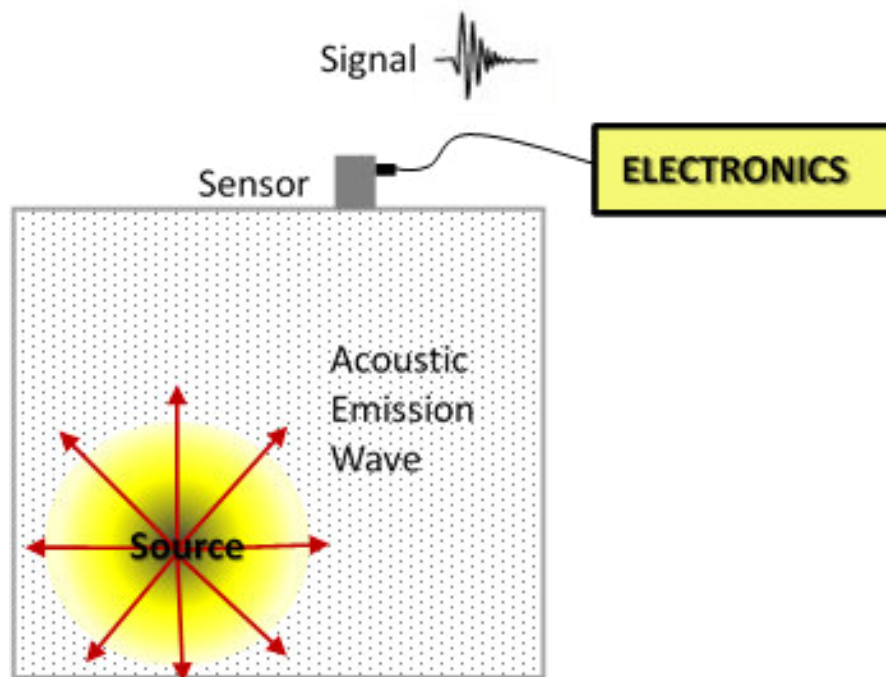
Figure 1. Basic principle of generation and detection of acoustic emissions.

The detection of an AE event is affected by the characteristics of the stress wave mode, the existence of multiple wave paths, wave propagation and attenuation. And the advanced algorithm has been used to determine the source location [6]. The AE based nondestructive testing has the following advantages and disadvantages [7]:

The advantages are:

• Possibility to examine large structures using only a small area to localize the sensor.

• The testing can be done during regular service to diminish down time.

• The structure evaluation and the damage location can be fulfilled in real time.

• Possibility to define the rate of damage and estimate the structure remaining life.

• The disadvantages are:

• The AE event is an irreversible process, which means that once one event is over the structure has to be exposed to higher load (stimuli) to generate another event.

• The quality of the information that can be gathered during a test is highly dependent on the background noise like friction, electromagnetic interferences or weather conditions.

• The need to have knowledge about the suspected crack locations and the load history to design a test in order to locate the sensor in a reasonable distance from the damage sources

• At least 2 sensors are required to perform a planar flaw location and 3 sensors for a 3D crack location.

2.1.1 Acoustic Emission Wave Characteristics

A usual AE wave is a mixture of transverse, longitudinal and reflected waves [8] and can be divided into two types: continuous and transient signals. Transient signals are also called bursts. And as can be seen in Figure 2 (a), a start and end points are evidently identifiable from background noise. Figure 2 (b) presents a continuous AE signal, it can

be noted that there are some frequency and amplitude variations but the signal don't have a clear ringing end.
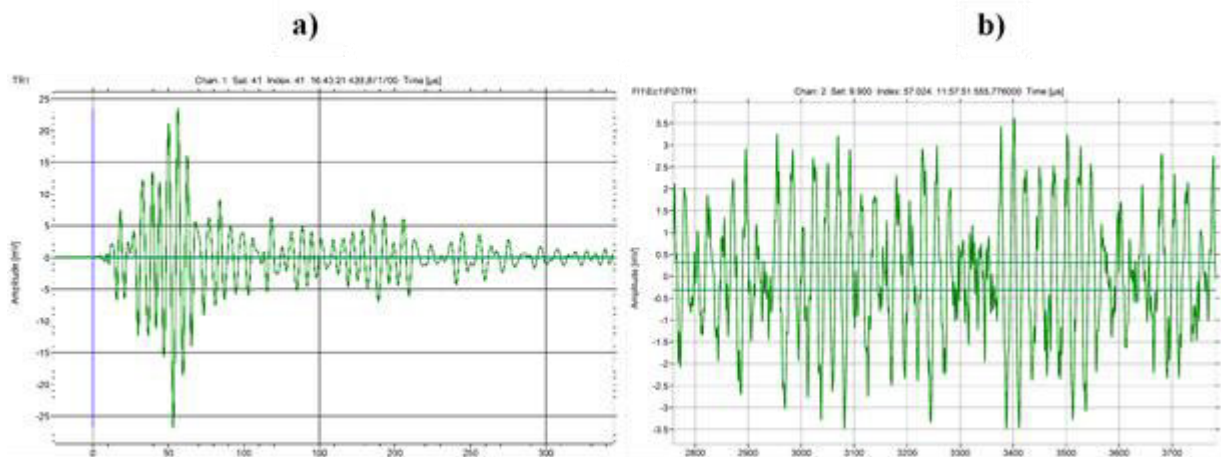
Figure 2. Waveforms of typical transient and continuous AE signals. Courtesy of Vallen Systeme GmbH.

During a testing procedure the transient AE signals are the useful wave types. Meanwhile the continuous signal is unwanted, because this type of AE is an indication of background noise such as friction or flow. So, the best noise existence scenario is when only the electrical noise from the amplifier is present [9]. But even under this ideal noise scenario, the background noise must be eliminated or minimized for the purpose of AE emissions analysis. To do this, the traditional AE emission systems are provided with signal processing algorithms to identify and manipulate the AE burst parameters. The key parameters are shown in Figure 2 and defined as the following [10]:

The Threshold is the blue line as shown in Figure 3. This parameter is determined by the operator and is the voltage level that needs to be exceeded to be considered as a

valid AE signal, when the AE transducer is triggered by an actual AE event. An AE signal exceeding the threshold is usually called a hit.

The Peak Amplitude is the maximum measured voltage in a waveform. This parameter determines the detectability of the AE signal.

The Rise Time is the time elapsed between the first time that the threshold is crossed and the moment the peak amplitude is reached. This parameter is a function of the wave propagation between the sensor and source, which is used as a measure of quality of the signal and can be a condition to filter noise.
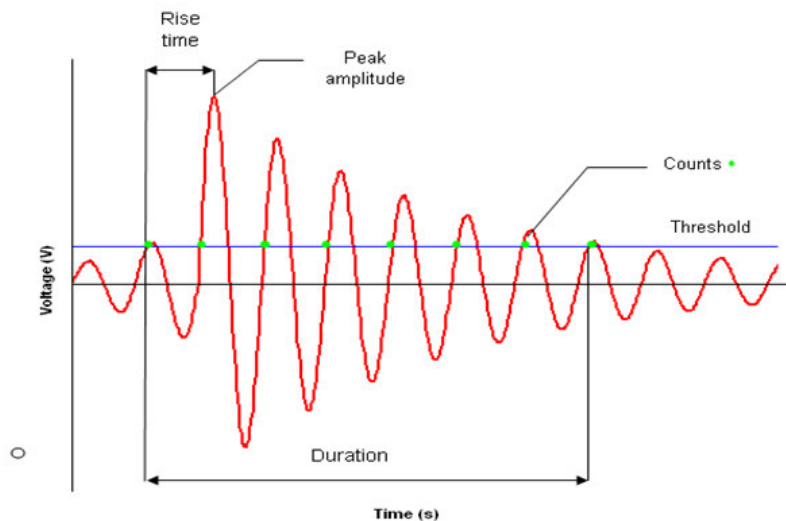
Figure 3. A conceptual illustration of all the key AE burst signal parameters [10].

The Duration is the time elapsed between the first time that the threshold is reached and the last time it is surpassed. This parameter can be also used to filter noise and to identify the type of source.

The Counts are the number of times that the threshold is crossed. This parameter in combination with the duration and the amplitude gives information about the quality of the signal.

8

Hence an acoustic emission testing scheme is being designed, these aforementioned parameters are preconfigured, followed by installation and calibration of the sensors. According to the calibration results and background noise, some parameters are adjusted and the test starts by recording each hit that the system collects. The system is also programed in such way that when consecutive hits within a specified time interval of Δt happen, the system record it and counted as one acoustic event. The time difference between the events registration on each sensor is used to localize the source via triangulation. When several events tend to cluster in a specific area, it is viewed as an indication of a growing flaw/cracks.

2.1.2 Commercial AE Sensor Characteristics

Acoustic emission sensors react to dynamic motion that is triggered by an acoustic emission event. To accomplish this, the sensor frame contains transducers that convert mechanical displacement into a measurable output electrical voltage signal. Commonly the transducer component (often in disk shape) is made of a piezoelectric crystal, such as lead zirconate titanate (PZT). The selection characteristics for these transducers are sensitivity, operating frequency (typically between 30 KHz and 1 MHz), and environmental characteristics. Usually, the sensitivity of these types of sensors can reach values on the orders of 1000V/µm. Hence, a displacement of 0.1 pm produces 100µVpk, which can be well differentiated from the electrical noise, that is typically around 10µVpk [9].

Figure 4 depicts the typical components that are included in an AE sensor [11]. As mentioned above, the core of these sensors is a thick and bulky piezoelectric disk that transforms a mechanical deformation into an electrical voltage. This element is attached to metal electrodes on both sides for electrical contact and usually the bottom electrode

is electrically connected with the metallic case to serve as ground and as electrical shielding. In order to optimize the sensitivity characteristic of the piezoelectric transducer element, it must be surrounded by a damping material, also called backing material, which offers specific mechanical and acoustic properties in order to provide structural support and selectable acoustic impedance to control reflections from the surface of the piezoelectric transducer. Additionally, a coupling material that is usually a thin gel layer used to enhance the acoustic coupling between the sample material and the sensor in order to eliminate or reduce the acoustic mismatch between them. In between the coupling material and the piezoelectric element, a wear plate is often introduced to avoid deterioration and contamination as can be seen in Figure 4.
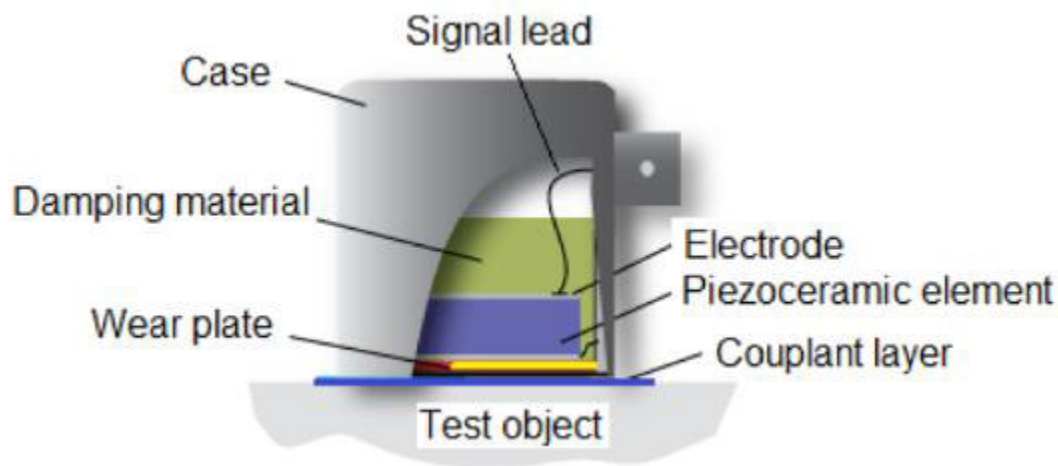
Figure 4. Configuration diagram of a commercial AE sensor [11].

2.1.3 The Drawbacks of the Commercial AE Sensors

The most commonly employed sensing mechanism in acoustic emissions systems is based on bulk piezoelectric transducers. This technology has been studied extensively.

Hence, its behavior and limitations are well understood. The most significant drawback of this technology is that it cannot be directly and easily integrated with the accompanying electronics. This is highly desirable from the signal-processing perspective to achieve monolithic integration with the signal-conditioning circuits on a single chip [12]. In current commercial AE technology, the electronic integration is achieved via cables that hinders the best achievable signal-to-noise ratio (SNR) and increases the onsite installation cost. Additionally, the traditional piezo-ceramic transducer technology for AE monitoring has the following constraints:

- Traditional piezo-ceramic sensors footprint is typically and approximately 1" (25.4 mm) in diameter and 1" in height, which makes it difficult to embed these AE sensors in structures for monitoring propose to be installed at high volumes.

- Current commercial sensor cannot discriminate between out-of-plane or in-plane AE signals due to its piezoelectric transduction mechanism. But, such an ability would be advantageous for damage characterization and damage location.

- Traditional piezoelectric materials cannot be used above 200°C.

- Traditional piezo transducers cannot be used in structures with complex shapes such as sharply curved surfaces or corners.

2.2 MEMS Acoustic Emissions Sensors Review

Some of the main concerns with regard to the traditional piezo-ceramic AE sensors lie in its high footprint that makes it difficult to be embedded in structures and its high cost (a single unit price between $300 and $500) that also prohibits high-volume installation. Micro-Electro-Mechanical-Systems (MEMS) technologies have the potential to mass-produce miniaturized, narrowband, acoustic emission transducers at low cost, which

11

cannot be achieved using conventional bulk piezoelectric transducers. Additionally, a MEMS AE sensor could have an electronic integration with amplifiers and antenna for remote monitoring, and more importantly, its small size could remove the aperture problem that exist between the size on the commercials piezoelectric sensors and the input signal wavelength. Several micro-machined AE sensors could be fabricated on the same chip and if they are designed for different resonance frequencies as an AE sensor array, Hence, it will be possible to detect acoustic emission signal at different frequencies, improving the data analysis capabilities to filter undesired noise signals and to have a better understanding of the source of the acoustic emissions events. .

The transduction mechanisms of the micro-machined MEMS transducers for acoustic emission detection applications can be either capacitive or piezoelectric.

2.2.1 Capacitive MEMS AE Sensors Review

There are several prior studies on using MEMS fabrication tecnology to produce AE capacitive transducers. The first reported work was done by Jones et.al [13]. They developed 1 mm^2 membranes using silicon nitride with capacitive gaps between 1 to 2 μm, which were used as capacitive AE transducers with resonacet frequencies between 100kHz to 250 kHz. The transducers were used to detect AE signals from composite materials in an aircraft and were able to detect a ball bearing drop and a pencil break at 13 cm distance from the mounted transducer.

In 2003 Oppenheim et.al, fabricated a phased array of polysilicon capacitive diaphragms designed for a resonance frequency of 5 MHz in air by using the PolyMUMPs (a multi-user shared MEMS foundry) [14]. The device was evaluated successfully to detect the distance and direction of an ultrasonic signal. In 2006 Ozevein et.al adapted

the geometric designs made by Oppenheim to develop capacitive MEMS AE transducer with resonant frequencies between 100 kHz to 500 kHz [15]. Arrays of 49-100 parallel plate capacitive transducers, with a total static capacitance between 30-40 pF, were fabricated using the PolyMUMPs process to obtain 1.25 µm gaps by using the dimple mask. The transducers were tested against traditional piezoelectric transducers, using a pre-cracked steel specimen during a four point bending test. As compared with commercial sensors, fewer (50%) AE events were detected due lower SNR caused by electrical interference. The MEMS AE sensors were 52 times less sensitive than commercial piezoelectric transducers.
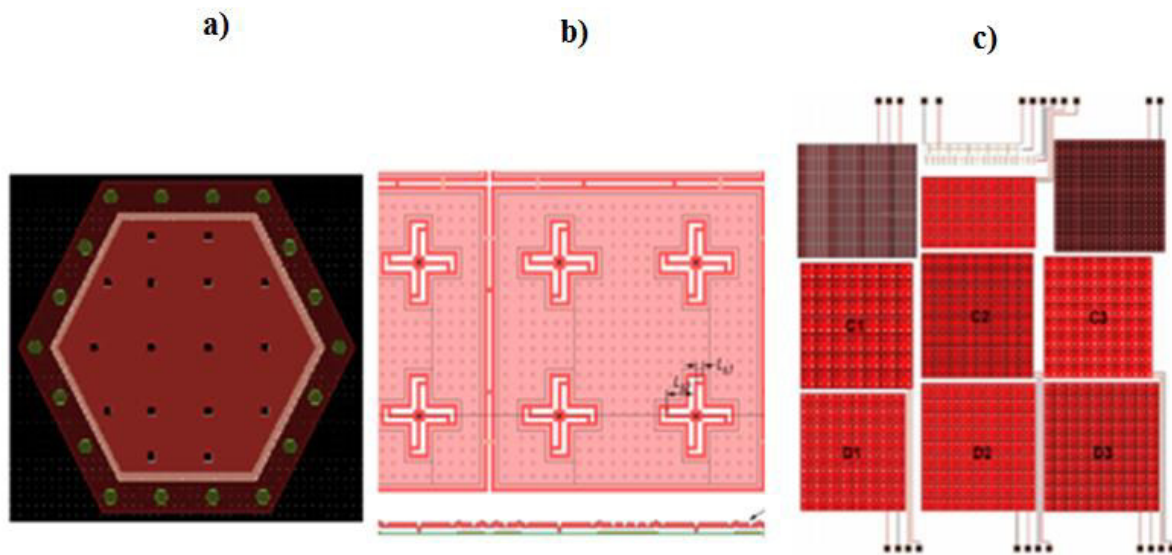
Figure 5. MEMS AE sensors designed by Ozevin with specially designed dimples [15].

Figure 5 shows the AE sensor designs, particularly the arrays of vertical capacitive transducers that were designed and tested by Ozevin et.al. [15] In particular, Fig. 5 (a) presents the top-view of an adapted diaphragm, which initially was used as an acoustic transducer, while Fig. 5(b) illustrates a spring type transducers and Fig. 5(c) shows the

arras layouts for the transducers. Later in 2007, Wu et.al also developed a resonant capacitive MEMS transducer using the PolyMUMPs process. This work has focused on means to diminish the squeeze-film damping and increase the Q factor compared with previous design [16]. Figure 3 presents the geometric design for the transducer with frequencies between 100 kHz and 500 kHz. The redistribution of the etching holes and the vacuum sealing of the device result in four fold increase in sensitivity compared to earlier designs.

In 2009, Wright et al. developed a MEMS chip that contains in-plane and out-of-plane capacitive MEMS transducers, in order to detect different wave modes for acoustic emission signals [17], [18]. As shown in Figure 7(a), the in-plane device was an open grill design and the out-of-plane one was a finger type design.
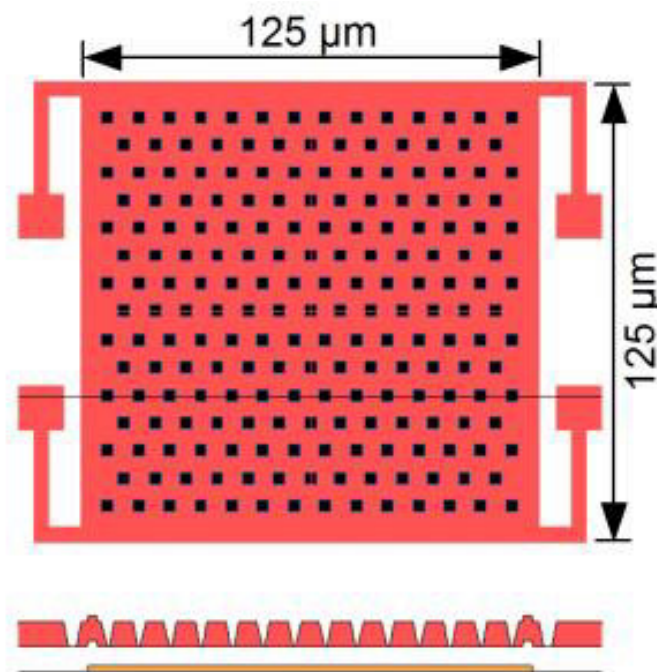
Figure 6. Illustration of vertical-gap MEMS AE sensors designed by Wu et al. [16]

The devices had resonance frequencies between 100 kHz to 500 kHz. Arrays of 144 out-of-plane transducers, 532 in- plane transducers, with a total static capacitance of 13 pF and 2.95 pF respectively, were fabricated using the PolyMUMPs process. Compared with the previous designs, the chip had an improved (vacuum sealed) package and amplifiers design. A noise analysis was performed to confirm that VRMS noise is independent of Q. The noise thus consists of a frequency independent component due to Johnson noise and a peaked component due to Brownian noise. And it was found that the main source of noise was the Amplifier. Furthermore, the open grill design had higher Q and sensitivity than others MEMS devices, which is still 24 times less than a commercial sensor. Nevertheless, the improved amplifier design reduced the sensitivity difference to 12 times. Figure 7(b), Illustrates the in-plane device that showed a long ringing response, which seems to be problematic.
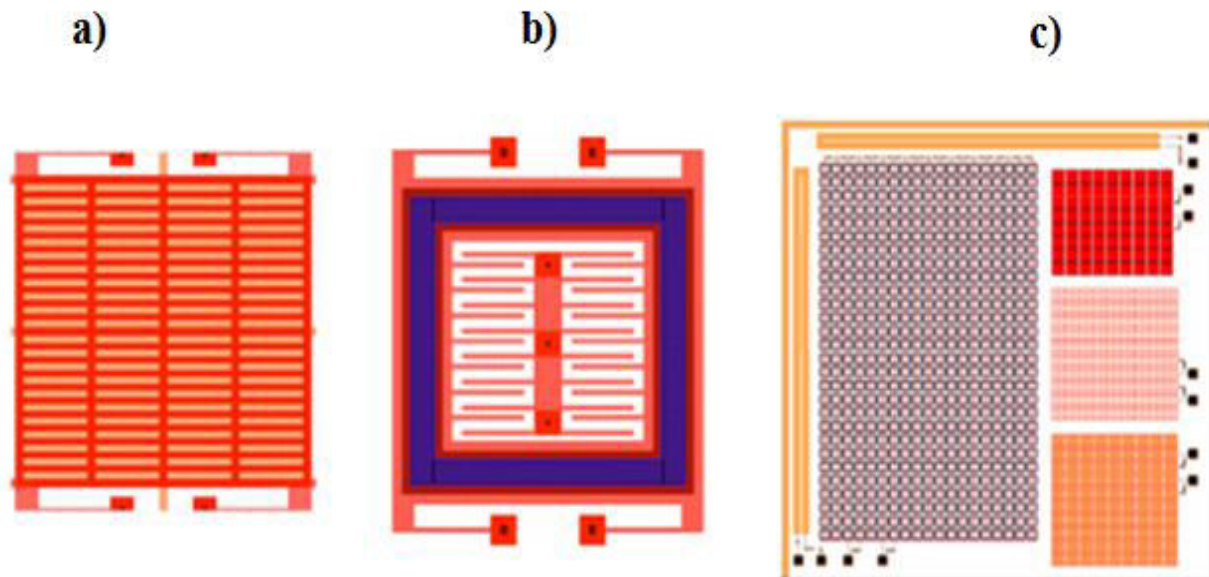
Figure 7. Illustration of MEMS AE sensors designed by Wright [17], [18].

In 2013, Saboonchi and Ozevin manufactured MEMS AE transducers of high aspect ratio by using the MetalMUMPs MEMS foundry process. Basically, they leveraged a thicker structural layer to increase the equivalent mass without over-dimensioning the planar size for low-frequency transducers while retaining the same spring coefficients. It is plausible to obtain higher spring coefficient at low resonance frequencies to enable application of higher DC voltages to increase the sensitivity. The devices had a resonance frequency between 50 kHz to 200 kHz. They made arrays of 55 transducers with a total static capacitance between 59 pF and 62 pF. Compared with the previous designs the total gap between the polysilicon layer (stationary layer) and the nickel layer (freely moving layer) is reduced to 1.45 µm (1.1 µm air and 0.35 µm silicon nitride). They also redesigned the anchor to reduce signal loss so that the devices don't require any amplifying circuitry or filtering. The sensors directionality was evaluated using a point source created by a short-pulse laser in the sensing direction. They report that for high frequency devices, the acoustic properties of the packaging structure play an important role with regards to its impact on sensitivity. Compared with commercial sensors, the MEMS devices had similar sensitivity and SNR. Figure 8 presents SEM photos of the AE sensor devices designed by Saboonchi and Ozevin [19].

2.2.2 Piezoelectric MEMS AE Sensors Review

There are only a few studies on micromachined AE piezoelectric transducers. In 1998, Polla & Francis integrated piezoelectric materials through MEMS processing technique for micro-sensor and micro-actuator applications, including AE sensing [20]. They used thin PZT films with thickness of 0.5 to 1 µm as the piezoelectric element and Ti/Pt as electrodes. The design frequencies were 50 kHz to 2 MHz. The AE sensors were

16

tested by minimizing the electromagnetic interferences while using the mechanical pencil break method. The measured peak voltage amplitude were 50 to 100 μV without external pre-amplification. Figure 9 shows a top-view SEM image of the PZT AE sensor.
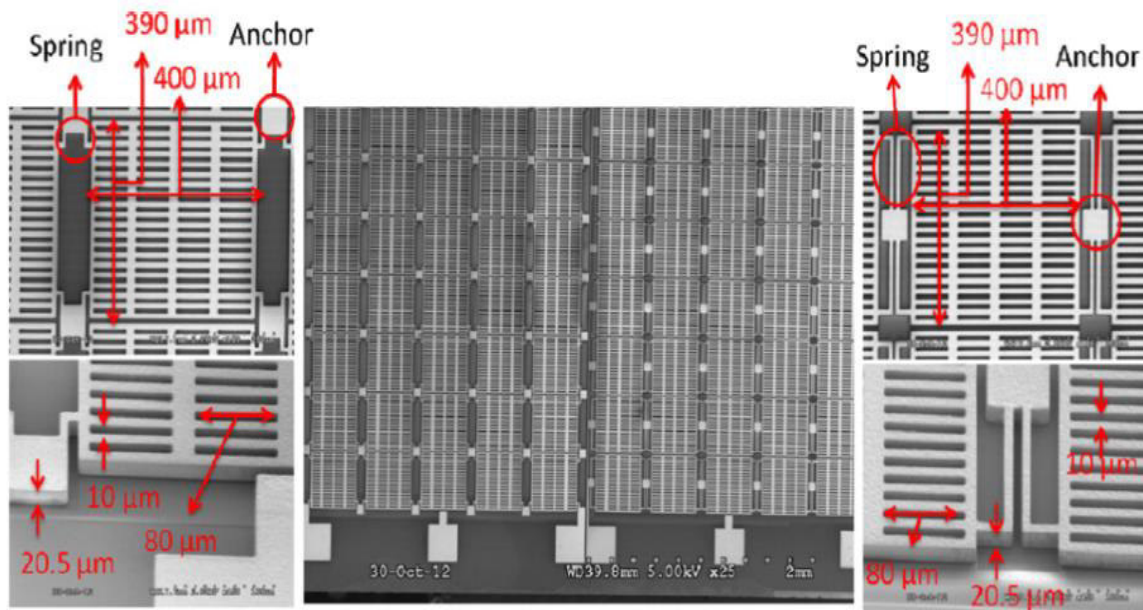
Figure 8. SEM photos of the MEMS AE sensors designed by Saboonchi and Ozevin [19].

In 2013, Chen and Shi used PZT nano active fiber composites, which were fabricated by an electrospinning process to obtain AE PZT nanofibers of approximately 80 nm in diameter [21]. According to the authors, the transverse piezo-coefficient d33 of PZT nanofiber is approximately 0.079 Vm/N, which is considerable higher than that of the bulk PZT or microfiber PZT of 0.025 Vm/N and 0.059 Vm/N, respectively. Figure 10 illustrates the basic sensor configuration and operation concept that consists of PZT nanofibers, gold interdigitate electrodes and a PDMS matrix. For AE testing they used a faraday cage to eliminate electromagnetic interference and used a steel bar to generate the AE signals that generated a maximum of 0.2V peak voltage.

17

Also in 2013, Pickwell et al. fabricated of a 4.4-μm-thick PZT film on a 110 μm-thick titanium foil substrate to be used as an acoustic emission sensor and its performance was compared with a commercial sensor [22]. The MEMS AE sensor had a resonant frequency around 320 MHz, while the commercial sensor had a frequency range between 250 kHz and 650 kHz. They made static measurements using the pencil break test and a dynamic one using a bearings test bed. The results showed a SNR of 3 for the static test and a SNR of 1 for the dynamic test. Figure 10 shows the MEMS sensor designed by Pickwell et.al.

2.2.3 Drawbacks in the Current Advances on MEMS AE Sensors

As mentioned above, the most common transduction mechanism used in MEMS AE sensor are capacitive and piezoelectric. The drawbacks and performance improvement opportunities will be discussed according to each sensing principle as follows:
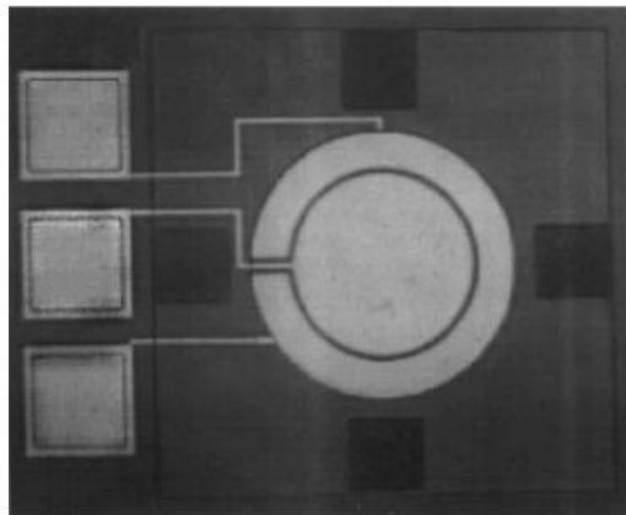
Figure 9. Top-view SEM image of the MEMS AE sensor designed by Polla and Francis [20].
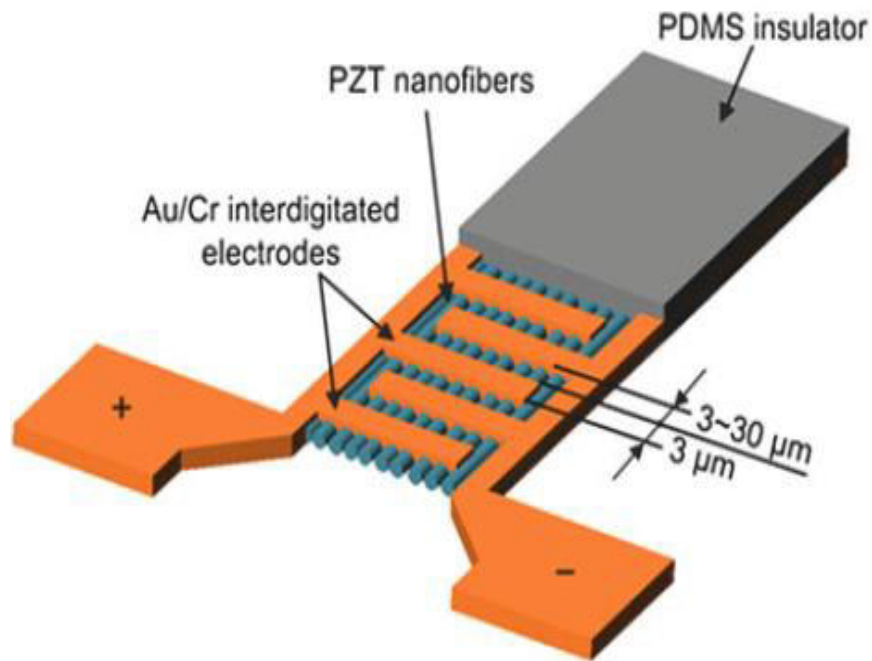
Figure 10. Conceptual illustration of the MEMS AE sensor designed by Chen and Shi [21].

The main shortcoming of the capacitive MEMS AE sensors is its limited SNR performance which is considerably lower than of the commercial piezoelectric sensors. Additionally, majority of the research in capacitive MEMS AE sensors is based on MEMS foundry processes such as PolyMUMPs or MetalMUMPs. The inherent design constraints of these foundry services limit the maneuverability of the designers with regard to materials selection, general process geometries and most importantly in terms of the signal strength that is determined by the minimal capacitive gap distance between the top and bottom electrodes in released and suspended parallel-plate membranes.

In the piezoelectric MEMS AE sensors the actuation and sensing characteristics are proportional to the transducer size, which hinders the performance of the miniaturized piezoelectric MEMS AE sensors as compared to the bulky commercial piezoelectric

19

devices. Nevertheless, the considerable smaller foot print of the MEMS devices make them an attractive alternative to allow AE technology to be deployed in applications for which the bulky commercial piezoelectric AE sensors are ill-suited [23], [24]. Moreover, there is a lack of research towards the addition of an acoustically matched backing material to improve the properties of the MEMS piezoelectric AE devices by reducing waveform reflections from the active boundaries.
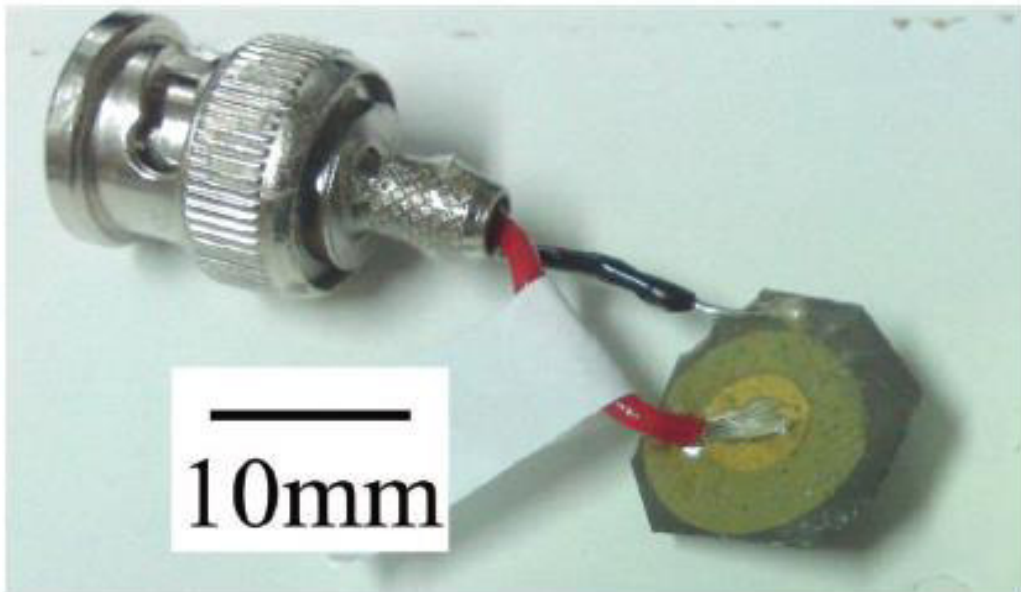
Figure 11. Photo of the MEMS AE sensor designed by Pickwell et al. [22].

2.3 Electromechanical Characteristic of Capacitive MEMS Resonators

Figure 12 illustrates the device configuration and the basic operation principle of a capacitive MEMS resonator that is used to detect acoustic emission signals. Basically, when an acoustic emission signal u(t) is generated due an energy release from a source inside of a material like localized stress energy release, the elastic wave produced cause a relative displacement x(t) of the bottom electrode with respect to the top electrode. If a

DC bias voltage (V_{dc}) is present between the electrodes, a time varying motional current i(t) is generated and can be converted to a time varying voltage v(t) to be detected and acquired later on [7].
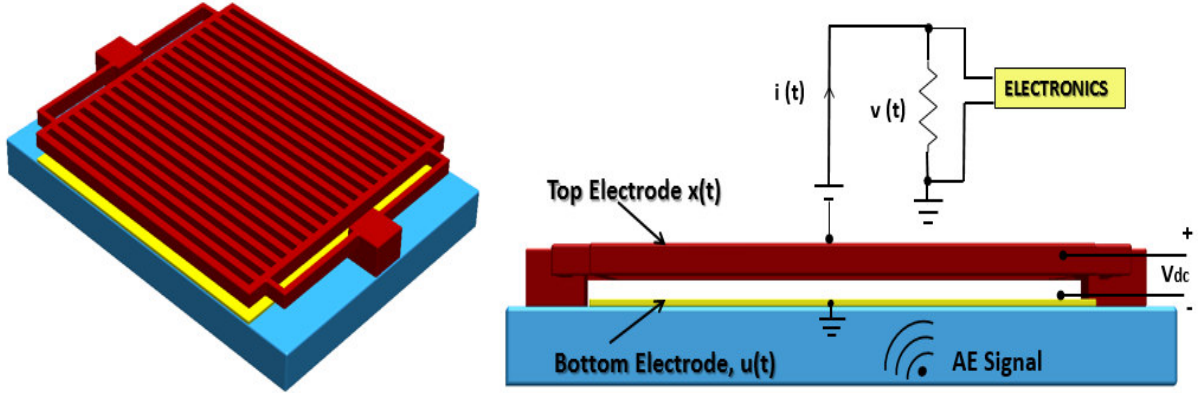
Figure 12. Schematic and cross-sectional diagrams of an open-grill shaped capacitive MEMS AE transducer.

This type of devices can be modeled as a lumped mass-spring-damper system that is governed by the following equation [7]:

$$\mathrm{m}\ddot{x} + c\dot{x} + kx - F_{elect} = -m\ddot{u} \tag{1}$$

where k is the spring constant, c is the damping coefficient, m is the mass and F_{elect} is electrostatic force that is generated between the two electrodes when de V_{dc} is applied. The resonance frequency is defines as:

$$\omega_0 = 2\pi f_0 = \sqrt{\frac{k}{m}}, [\frac{rad}{s}] \tag{2}$$

21

The dimensionless parameter quality factor that describes the damping characteristics is given by:

$$Q = \frac{m\omega_0}{c} \tag{3}$$

The capacitance that exist between the two parallel plates or bottom nad top electrode can be modeled by:

$$C = \frac{\varepsilon_0 A}{g - x} \approx \frac{\varepsilon_0 A}{g}\left(1 + \frac{x}{g}\right) \tag{4}$$

where A is the electrodes area, ϵ_0 is the permittivity of free space and g is the static gap between electrodes.

The electrical force F_{elect} can be defined as:

$$F_{elect} = -\frac{d}{dx}\left(\frac{1}{2}CVdc^2\right) = -\frac{1}{2}Vdc^2\frac{d}{dx}\left(\frac{\varepsilon_0 A}{g - x}\right) = \frac{1}{2}Vdc^2\frac{\varepsilon_0 A}{g - x} \tag{5}$$

for small gaps or $g \gg x$:

$$F_{elect} = \frac{1}{2}Vdc^2\frac{\varepsilon_0 A}{(g - x)^2} \tag{6}$$

By consideration Eq. (6) then Eq. (1) can be simplified to an expression that takes into account the inertial forces, the damping forces, the electrostatic forces and the acceleration of the structure's surface that is generated as consequence of the incoming acoustic emission waves.

The lumped mass-spring-damper system in Eq. (1) can be expressed as:

$$\text{m}\ddot{x} + c\dot{x} + kx - \frac{\varepsilon_0 A V dc^2}{2g^2} = -m\ddot{u} \tag{7}$$

According to this equation, the capacitive transducer can be under induced displacements in three cases:

1) Existence of a DC bias voltage with no mechanical excitation: Under this scenario, the displacement of the top plate can be described using Eq. 8.

$$\text{x} = \frac{\varepsilon_0 A V dc^2}{2kg^2} \tag{8}$$

then, replacing x in Eq. (4) the following is obtained:

$$\text{C} = \frac{\varepsilon_0 A}{g}\left(1 + \frac{\varepsilon_0 A V dc^2}{2kg^3}\right) = C_0 + C_1 V dc^2 \tag{9}$$

The static capacitance and C_1 can be expressed as:

$$C_0 = \frac{\varepsilon_0 A}{g}, and \; C_1 = \frac{C_0^2}{2kg^2} \tag{10}$$

2) If the electrostatic force is equal to the spring force, the voltage applied over the capacitance is at a point where if there is a small increase on its value, it will cause the

reduction of the distance between the parallel top and bottom electrode until they collapse and snap together.

The pull-in voltage given by:

$$V_{pull\ in} = \sqrt{\frac{8kg^3}{27\varepsilon_0 A}}$$ (11)

3) The existence of mechanical input: Under a mechanical input, the induced current will be equal to (the 1st and 2nd components are electrical and motional currents):

$$i(t) = \frac{dQ}{dt} = C\frac{dV}{dt} + V\frac{dC}{dt} = C\frac{dV}{dt} + \frac{Vdc\varepsilon_0 A}{g^2}\frac{dx}{dt}$$ (12)

2.4 Noise in MEMS Devices

Noise is often related to a random oscillation of molecules, atoms or electrons. The motion of these small particles results in a measurable noise at macro or micro-scale. Noise is an essential parameter to be considered in electronic designs, because it degrades the performance of electronic systems and limits the output of measurement systems like sensors. In general there are internal and external sources of noise. Internal sources are those correlated to the circuit under study, which are caused by resistors, transistor amplifiers, etc.; while the external sources are those introduced to the circuit by different means.

In micromechanical sensors and actuators, its performance can be degraded by mechanical and electrical input and output noise. The specific noise source depends on the characteristics and physics of the sensor or actuator. But for MEMS devices that

24

usually have static or movable elements at the micrometer scale, the mechanical-thermal noise is the main source that limits its performance. In fact, this type of noise defines the minimum tolerable size for these devices, even though the thermal noise energy is independent of the size of the system. As the devices reduce its size, the signal power is ordinarily lower while the noise level tends to increase. Consequently, the device signal have tendency to fall below the noise floor [25], [26], [27].

2.4.1 Statistical Representation of Noise

All the electronic systems has some degree of noise that can affect analog or digital circuits. The random characteristics of the noise makes it impossible to predict the instantaneous value of a measured signal. Nevertheless, it is possible to calculate the probability that a signal fall in a specific range. Majority of noise sources have a Gaussian probability distribution, then if voltage v_n is used as an example of electrical noise, its probability distribution will be:

$$f(v_n) = \frac{1}{v_{rms}\sqrt{2\pi}} e^{-\frac{v_n^2}{2v_{rms}}} \tag{13}$$

where v_{rms} is the standard deviation of the average voltage. Then the probability that the measured noise v_n is in between v_1 and v_2 is [28]:

$$P = \int_{v_1}^{v_2} f(v_n)\, dv_n \tag{14}$$

The mathematical definition for the root mean square voltage v_{rms} can then be given by Eq. 15.

If several noise sources are present, then these must be summed according to its correlation. For instance for uncorrelated sources the following Eq. 16 can be used.

$$v_{rms} = \lim_{N\to\infty} \sqrt{\frac{1}{N}\sum_{n=1}^{N} v_n{}^2} \tag{15}$$

$$v_{rms,tot} = \sqrt{v_{rms,1}{}^2 + v_{rms,2}{}^2 + \cdots + v_{rms,n}{}^2} \tag{16}$$

On the other hand, if the unwanted noise signals are from correlated sources Eq. (17) as below must be used.

$$v_{rms,tot} = v_{rms,1} + v_{rms,2} + \cdots + v_{rms,n} \tag{17}$$

Usually two noise signals are assumed to be uncorrelated, unless they are absolutely necessary.

2.4.2 Noise in Frequency Domain

In frequency domain a Gaussian noise usually assumed, because it facilitates its calculation and because this assumption can take into account the unknown nature of the noise. The rms noise represents the amplitude of the noise in the time domain, which does not give any information about its characteristics in frequency. This information is given by the power spectral density $\overline{v_n^2}$ and the spectral density $\overline{v_n} = \sqrt{\overline{v_n^2}}$. These parameters determines the average amount of noise per unit bandwidth on a specific frequency. The root mean square noise or rms noise can be related to the noise spectral density by Eq. 18.

In any real system, the measured noise is always shaped by its transfer function $H(f)$, then the measured noise is given by Eq. 19.

$$v_{rms} = \sqrt{\int \overline{v_n^2}(f)df} \tag{18}$$

$$\overline{v_{n,out}^2}(f) = |H(f)|^2 v_n^2 \tag{19}$$

where $H(f) = \frac{v_{out}}{v_{in}}$, then the output rms noise is given by:

$$v_{rms} = \sqrt{\int |H(f)|^2 \overline{v_n^2}(f)df} = \overline{v_n}\sqrt{\int |H(f)|^2 \, df} \tag{20}$$

The noise bandwidth can be modeled as:

$$BW = \frac{1}{|H_{pk}|^2}\int |H(f)|^2 \, df \tag{21}$$

where $|H_{pk}|$ is the peak value of the transfer function, and the v_{rms} noise is:

$$v_{rms} = |H_{pk}| \sqrt{BW} \, \overline{v_n} \tag{22}$$

2.5 Thermal Noise

Thermal noise is the intrinsic noise generated by thermal fluctuations generated by electrical or mechanical components of the system. This type of noise can be quantified using the equipartition theorem of thermodynamics. For each element that is

27

capable of storing energy independent of other variables (degree of freedom), the average thermal energy is $W = \frac{1}{2}k_B T$, where k_B is the Boltzmann constant.

2.5.1 Electrical Thermal Noise

The thermal noise is the electronic noise produced by the thermal agitation of the charge carriers inside an electrical conductor at equilibrium. Is usually called Johnson-Nyquist noise. It occurs regardless of the applied voltage and its degrees of freedom or energy storage elements is often determined by the number of independent capacitors plus the number of independent inductors. According to the equipartition theorem, the thermal energy stored in a capacitor is:

$$W_C = \frac{1}{2}C v_{rms}^2 = \frac{1}{2}k_B T \tag{23}$$

The rms noise voltage for a capacitor is also referred as kTC noise is given by:

$$v_{rms} = \sqrt{\frac{k_B T}{C}} \tag{24}$$

Similarly, for inductors the stored energy is:

$$W_I = L i_{rms}^2 = \frac{1}{2}k_B T \tag{25}$$

Then the rms noise current for the inductor is given by:

$$i_{rms} = \sqrt{\frac{k_B T}{L}} \tag{26}$$

28

In general, for electrical components, the noise frequency spectrum is defined by the damping condition of the system. Then the noise spectral density is related to each resistor by:

$$\overline{v_n^2} = 4k_B T R \tag{27}$$

2.5.2 Mechanical Thermal Noise

The thermal noise comes from mechanical components is usually known as Brownian noise. Similarly to the case for the electrical thermal noise, it depends on the energy-storing elements. MEMS resonators can be modeled as mass-spring-damper system as can be seen in Figure 13. In these systems, energy is stored as potential energy in the spring and kinetic energy in the mass.

Then based on the equipartition theorem, it is possible to define the rms noise displacement and velocity as follows:

$$W_{kin} = \frac{1}{2} m \dot{x}_{rms}^2 = \frac{1}{2} k_B T \tag{28}$$

$$W_{pot} = \frac{1}{2} k x_{rms}^2 = \frac{1}{2} k_B T \tag{29}$$

$$x_{rms} = \sqrt{\frac{k_B T}{k}} \tag{30}$$

Similar to that of the electrical thermal noise, the frequency content for the mechanical thermal noise is related with the damping as a force noise generator as is expressed in

Eq. 31. Where γ is the damping coefficient of the system, k_B is the Boltzmann constant ant T is the temperature.

$$\overline{F_n^2} = 4k_BT\gamma \tag{31}$$

2.6 Signal to Noise Ratio

In every electronic measurement system, it is important to achieve the lowest noise floor to maximize performance from the signal acquisition circuitry. Then is critical to measure and understand the noise sources in order to be able to attain a good resolution from small input signals. These sources can other electrical devices or external machines that generate mechanical noise.
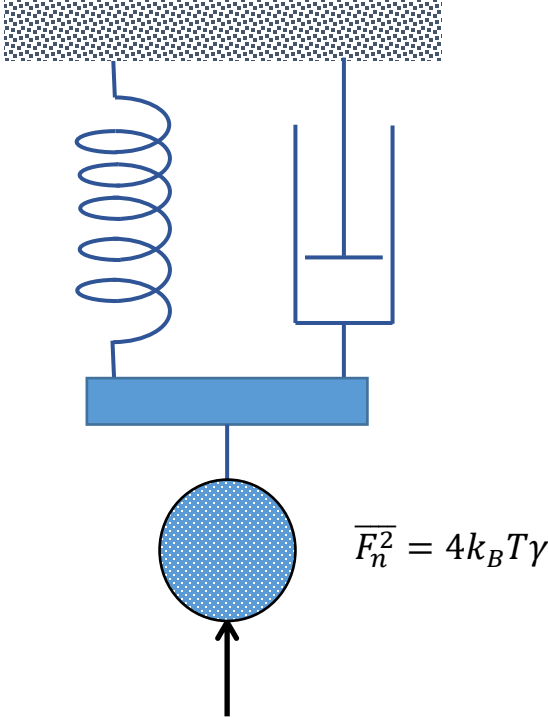
Figure 13. Equivalent rms noise model of a standard mass-spring-damper system.

To describe and quantify a sensor performance, it is necessary to calculate its signal-to- noise ratio (SNR), which describes the quality of the signal. The SNR is usually defined as power ratios in order to make it applicable for most of the situations:

$$SNR = \frac{signal\ power, Ps}{Noise\ power, Pn}$$

(32)

In electrical systems, this can be expressed as:

$$SNR = \frac{Ps}{Pn} = \frac{v_s^2/R}{v_n^2/R} = \frac{v_s^2}{v_n^2}$$

(33)

or in dB units as the following:

$$SNR = 10\ log_{10}\frac{Ps}{Pn} = 20\ log_{10}\frac{v_s}{v_n}$$

(34)

2.7 References

[1]   J. Kaiser, "Untersuchungen uber das auftreten Geraushen beim Zugversuch," Ph.D. Thesis, Technische Hochschule, 1950.

[2]   C. A. Tatro, ""Sonic Techniques in the Detection of Crystal Slip in Metals," Michigan State University, East Lansing, Mich.1959.

[3]   C. Tatro and R. G. Liptai, "Acoustic Emission from Crystalline Substances," in *Proc, Symp. Phys. Nondestruct. Test*, San Antonio, Texas, 1962.

[4]   H. L. Dunegan, C. A. Tatro, and D. O. Harris, "Acoustic Emission Research," Lawrence Radiation Laboratory, Livermore1964.

[5]   ASNT, *Nondestructive testing handbook*. Columbus, OH: ANST, 2005.

[6]   A. Nair and C. S. Cai, "Acoustic emission monitoring of bridges: Review and case studies," *Engineering Structures,* vol. 32, pp. 1704-1714, 2010.

[7]   A. P. Wright, "A Multi-Axis Capacitive MEMS Sensor System for Acoustic Emission Sensing," Ph.D., Civil and Environmental Engineering, Carnegie Mellon University, 2009.

[8]   S. Kawamoto and R. S. Williams, "Acoustic emission and acousto-ultrasonic techniques for wood and wood-based composites: a review.," U.S. Department of Agriculture, Madison, WI Gen. Tech. Rep. FPL-GTR-134, 2002.

[9]   H. Vallen, "AE Testing Fundamentals,Equipment, Applications," *The e-Journal of Nondestructive Testing,* vol. 7, 2002.

[10]   B. Muravin. (2013, 4/13/2017). *Physical principals of Acoustic Emission*. Available: http://muravin.com/

[11]   NDT. (4/13/17). *Introduction to Acoustic Emission Testing*. Available: https://www.nde-ed.org/EducationResources/CommunityCollege/Other%20Methods/AE/AE_Equipment.php

[12]   M. H. Chen, S. J. Hung, J. H. Hsu, and M. S. C. Lu, "Design and Characterization of a CMOS Micromachined Capacitive Acoustic Sensor," in *2007 IEEE Sensors*, 2007, pp. 1148-1151.

[13]   A. R. D. Jones, R. A. Noble, R. J. Bozeat, and D. A. Hutchins, "Micromachined Ultrasonic Transducers for Damage Detection in CFRP Composites," vol. 3673, pp. 369-378, 1999.

[14]   I. J. Oppenheim, A. Jain, and D. W. Greve, "Electrical characterization of coupled and uncoupled MEMS ultrasonic transducers," *IEEE Transactions on Ultrasonics, Ferroelectrics, and Frequency Control,* vol. 50, pp. 297-304, 2003.

[15]   D. Ozevin, D. W. Greve, I. J. Oppenheim, and S. P. Pessiki, "Resonant capacitive MEMS acoustic emission transducers," *Smart Materials and Structures,* vol. 15, p. 1863, 2006.

[16]   W. Wu, D. W. Greve, and I. J. Oppenheim, "Characterization and Noise Analysis of Capacitive MEMS Acoustic Emission Transducers," in *2007 IEEE Sensors*, 2007, pp. 1152-1155.

[17]   A. P. Wright, D. W. Greve, and I. J. Oppenheim, "Sensitivity of a MEMS acoustic emission sensor system," 2009, pp. 72920R-72920R-9.

[18]   D. W. Greve, I. J. Oppenheim, W. Wu, and A. P. Wright, "Development of a MEMS acoustic emission sensor system," *SPIE Proceedings,* vol. 6529, pp. 1-9, 2007.

[19]   H. Saboonchi and D. Ozevin, "MEMS acoustic emission transducers designed with high aspect ratio geometry," *Smart Materials and Structures,* vol. 22, p. 095006, 2013.

[20]   D. L. Polla and L. F. Francis, "Processing and Characterization of Piezoelectric Materials and Integration Into Microelectromechanical Systems," *Annual Review of Materials Science,* vol. 28, pp. 563-597, 1998.

[21]   X. Chen and Y. Shi, "PZT Nano Active Fiber Composites-Based Acoustic Emission Sensor," in *Selected Topics in Micro/Nano-robotics for Biomedical Applications*, Y. Guo, Ed., ed New York, NY: Springer New York, 2013, pp. 9-22.

[22]   A. J. Pickwell, R. a. Dorey, and D. Mba, "Development of a thick film PZT foil sensor for use in structural health monitoring applications," *IEEE Transactions on Ultrasonics, Ferroelectrics, and Frequency Control,* vol. 60, pp. 373-379, 2013.

[23]   S. Dolinsek, J. Kopac, Z. J. Viharos, and L. Monostori, "An intelligent AE sensor for the monitoring of finish machining process," in *Intelligent Processing and Manufacturing of Materials, 1999. IPMM '99. Proceedings of the Second International Conference on*, 1999, pp. 847-853 vol.2.

[24]   V. Kaajakari, *Practical MEMS*: Small Gear Pub., 2009.

[25]   T. B. Gabrielson, "Mechanical-thermal noise in micromachined acoustic and vibration sensors," *IEEE Transactions on Electron Devices,* vol. 40, pp. 903-908, 1993.

[26]   A. N. Cleland and M. L. Roukes, "Noise processes in nanomechanical resonators," *Journal of Applied Physics,* vol. 92, pp. 2758-2769, 2002.

[27]   F. Mohd-Yasin, D. J. Nagel, and C. E. Korman, "Noise in MEMS," *Measurement Science and Technology,* vol. 21, p. 012001, 2009.

[28]   T. J. Sobering. (1999, 4/20/2017). Noise in Electronic Systems. [Technote]. Available: https://www.k-state.edu/edl/docs/pubs/technical-resources/Technote4.pdf

CHAPTER 3: ACOUSTIC EMISSIONS MODELING

Structural Health Monitoring (SHM) is the main engineering tool to prevent and mitigate premature structural collapses. The ability of SHM systems to provide timely and accurate information, thus avoiding a catastrophic failure, has a crucial impact on both public safety and economic investments. Acoustic Emission (AE) is one of the most common nondestructive SHM techniques to determine if cracks are growing at the interior of a structure or monitor the degree of structural deterioration. These acoustic emissions are short-duration elastic waves (impulses) with high-frequency contents (30 kHz to 1 MHz) that are triggered by evolving micro- fractures in solids and other confined events related to structural integrity, such as chemical corrosion and pressure leaks.

Between all the current AE technologies, MEMS capacitive acoustic emission (AE) transducers have the greatest potential to resolve several shortcomings of the traditional piezoelectric sensors with the advantage of possible on-chip integration with preamplifier, while allowing a substantial cost reduction due to the batch manufacturing nature of MEMS processing technology.

In order to evaluate the performance of capacitive acoustic emission sensors, in this chapter, a thorough modeling and simulation approach for capacitive MEMS acoustic emission transducers is presented and validated by using the experimental behavior of a device from the published literature. Furthermore, four revised designs were made, in order to explore the effect of the top electrode perforations' aspect ratio and electrodes'

gap distance on the quality factor, sensitivity, transient response, and signal to noise ratio (SNR). Six 3D solid finite element analysis (FEA) models were constructed to perform modal and harmonic analysis of the devices with a particular emphasis on their damping characteristics.

3.1 Analytical Modeling

In Chapter 1, it was mentioned that a parallel plate capacitive actuator could be modeled as a lumped mass-spring-damper system that is governed by the equation:

$$\mathrm{m}\ddot{x} + c\dot{x} + kx - F_{elect} = -m\ddot{u} \tag{1}$$

where *k* represents the equivalent stiffness, *c* accounts for the damping coefficient, *m* is the equivalent mass, and F_{elect} is electrostatic force that is generated between the two electrodes, when a DC bias voltage (*V$_{dc}$*) is applied. The damping coefficient defines the amplitude of an oscillation as a result of energy that comes from an acoustic emission event. On the other hand, the stiffness constant can be directly correlated to resonance frequency of the acoustic emission sensor. This two parameters and the electrostatic force are strongly affected by the top electrode's geometry as well. In order to study the performance of MEMS AE sensors, a similar top electrode design and geometry was investigated by Wu et al. [1], Wright et al. [2] and Saboonchi et al.[3], was adopted to simulate the effective electromechanical characteristics and dynamic behaviors. This open grill geometry was modified to generate five MEMS AE sensors designs with different perforation aspect ratios in order to evaluate the correlation and effect of electrodes' openings dimensions and gap distance between top electrode and substrate on squeeze damping, Q-factor, SNR and transient response of the AE sensors. Figure

14 depicts the CAD layouts and the key geometries of the top electrodes that have been used for the AE sensor design optimization of this work. Basically, as can be seen in Fig. 14 (a)-(e), the original design was modified by varying the aspect ratio (AR) of the perforated holes while retaining the effective electrode area (A_e) and perforated hole area (A_h) as close as possible. The exact geometrical layouts and the key lateral dimensions for all designs were summarized in Table 1.
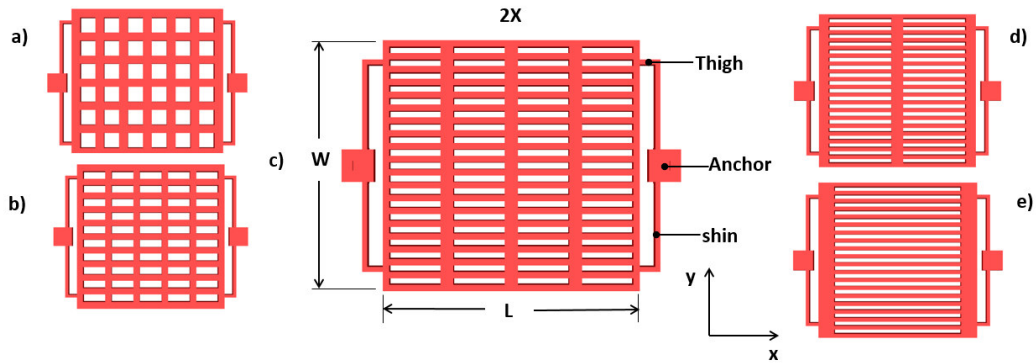
Figure 14. Illustration of the AE sensor design geometries and key CAD layout (lateral) dimensions.

Table 1. A summary of the geometrical designs and key dimensions of the investigated AE sensors.

Device	AR	Width (W)	Length (L)	W_h	L_h	A_e/A_h
AEs1	1:1	390 µm	400 µm	40 µm	40 µm	1.71
AEs2	3:1	390 µm	400 µm	60 µm	20 µm	1.60
AEs3	8:1	390 µm	400 µm	80 µm	10 µm	1.57
AEs4	16:1	390 µm	400 µm	160 µm	10 µm	1.57
AEs5	32:1	390 µm	400 µm	320 µm	10 µm	1.57

In order to perform the numerical evaluation of equation 1, the stiffness of the structure and damping coefficient must be known. Table 2 presents the calculated value of the static capacitance, electrostatic force and displacement under a 10V DC bias voltage, using equations (6), (8) and (9). The differences in the calculated parameters are due to the slight variances in the overlap area and gap between the electrodes.

Table 2. The values of the key electrical parameters with a DC bias voltage (Vdc = 10V).

Device	C_0 [pF]	F_{elec} [N]	x [nm]
AEs1	0.868	-4.38×10^{-5}	6.45
AEs2	0.847	-4.27×10^{-5}	6.29
AEs3	0.84	-4.24×10^{-5}	6.24
AEs4	0.84	-4.24×10^{-5}	6.24
AEs5	0.84	-4.24×10^{-5}	6.24
Saboonchi[10]	0.742	-3.29×10^{-5}	4.84

3.1.1 Stiffness Constant Calculation

Amongst MEMS devices, it is prevalent to use the planar flexural mechanism, such as supporting beams, due to their ability to have a highly repeatable dynamic behavior. The strategically designed support beams also enable a stiffness-based movement constraint in order to generate actuation only in the desired direction while limiting the other movements due to a drastic stiffness difference. The anchor design adopted in this study is a variation of the typical crab-leg supporting beams, where the fixed end of the shin shares the same anchor point as shown in Figure 14. This supporting beam

arrangement is designed to occupy a less chip area in an array configuration while keeping the same flexural behavior of the typical crab-leg supporting beams. Similar to commercial AE sensors, this design is gear toward an excellent out-of-plane sensitivity, indicating that the beam suspension has to be significantly softer in the z-direction (out-of-plane) than x and y (in-plane) directions. With the assumption that there is no rotation between the fixed anchor points and the suspended proof mass, the following equations were used to determine the equivalent stiffness of the flexural supporting beams [4]:

$$k_x = \frac{Ehw_b^3(4L_b + \alpha L_a)}{L_b^3(L_b + \alpha L_a)} \tag{35}$$

$$k_y = \frac{Ehw_a^3(L_b + 4\alpha L_a)}{L_a^3(L_b + \alpha L_a)} \tag{36}$$

$$k_z = \frac{48S_{ea}{}^2 S_{eb}{}^2 L_b L_a}{4S_{ea}S_{eb}{}^2 L_a{}^4 L_b + 4S_{ea}{}^2 S_{eb} L_a L_b{}^4} \tag{37}$$

where L_a and w_a are the length and width of the thigh, L_b and w_b are the length and width of the shin, E is Young' Modulus of the structural material, h is the thickness. α represents a scaling factor defined as $\alpha=(w_b/w_a)^3$, while S_{ea} and S_{eb} represent the bending stiffness, which are related to Young's Modulus and moment of inertia by: $S_{ea}=EI_{x,a}$, $S_{eb}=EI_{x,b}$. The moment of inertia can be calculated as $I_{x,a}=w_a t^3/12$ and $I_{x,b}=w_b t^3/12$. As noted earlier, the geometric variations were solely applied in the form of the different aspect ratio of the perforated holes within the suspended membrane/proof mass, while identical supporting beam configuration and dimensions have been used. The calculated equivalent

stiffnesses were of the supporting spring under x, y, z axis $k_z = 6.79 \times 10^3 \; N \cdot m^{-1}, k_y = 1.37 \times 10^5 N \cdot m^{-1}, k_x = 5.63 \times 10^3 N \cdot m^{-1}$

3.1.2 Damping Factor Calculation

The oscillatory motion of the MEMS microstructures is known to be significantly affected by the surrounding air [5], [6], [7]. The air generates a force that opposes to the vibrational movements and causes a damping effect. This becomes more severe when the microstructure oscillates near another surface owing to the squeeze film damping created by the trapped viscous gas air between the surfaces [8]. The squeeze-film air damping is the dominant energy dissipation mechanism in capacitive MEMS devices with a suspended oscillatory proof mass adjacent to a stationary electrode that drastically affects the frequency characteristics of these micromechanical structures [6].

The effects of pressure, viscosity, and inertia in fluids are fully described by the Navier-stokes equations. Generally, the behavior of squeeze films is characterized by the inertial and viscous effects, but the inertial effects can be ignored due to the tiny dimensions of MEMS devices. Hence, the mathematical modeling of squeeze-film damping in MEMS devices can be further simplified into the Reynolds equation [9]. For a parallel plate transducer, the effects of the fluid squeeze-film damping, under isothermal conditions, can be described by Reynolds equation as follows:

$$\nabla \cdot \left((1 + 6K_n)h^3(P_0 + p)\nabla p \right) = 12\mu \frac{\partial \big((P_0 + p)h\big)}{\partial t} \tag{38}$$

where P_0 is the environment pressure, μ is the fluid viscosity, p is the amount of pressure change with respect the environment and h it's the air or gas film thickness. K_n is the

Knudsen number, that is represented by λ/h, where λ is the mean free path or the average distance traveled by a moving particle between collisions. If the film thickness is so small in such way that the mean free path became significant with respect to the thickness of the film, then a slip-flow condition could occur, and the continuum fluid equations cannot describe the flow behavior accurately [10].

For Eq. (38) to be applicable, the following assumptions must be valid: the gap is small; the pressure distribution across the gap is uniform; the film is isothermal, and the fluid velocity normal to the mass surface is negligible. Additionally, if the MEMS devices under analysis have small displacements compared with the nominal film thickness value ($\Delta h \ll h_0$) and small pressure changes ($p \ll P_0$), then Eq. (38) can be linearized into the following partial differential equation, which requires less computational power to be solved [10]:

$$\frac{P_0 {h_0}^2}{12\mu_{eff}}\nabla^2\left(\frac{\Delta p}{P_0}\right) - \frac{\partial}{\partial t}\left(\frac{\Delta p}{P_0}\right) = \frac{\partial}{\partial t}\left(\frac{h}{h_0}\right) \tag{39}$$

To verify the validity of Eq. (38) and Eq. (39), the Knudsen number (K_n) must lie in the slip flow regime ($0.01 < K_n < 0.1$), is not in this range, some correction factors for the fluid viscosity must be included to solve the differential equations. Meanwhile, the squeeze number (σ), which measures the degree of fluid compression in squeeze-films given by Eq. (40), should be less than 1 or the spring effects become important and need to be taken into account in the evaluated system. The $\sigma_{cut-off}$, is the cut-off squeeze number or the value where the damping and spring forces become equal. And it can be determined by Eq. (41) [7].

$$\sigma = \frac{12\mu\omega L_s^2}{h_0{}^2 P_0} \tag{40}$$

where L_s is the smallest characteristic dimension of the system and ω is the angular frequency.

$$\sigma_{cut-off} = \pi^2 \left(\frac{\chi^2}{4} + 1 \right) \tag{41}$$

where χ is the width-to-length ratio of the structure $\chi = W/L$.

The mean free path of air at ambient pressure is 68 nm [11], then the calculation of the Knudsen number is $K_n = 0.068$ for a for devices that have a 1 μm air gap. Based on the structure dimensions of the designs under study, the cut-off squeeze number $\sigma_{cut-off} \approx 12$. Table 3 shows the angular frequency dependent squeeze numbers for each design and the limit frequency where the damping force dominates over spring force for all the devices under test.

Table 3. Angular frequency dependent squeeze numbers and the limit frequency.

Device	$\sigma(\omega)$	$f_{max\ (KHz)}$
AEs1	$1.16 \times 10^{-7}\omega$	137
AEs2	$6.35 \times 10^{-7}\omega$	251
AEs3	$2.2 \times 10^{-7}\omega$	725
AEs4	$2.2 \times 10^{-7}\omega$	725
AEs5	$2.2 \times 10^{-7}\omega$	725

3.1.2.1 Mesh Convergence Study

The strategically designed AE sensors are composed of rectangular shaped plates and planar beams with orthogonal geometry. Thus eight-node Manhattan bricks were used as the mesh elements with uniform mesh density as is illustrated in Figure 15. Additionally, to have a right balance between computational resources and model accuracy, a mesh convergence study was done. Basically, successive mesh refinements were performed by isotropically reducing the mesh element sizes. Then a mechanical analysis was performed for the different mesh models until the peak proof mass plate displacement converges asymptotically.
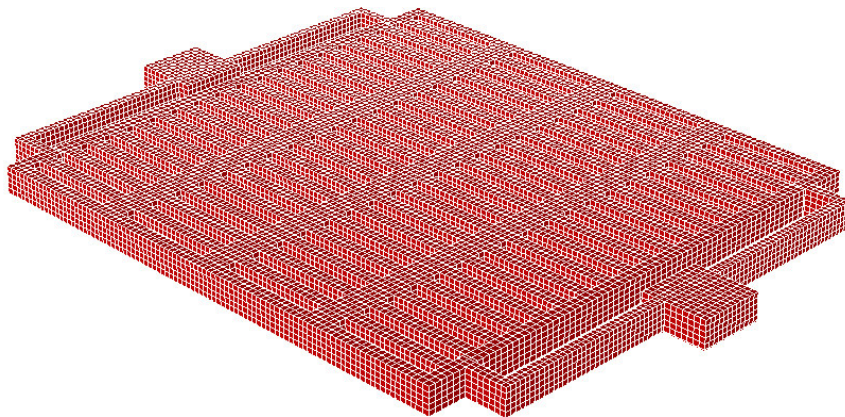
Figure 15. Schematic diagram of the meshed model. Eight-node Manhattan bricks were used for the mesh study for the top electrode of the AE sensor.

Figure 15 shows the proof mass plate displacement when a vertical pressure of 0.001 $\mu N/\mu m^2$ is applied to its top surface. Based on these results, from a mesh element number of 25,842 and more, the change in variation of the proof mass displacement is less than 0.7%. As seen in Figure 16, convergence has been attained with a minimum

mesh element number of $3{\times}10^4$ and simulation time is at least 5 times shorter than the higher mesh density used in this study.
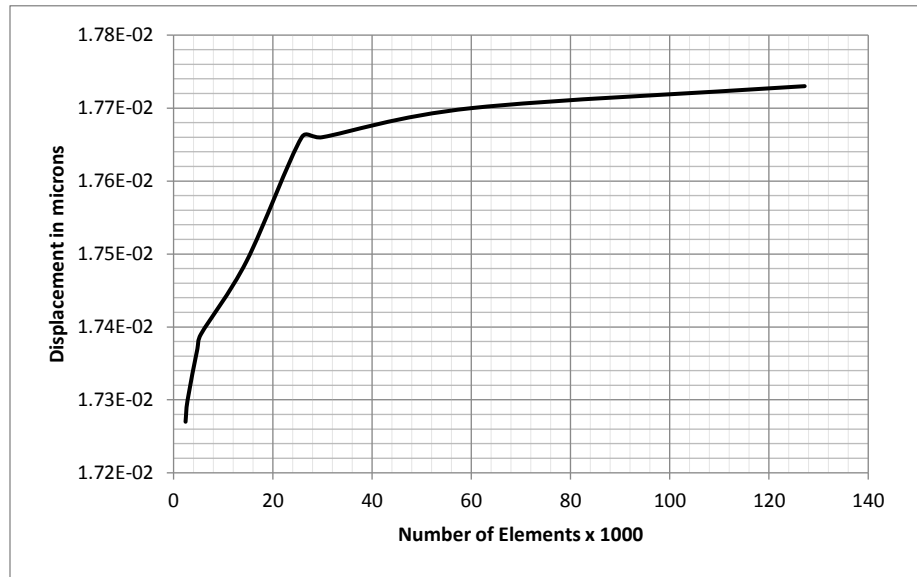
Figure 16. Results of the mesh convergence study. A minimum mesh element number of $3{\times}10^4$ is needed.

3.1.3 Damping Coefficient Extraction

Six 3D solid models were created within FEA tool to extract the damping coefficients, then modal and harmonic analysis were performed to identify the resonance frequencies of the MEMS structures and to determine the modal deformation displacements at the frequencies of interest. These tasks were conducted by using Coventorware as an FEA design software that contains a so-called DampingMM module to solve Eq. (38) numerically and to extract the damping coefficients for each of the relevant degrees of freedom. Figure 17 shows the squeezed-film damping coefficients in the z-direction, for the capacitive MEMS AE devices designed in this work and by Saboonchi et al. [3] at different frequencies.

By comparing these results with the analytical and experimental results reported by Saboonchi et al. [3], a small (4%) resonance frequency discrepancy is observed by our numerical results. In this prior work, an analytical model was used to calculate an anticipated Q value of 114, while their reported experimental results by a standard device admittance test and half-power bandwidth method indicated a Q-factor of 6 and 16, respectively. The numerical damping model incorporated by this work has led to an improved accuracy with 9.5% and 83% discrepancies, which is substantially better than 180% and 150% differences obtained by Saboonchi et al. by their analytical model [3].
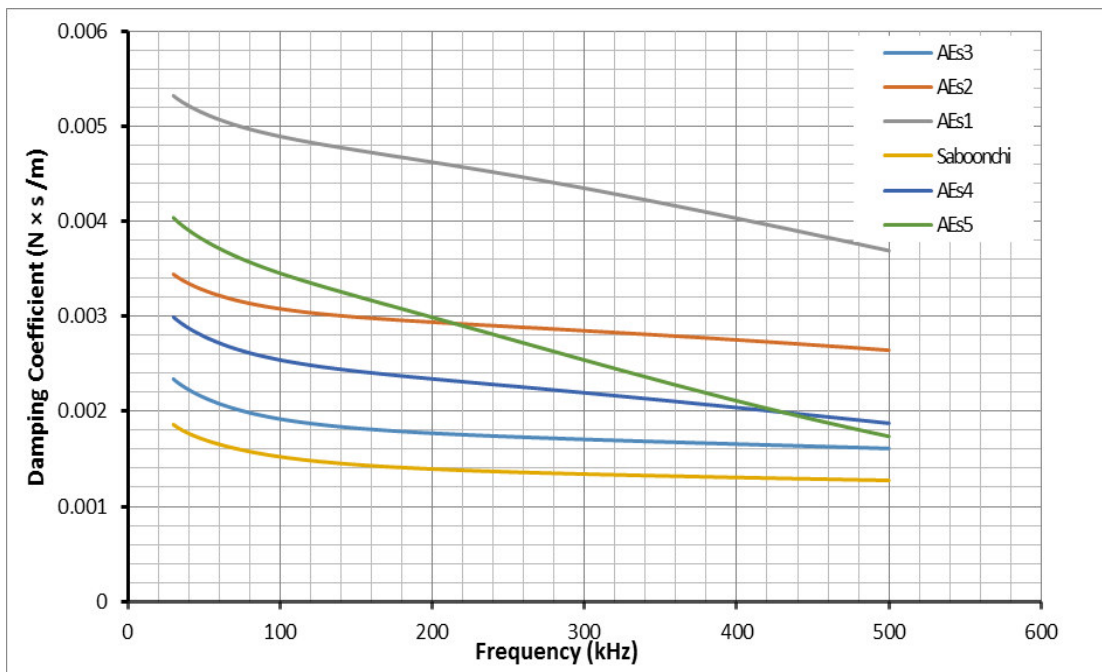

Figure 17. Simulated damping coefficients vs frequency for all the designs under study by this work.

Table 4 presents a summary of the key mechanical characteristics of all the devices under evaluation, including 5 new designs and a design identical to prior work by Saboonchi et al [3].

3.2 Electromechanical Analysis

The AE sensors investigated in this study leverages electrostatic actuation as its electromechanical energy transduction mechanism. The dynamic behavior of this MEMS structure is a function of the geometrical design of its moving parts base on perforated membranes and its elastic characteristics.

Table 4. A summary of the key mechanical characteristics of the AE devices designed and studied by this work.

Device	f_0 Numerical	f_0 Analytical	k_z	k_x	k_y	c	Q
AEs1	90425.4	97877.9				49.28×10^{-4}	2.07
AEs2	92342.5	99093.3				30.93×10^{-4}	3.3
AEs3	92899.7	99509.3				19.37×10^{-4}	5.21
AEs4	94212.9	99509.3				25.6×10^{-4}	3.26
AEs5	95230.7	99509.3				34.85×10^{-4}	2.82
Saboonchi	92341.2	99509.3				15.2×10^{-4}	6.6

Admittance is a measure of how ease an alternating current flow in a circuit or device, it's a vector quantity and its units are Siemens. The admittance tests are generally used to characterize the frequency response and the electromechanical coupling coefficient of transducers. Admittance is usually defined as the ratio of output current to the input voltage when a device is driven by a sinusoidal AC input voltage [12]. The following analytical expression for admittance is typically used for an electrostatic resonant actuator [12], [13].

$$Y = j\omega C_0 + F \frac{j\omega}{\omega_0^2 - \omega + {j\omega\omega_0}/{Q}} \tag{42}$$

Eq. (42) correlates the frequency characteristic of a resonant sensor with its electrostatic, geometric and structural characteristics. The details of the derivation of this equation are given in [14]. Figure 18 shows the simulated admittance amplitude and phase plots for the devices under study. The resonance frequencies can be seen more clearly in the phase plots presented in Figure 18(b). The admittance magnitude is peaked at the resonance frequencies, and the amplitudes are maximized for the design with perforation hole's aspect ratio (AR) of 8:1 that corresponds to AEs 3 that is similar to Saboonchi's design. Also as shown, the design with different perforation hole patterns only exhibited slight differences in their resonance frequencies.

3.3 Sensor Signal-To-Noise Ratio (SNR)

The performance of micromechanical sensors and actuators can be more severely impacted or degraded by mechanical and electrical noise. The specific noise source depends on the characteristics and physics of the sensor or actuator. But for MEMS devices that typically have static or movable elements at the micrometer scale, the mechanical-thermal noise is the main source that limits its performance. In fact, this type of noise generally defines the minimum tolerable size for these devices, even though the thermal noise energy is independent of the scale of the system.

As the devices reduce their sizes, the signal power is ordinarily lower while the noise level tends to increase in general. Consequently, the device's signal falls below the noise floor [15], [16], [17]. Specifically for AE sensors, the work made by Wu et al. demonstrated that main source of noise for the sensor itself is due to Brownian motion

[1]. This type of noise It is triggered by the random motion of particles suspended in a fluid (air) due to their collisions with the microstructure, thus causing motion of the movable parts and inducing a noise current. The rms current value generated by Brownian motion is given by [14], [2]:
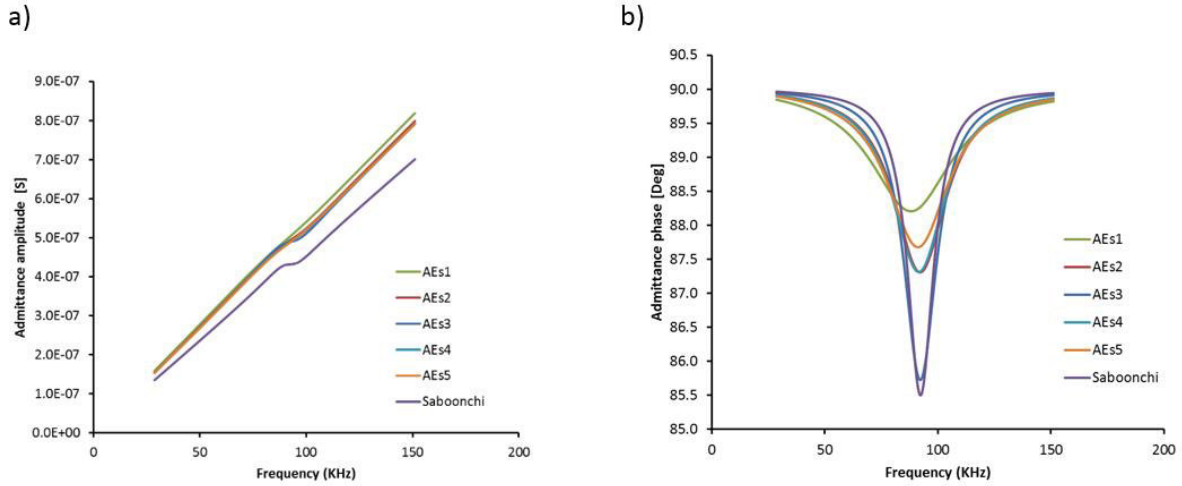

Figure 18. Admittance calculations results. a) Admittance amplitude, b) Admittance phase.

$$i_{RMS}{}^2 = \left(\frac{V_{DC}C_0}{g}\right)^2 \frac{k_B T}{N m_d} \tag{43}$$

where N is the number of devices, k_B is the Boltzmann's constant and T is the temperature in Kelvin.

In order to quantify a sensor performance, it is necessary to calculate its signal-to-noise ratio (SNR), which describes the quality of the signal. In this paper, the method proposed by Vallen et al. to compare the sensitivity of different AE sensors was adopted, where the peak SNR is defined as [18]:

$$SNR \ (dB) = 10Log\left(\frac{A_{p\_signal}}{A_{p\_noise}}\right) \tag{44}$$

where, A_{p_signal} and A_{p_noise} are the highest peak signal amplitude of the sensing element and the highest peak Brownian noise, respectively. It is important to highlight that the SNR calculated using only the Brownian noise underestimates its value as compared to a measured device with a readout circuit, as the added noise from the amplification electronics (e.g., Johnson or thermal noise) was not taken into account [1], [14], [12]. However, the fact that this type of noise comes from the MEMS sensor itself make it a good reference point to evaluate how the damping coefficient affects the best achievable SNR in these type of devices.

3.4 Dynamic Simulation

The AE sensor dynamic performance can be modeled by a second-order mass-spring-damper system with an electrostatic actuation as shown in Eq. (1). This mathematical model can be simulated by using MATLAB/Simulink, which is expressly instrumental to study systems that are governed by dynamic differential equations. This approach has been used to simulate the behaviors of many MEMS devices that are described by a second-order mass-spring-damper equation [19], [20], [21], [22], [23].

To perform the dynamic simulation of the deigned AE sensors, Eq.(1) was programmed in MATLAB/Simulink by using a force input that is generated at sensor's boundary by the surface displacement u(t) after an acoustic emission event occurs within a material. ASTM approves several methods to simulate AE signal sources in order to test or compare the performance of acoustic emission sensors. Sources like pencil lead break, gas jet and ultrasonic transducers driven by white noise, sweep or pulse

generators can be used for this task [24]. In this work, a pulse generator block is introduced as an input into the Simulink model, and its block waveform parameters were programmed following ASTM E976 recommendations. Basically, the pulse width should be either slightly less than one-half the period of the center frequency of the transducer and the pulse repetition rate should be low so that every acoustic wave train is completely damped before the next one arrive.

Figure 19 shows the Simulink's block diagram for the dynamic modeling of the AE sensor. The Brownian noise was modeled as bandwidth-limited white noise source (i.e., ideal white noise current) over the entire bandwidth of the system. Its power magnitude is calculated by Eq. (18), and the output current generated is proportional top electrode velocity given by [14]:

$$i(t) = \left(\frac{V_{DC}\epsilon_0 A}{g^2}\right)\frac{dx}{dt} \tag{45}$$

Eq. (45) can be programmed as a gain that multiplies the velocity of the proof mass.

In typical AE signal, the waveforms initially are direct waves from the source, while the latter part are from waves that have been reflected back and forward several times before hitting the sensor. In general, a typical AE source motion takes about a few microseconds, the wave takes about a millisecond to reach the sensor and the total span of the wave is about 1.5 milliseconds [31]. Figure 20 shows the transient response of each one of the analyzed sensors after a pulse input signal. In all the devices the waveform envelope shows a fast rise, but the decay response differs from one sensor

design to another as the damping factor increases. It is evident that the damping coefficient strongly affects the overall "ringing" behavior.
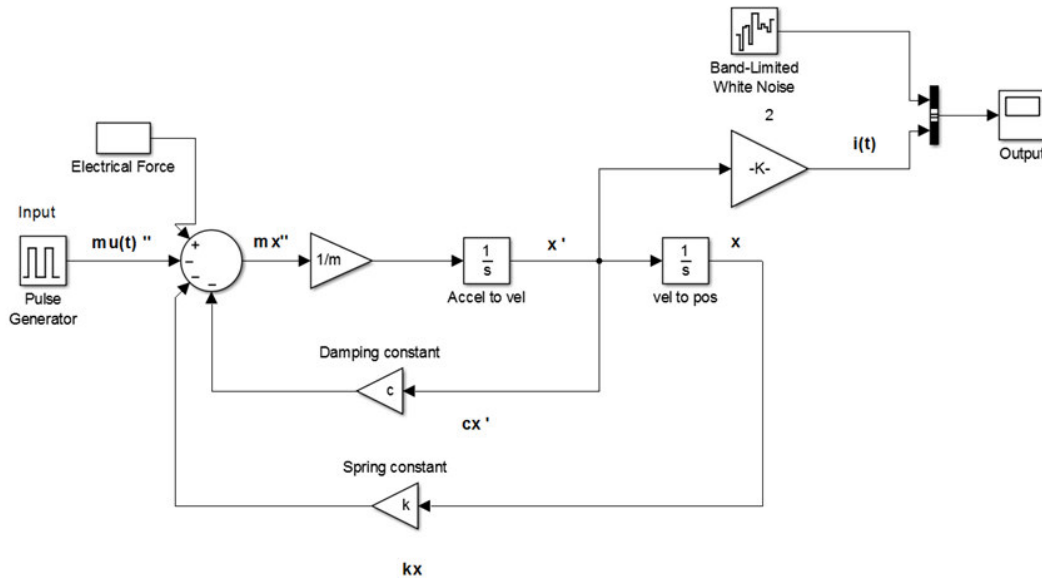

Figure 19. Block diagram for the Matlab/Simulink dynamic modeling of the AE sensor.

In a typical resonant sensor such as an accelerometer, ringing can be detrimental because it increases its settling time while a region beyond the maximum tolerable displacement can be reached to damage the sensor due to significant overshoot [25]. The ringing behavior of an AE sensor needs to be even more carefully evaluated because it influences several waveforms parameters including hit counts, rise time, duration and energy content, which are used to locate and characterize the AE sources. Meanwhile inadequate ringing conditions can lead to distorted AE information content. Particularly, the hit count parameter, which is the number of times a signal crosses a preset threshold, is evidently affected by the damping characteristics of the transducer, as shown in Figure 20. For the same pulse signal, if the threshold is around 0.3E-7A, AEs1 is capable of

detecting one signal crossing (hit count), while Saboonchi's sensor can pick up four. Therefore, in order to exhibit consistency in AE data interpretation, it is essential to tune up the damping characteristics of these type of MEMS AE transducers.
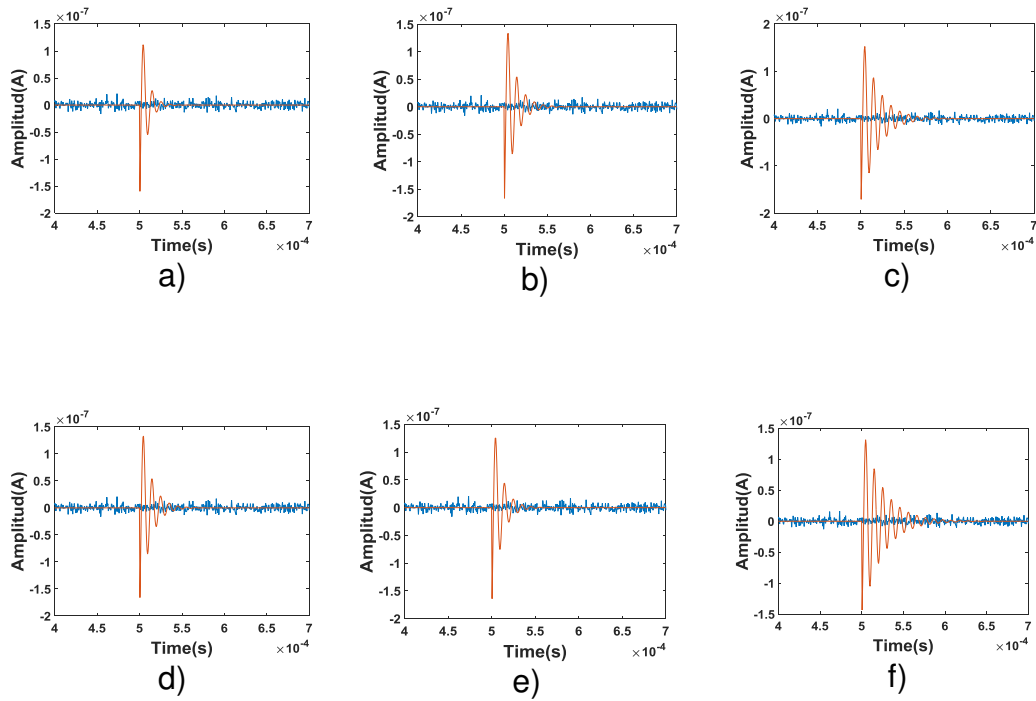

Figure 20. Simulated time-domain dynamic response of sensors. a) AEs1, b) AEs2, c) AEs3, d)AEs5, e) AEs6, and d) Saboonchi [3].

Figure 21 shows the signal-to-noise ratio (SNR) and the quality factor (Q) for the AE devices with different perforation aspect ratios (AR) within the suspended proof mass/plate. The SNR is slightly affected by the pattern and aspect ratio perforated holes in such way that the device with AR 8:1 (AEs3) have higher SNR even though it has slightly less electrode area than those of AR 1:1 (AEs1) and AR 3:1 (AEs2). This is because the current signal is directly proportional to the electrode velocity and higher damping coefficient results in a lower peak velocity. In general, as can be seen in Eq.

(3), reduced damping coefficient results in higher Q. The devices with AR 8:1 (i.e., AEs3 and Saboonchi's design) have shown higher Q. It is important to highlight that the slight difference in the Q value between these devices with same AR can be ascribed to the difference in gap distance (1 µm for AEs3 vs. 1.1 µm for Saboonchi's device). The squeeze-film damping effect strongly depends on the gap distance. As a result, the damping coefficient of the latter is slightly lower.
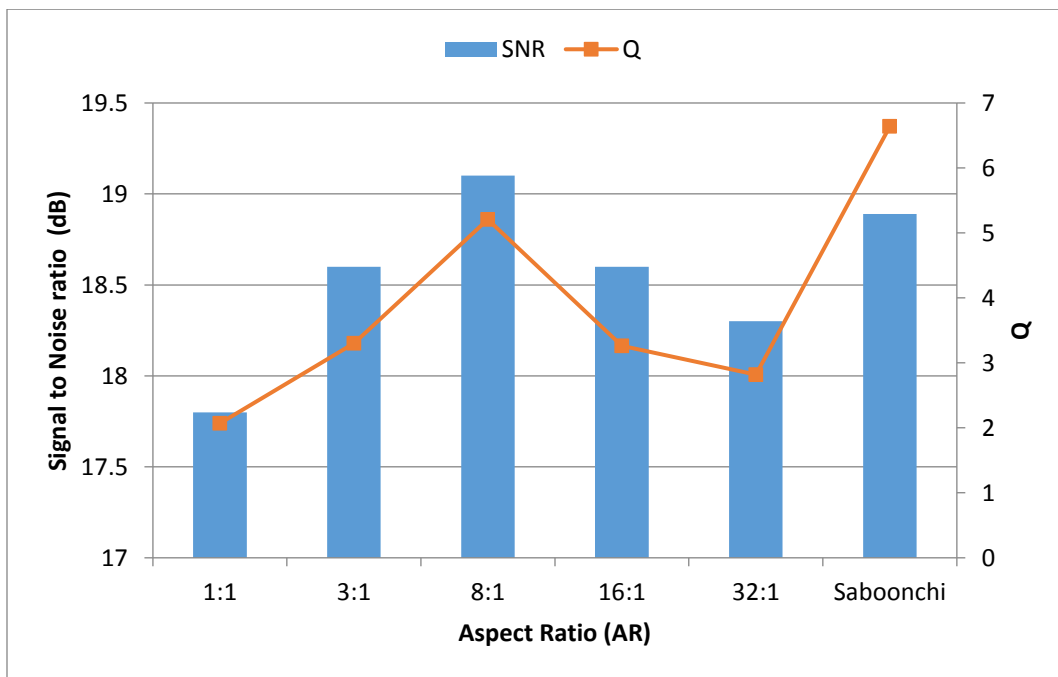

Figure 21. SNR and Q factor for AE devices composted of perforated plates with different perforation aspect ratio (AR).

The effect of the gap can be seen in Figure 22, which shows the SNR and Q values for a device with AR 8:1 designed with different capacitive gap distances between electrodes. Basically, the SNR decreases with a greater gap distance due to the lower capacitance, whereas Q increases with an increased gap spacing due to the lower

52

damping coefficient. For AE applications, SNR ratio can be readily improved by using a parallel array of individual transducers to boost the signal and/or improving the readout circuit, but the damping characteristics should be managed carefully by tailoring the design of the plate perforation and gap spacing between the electrodes to ensure a fast, stable and adequate ringing characteristics of the designed MEMS AE sensor.
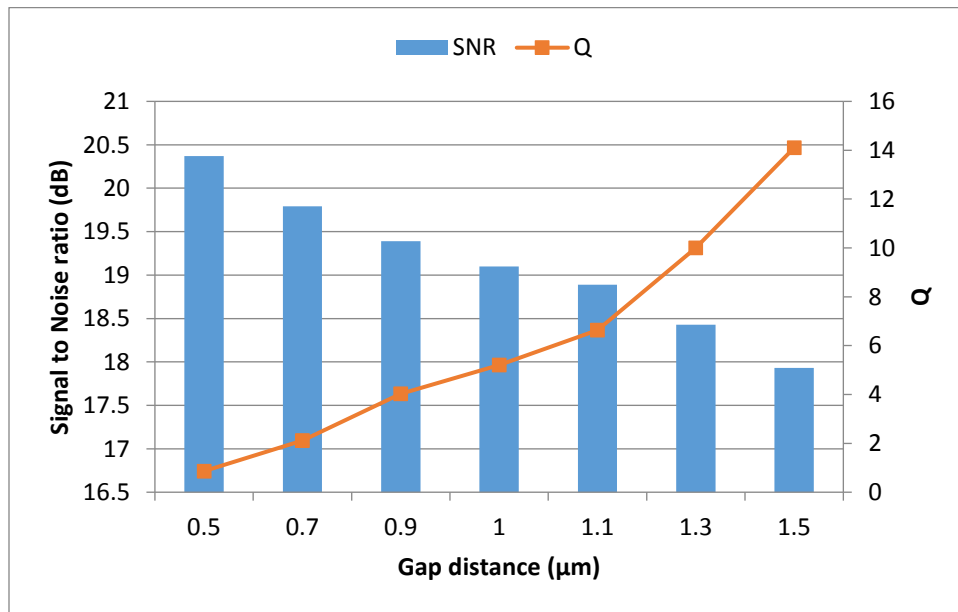

Figure 22. SNR and Q values for a device with AR 8:1 with different capacitive gap distances between electrodes.

With this simulation results, it can be stated that although capacitive transducer is known to be strongly affected by damping coefficient, a trade-off must be made between higher signal strength and damping characteristics of the transducer for the target AE sensor application. Although the large electrode surfaces and small gaps required to attain proper sensing capacitance, the utilization of bigger electrode surfaces or inadequate gaps can lead to inconsistencies in AE data interpretation. In essence, the

key parameters used to locate and characterize the AE sources, including hit counts, rise time, duration and energy content, can be distorted if the damping behavior of these types of transducers is not correctly tuned.

3.5 References

[1] W. Wu, D. W. Greve, and I. J. Oppenheim, "Characterization and Noise Analysis of Capacitive MEMS Acoustic Emission Transducers," in *2007 IEEE Sensors*, 2007, pp. 1152-1155.

[2] A. P. Wright, D. W. Greve, and I. J. Oppenheim, "Sensitivity of a MEMS acoustic emission sensor system," 2009, pp. 72920R-72920R-9.

[3] H. Saboonchi and D. Ozevin, "MEMS acoustic emission transducers designed with high aspect ratio geometry," *Smart Materials and Structures,* vol. 22, p. 095006, 2013.

[4] G. K. Fedder, "Simulation of microelectromechanical systems," Ph.D., Dept. of Electrical Engineering and Computer Science, Univ. of California at Berkeley, 1994.

[5] M. Andrews, I. Harris, and G. Turner, "A comparison of squeeze-film theory with measurements on a microstructure," *Sensors and Actuators A: Physical,* vol. 36, pp. 79-87, 1993/03/01 1993.

[6] M. Bao and H. Yang, "Squeeze film air damping in MEMS," *Sensors and Actuators A: Physical,* vol. 136, pp. 3-27, 5/1/ 2007.

[7] P. Ashok Kumar and P. Rudra, "Effect of flexural modes on squeeze film damping in MEMS cantilever resonators," *Journal of Micromechanics and Microengineering,* vol. 17, p. 2475, 2007.

[8] W. E. Newell, "Miniaturization of Tuning Forks," *Science,* vol. 161, pp. 1320-1326, September 27, 1968 1968.

[9] J. B. Shukla, S. Kumar, and P. Chandra, "Generalized reynolds equation with slip at bearing surfaces: Multiple-layer lubrication theory," *Wear,* vol. 60, pp. 253-268, 1980/05/01 1980.

[10] J. B. Starr, "Squeeze-film damping in solid-state accelerometers," in *Solid-State Sensor and Actuator Workshop, 1990. 4th Technical Digest., IEEE*, 1990, pp. 44-47.

[11]   S. G. Jennings, "The mean free path in air," *Journal of Aerosol Science,* vol. 19, pp. 159-166, 4// 1988.

[12]   a. W. Harris, I. J. Oppenheim, and D. W. Greve, "MEMS-based high-frequency vibration sensors," *Smart Materials and Structures,* vol. 20, p. 075018, 2011.

[13]   D. Ozevin, D. W. Greve, I. J. Oppenheim, and S. P. Pessiki, "Resonant capacitive MEMS acoustic emission transducers," *Smart Materials and Structures,* vol. 15, p. 1863, 2006.

[14]   A. P. Wright, "A Multi-Axis Capacitive MEMS Sensor System for Acoustic Emission Sensing," Ph.D., Civil and Environmental Engineering, Carnegie Mellon University, 2009.

[15]   T. B. Gabrielson, "Mechanical-thermal noise in micromachined acoustic and vibration sensors," *IEEE Transactions on Electron Devices,* vol. 40, pp. 903-908, 1993.

[16]   F. Mohd-Yasin, D. J. Nagel, and C. E. Korman, "Noise in MEMS," *Measurement Science and Technology,* vol. 21, p. 012001, 2009.

[17]   A. N. Cleland and M. L. Roukes, "Noise processes in nanomechanical resonators," *Journal of Applied Physics,* vol. 92, pp. 2758-2769, 2002.

[18]   H. Vallen, J. Vallen, and J. Forker, "A Simple Method to Compare the Sensitivity of Different AE Sensors for Tank Floor Testing," *Journal of Acoustic Emissions,* vol. 25, 2007.

[19]   B. Mukherjee, K. B. M. Swamy, T. V. D. Krishnan, and S. Sen, "A simple low cost scheme for closed loop operation of MEMS capacitive accelerometer," in *Students' Technology Symposium (TechSym), 2014 IEEE*, 2014, pp. 111-115.

[20]   T. L. Grigorie, "The Matlab/Simulink modeling and numerical simulation of an analogue capacitive micro-accelerometer. Part 1: Open loop," in *Perspective Technologies and Methods in MEMS Design, 2008. MEMSTECH 2008. International Conference on*, 2008, pp. 105-114.

[21]   J. Soen, A. Voda, and C. Condemine, "Controller design for a closed-loop micromachined accelerometer," *Control Engineering Practice,* vol. 15, pp. 57-68, 1// 2007.

[22]   W. Chen, J. Ding, X. Liu, and C. Wang, "Design and system-level simulation of a capacitive dual axis accelerometer," in *2007 2nd IEEE International Conference on Nano/Micro Engineered and Molecular Systems*, 2007, pp. 614-617.

[23]   B. Boga, I. E. Ocak, H. Kulah, and T. Akin, "Modeling of a Capacitive MEMS Accelerometer System Including the Noise Components and Verification with Test Results," in *Micro Electro Mechanical Systems, 2009. MEMS 2009. IEEE 22nd International Conference on*, 2009, pp. 821-824.

[24]   "ASTM E976-15, Standard Guide for Determining the Reproducibility of Acoustic Emission Sensor Response," ed. West Conshohocken, PA: ASTM International, 2015.

[25]   O. Brand, I. Dufour, S. Heinrich, F. Josse, G. K. Fedder, C. Hierold*, et al.*, *Resonant MEMS: Fundamentals, Implementation, and Application*: Wiley, 2015.

CHAPTER 4: AE SENSOR FABRICATION PROCESS

In this work, a versatile fabrication process that offers compatibility with low-cost structural materials were developed. Additionally, different material's alternatives were investigated for the bottom and top electrode, the sacrificial layer, and the insulation layer.

4.1 Bottom Electrode
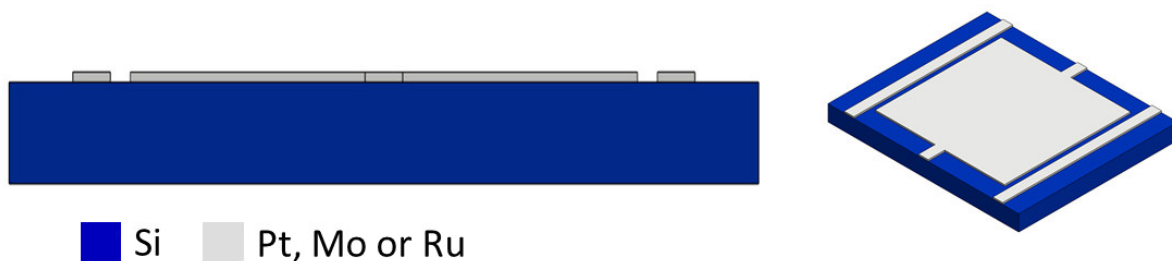
Figure 23. Illustration of the fabricaiton of bottom electrodes by a lift-off process.

The fabrication process starts with a low resistivity silicon wafer coated with 1 µm of thermal silicon oxide or 300 nm of Si_3N_4 as an insulation layer. The wafer is cleaned using Acetone, followed by Methanol and DI water. Then the wafer is dried with N_2 and baked for 5 minutes at a 110 °C to eliminate any humidity traces. Once the wafer has cooled down a dual layer spinning and lithography is performed as follows:

1) Initially, hexamethyldisilazane (HMDS) is spun on the wafer at 3500 rpm for 1 min. This organosilicon compound is used when the surface of the wafer is coated with Si_3N_4, SiO2 or other oxide starting layers. The reason is that these layers are hydrophilic

and have the tendency to absorb water from ambient humidity. The humidity can cause that the developer and other chemicals or etchants to penetrate the photoresist and generate extreme etch undercutting or the delamination of the photoresist film. The application of HMDS ensures photoresist adhesion by attaining the surface hydrophobicity required to avoid photoresist delamination [1].

2) As is showed in Figure 24, the Bottom electrode is fabricated by a lift-off technique using an undercut layer in a bi-layer lift-off process. The first layer is composed of a Polydimthylglutarimide resist that is commercialized as LOR and can be spun at speeds between 2500 and 4500 rpm to obtain different thicknesses between a few hundreds of nanometers to several microns. The layer thickness is a crucial parameter to be able to achieve a successful lift-off process. Its value will depend on the thickness of the deposited film, in such way that the LOR layer should be at least 25% thicker than the metal layer. If the layer is too thick, it can generate short circuit problems between nearby electrode features, this specifically critical if highly conformal depositions technique such as sputtering is employed. Table 5 shows the lithography conditions for the types of LOR resist that were used in this research.

3) For the second layer, AZ 1512 photoresist is used. Table 5 presents the lithography conditions for spinning, soft bake, exposure, hard bake and developing for AZ 1512. Figure 24 a-c illustrates the lithography sequence for the bi-layer processing for achieving a complete develoment of the AZ 1512 photoresist and a suitable undercut generated by the etching of the LOR when is exposed to the developer. The lithography conditions are demarcated by the type of photoresist that is used because the LOR is not UV sensitive. On the other hand, the undercut rate can be tailored by modifying the LOR's

58

soft-bake temperature and time; The undercut rate decreases with a higher temperature and soft bake times, and the temperature has a higher impact than the soft bake time [2]. Figure 25 shows the bottom electrode lithography and the resultant undercut in the LOR layer.
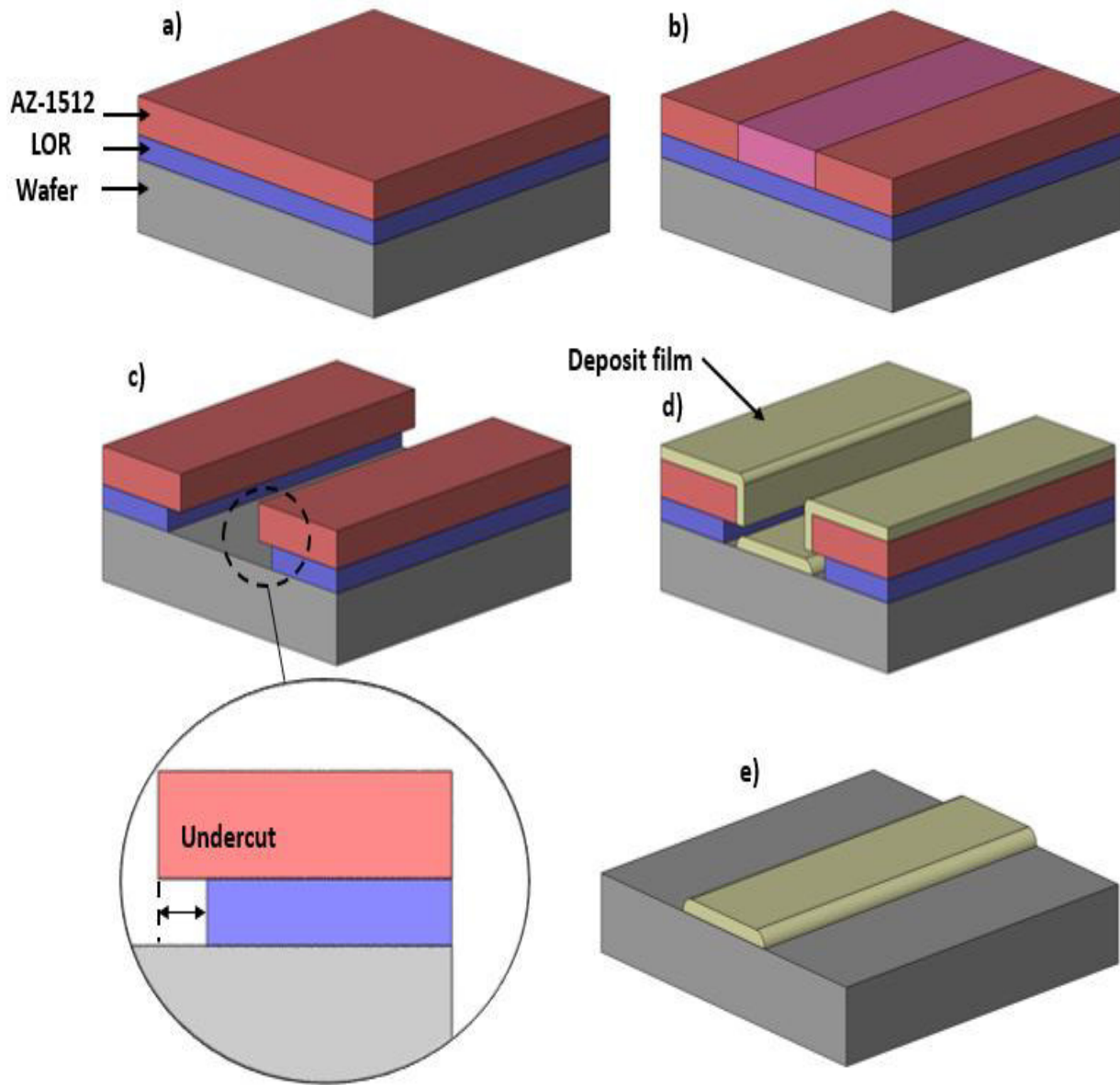

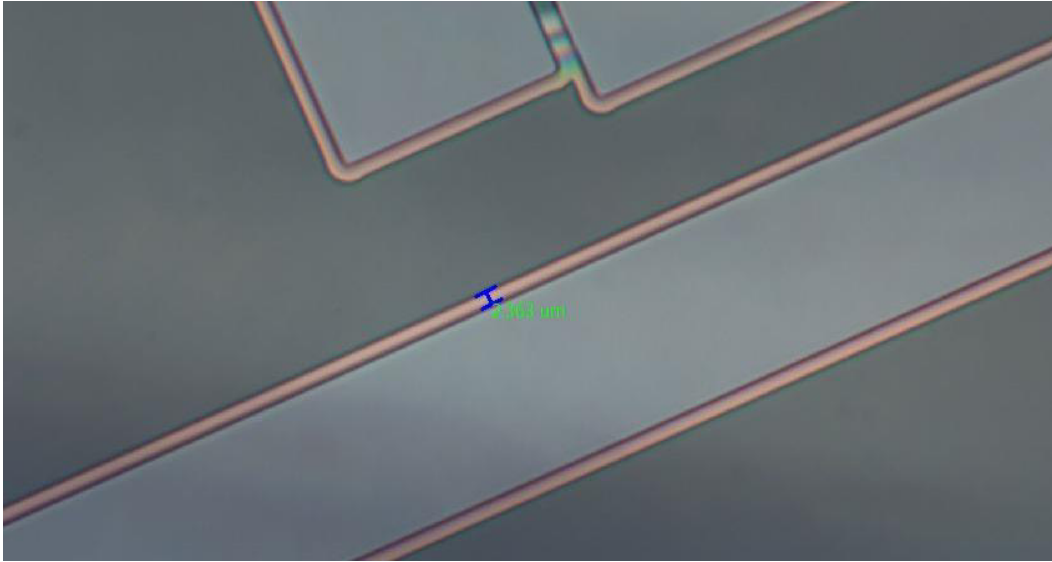Figure 24. Step-by-step illustration of the bi-layer lift-off process studied in this work.

Figure 25. Top-view microscope photo showing the lithographically defined pattern for the bottom electrode.

Table 5. UV lithography process parameters for the bottom electrode lift-off process.

Photoresist	LOR 3B	LOR 10B	LOR 10B (Diluted)	AZ 1512
Spinnig step 1 [rpm]	500	500	500	500
(time [s])	(10)	(10)	(10)	(10)
Spinnig step 2 [rpm]	2000	4500	3750	2500
(time [s])	(45)	(45)	(45)	(45)
Soft bake [ºC]	180	180	180	95
(time [s])	(510)	(510)	(510)	(50)
Dose [mJ/cm²]	NA	NA	NA	31.7
Post bake [ºC]	NA	NA	NA	105
(time [s])				(50)
Developer	NA	NA	NA	AZ 726
(time [s])				(25)
Layer thickness [µm]	0.350	0.7	0.395	1.1

4) Once the lithography step is completed, the wafer is treated with O_2 descum at 50 W and 100 mTorr for 2 minutes to remove any residual photoresist. As is shown in Figure 24 c, the next step is to deposit the metal layer for the bottom electrode. In this work three materials were studied to be used as a bottom electrode including; Molybdenum, Platinum, and Ruthenium. The following properties defined the material selections criteria:

• The resistivity is usually the key characteristic required for thin films that are going to be used as an interconnect material in MEMS technology are low contact resistivity, low sheet resistance, high electron and stress-migration resistance [3]. Between them, an appropriate electrical resistivity is critical to decrease the energy dissipation and boost the energy transfer performance of the device [4]. As can be seen in Table 6, between the selected materials in this work Molybdenum has the lowest resistivity, but Platinum and Ruthenium also have a competitive electrical resistivity [5].

Table 6. Comparison of the key properties of the bottom electrode materials studied by this work.

Electrode Material	Resistivity $(\rho \times 10^{-8})$ $(\Omega \cdot m)$	Thermal expansion coefficient (α x10^{-6}) $m/(m \cdot K)$
Molybdenum	5.2	5
Ruthenium	11.5	9.1
Platinum	10.5	9

• The thermal expansion (α): is a phenomenon that occurs when a temperature gradient generates a change in the dimensions of the material. Then a low thermal

61

expansion coefficient is desired for compatibility with other material in contact with the bottom electrode. Otherwise, a high mismatch between two adjacent materials can lead to development of residual stress that can compromise the device's structural integrity. The bottom electrode layer is going to be in direct contact with the SiO_2 insulation layer, which has fairl low thermal expansion coefficient $\alpha = 0.65 \times 10^{-6}$ m/(m·K). Likewise, the top electrode as will be described later, could be Molybdenum or nickel ($\alpha = 13 \times 10^{-6}$ m/(m·K)) [6], [7]. As can be seen in Table 6, Molybdenum has the closets match in terms of its thermal expansion properties with that of the, but Platinum and Ruthenium have closets match with Nickel.

• The bottom electrode layer will be exposed to all the micromachining steps for the AE sensor fabrication. It is important that the selected material has an adequate chemical and physical compatibility with all the etchants, developers and any other reagents that will be in close contact with the electrode. From the selected materials, Platinum holds the highest chemical resistance and temperature stability, followed closely by Ruthenium while Molybdenum exhibits much poor stability.

The selected materials were deposited using an AJA Orion 5 sputtering system using the process conditions shown in Table 7. It is important to highlight that a good adhesion between this layer and the substrate must be guaranteed to have a good reliability of the device. Therefore, the substrate must be very clean and is highly advantageous to deposit first an oxide forming element between a metal and the SiO_2 or any oxide layer; this intermediate film allows a continuous transition from one lattice to another improving the adhesion properties [8]. Usually, Chrome, Titanium, and Aluminum are used as an adhesion layer and provide a good anchor for the subsequent metal layer.

In this work Chrome used as an intermediate layer and its sputtering conditions are presented in table 7.

Table 7. Sputtering conditions for the bottom electrode materials.

Electrode Material	Pressure (mTorr)	Power (W)	Time (Min)	Thickness (nm)
Chrome	3	100	14	20
Molybdenum	3	100		200
Ruthenium	3	100		160
Platinum	3	100		200

5) The last step to fabricate the bottom electrode is the lift-off process. The wafer is immersed into AZ-400T stripper at 180 °C for 45 to 60 minutes and then is washed with DI water. The inverse pattern and the undercut that was created in the bi-layer lithography process is used so that the stripper can reach the surface of the substrate. In this way the photoresist is used as a sacrificial layer and is washed away, the metal on top is lifted-off and is carried away with the sacrificial material, leaving only the desired pattern of the bottom electrode on the wafer. Figure 26 illustrates the CAD layout of the bottom electrode mask, and the fabricated bottom electrode using the explained process' sequence.

4.2 Insulation Layer Deposition

After the fabrication of the bottom electrode, an insulation layer is deposited using a Savannah 200 atomic layer deposition (ALD) system.

This layer is needed because the AE sensors have a large area and there is a high probability that residues from the top electrode fabrication like release features, parts of the alignment marks or even from other devices, land near or between the top and bottom electrode a create a short circuit between them. Figure 28 presents an example of the fabrication's debris landing in the AE device.
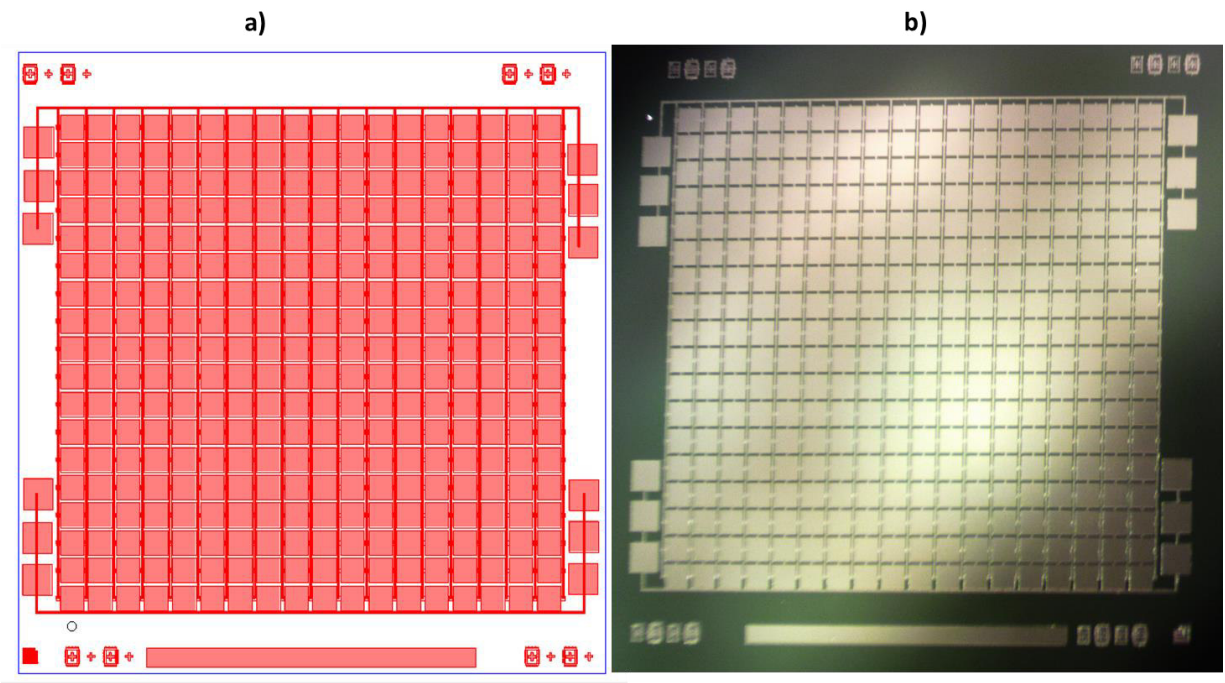
Figure 26. Bottom electrode CAD layout and fabrication. a) Bottom electrode CAD layout. b) Top-view microscope image of fabricated bottom electrode.

Si   Pt, Mo or Ru Al_2O_3 or HfO_2
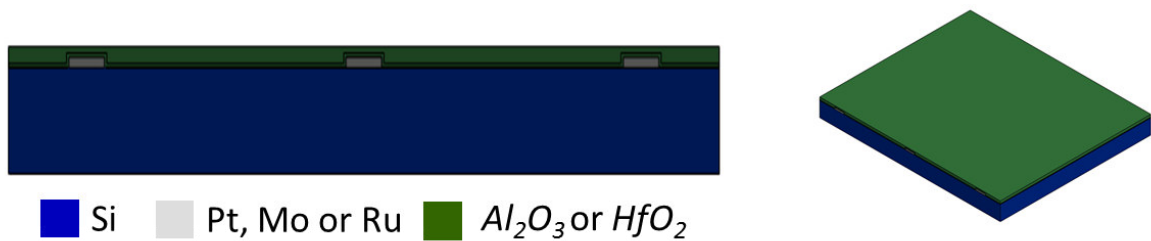
Figure 27. Schematic illustration of the insulation layer deposition.

This layer is needed because the AE sensors have a large area and there is a high probability that residues from the top electrode fabrication like release features, parts of the alignment marks or even from other devices, can land near or between the top and bottom electrode a create a short circuit between them. Figure 28 presents an example of the fabrication's debris landing inside an AE device causing a short-circuit issue.
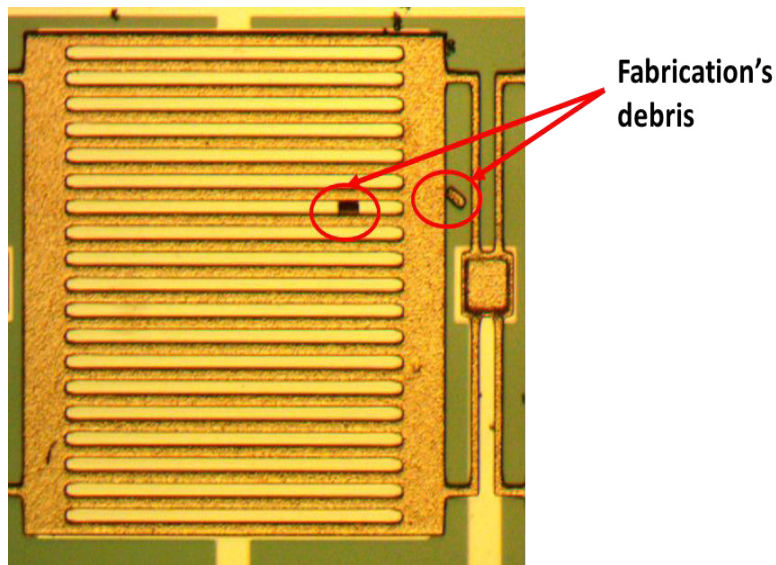
Figure 28. Top-view microscope image shown fabrication generated debris after the top electrode release process. Which might cause short-circuit problems.

In this work we used two materials as an insulation layer; Aluminum oxide (Al_2O_3) and Hafnium oxide (HfO_2). Its choice depends on the post-processing approach, if the subsequent fabrication process uses Buffered oxide etch (BOE), then HfO_2 is used preferably because its considerable lower etching rate compared with Al_2O_3.

Figure 29 presents the graphics interface of the Savannah atomic layer deposition system's control software. Table shows the ALD deposition process parameters for Al_2O_3

and HfO$_2$ films studied by this work, and all the recipes used to deposit each material have been included in Appendix II.

Table 8. ALD deposition process parameters for the two thin films studied in this work.

	Al$_2$O$_3$	*HfO$_2$*
Inner heater temperature (°C)	200	250
Precursor manifold temperature (°C)	150	150
Outer heater temperature (°C)	200	200
Stop valve temperature (°C)	150	150
Trap / Pump line temperature (°C)	150	150
Layer thickness [nm]	45	45
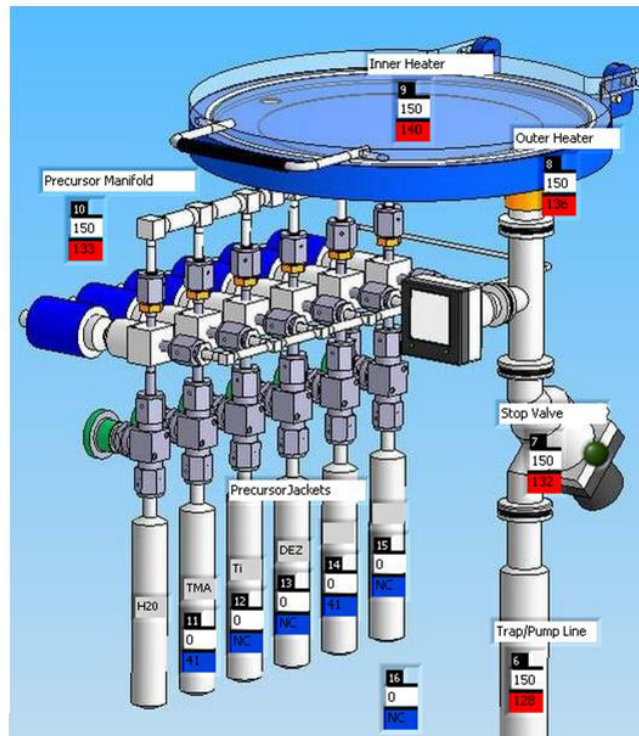
Figure 29. Graphic interface of the Savannah ALD control software.

4.3 Sacrificial Layer Deposition

Si   Pt, Mo or Ru Al_2O_3 or HfO_2 SiO_2 or PR
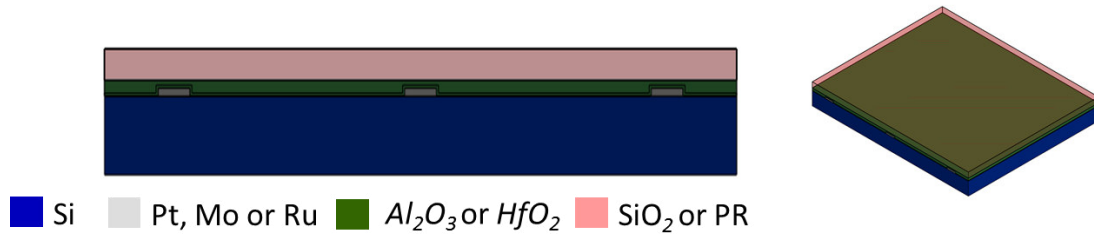
Figure 30. Schematic of the sacrificial layer deposition.

The next step in the fabrication process of capacitive MEMS AE sensors is the deposition of a sacrificial layer that will define the gap distance between the top and the bottom electrode. The material selected for this purpose will define the releasing process of the suspended and perforated metal membrane, which is one of the most critical steps in the fabrication of a MEMS capacitive device since the choice of sacrificial material will determine the releasing method. In this work, both wet and dry release methods were studied along with two sacrificial layer materials, which are plasma-enhanced chemical vapor deposition (PECVD) SiO_2 and photoresist. Wet etching of PECVD oxide by buffered HF and oxygen plasma dry etching were conducted as the final releasing processes.

4.3.1 Plasma-Enhanced Chemical Vapor Deposition (PECVD) SiO_2

Silicon dioxide is a common sacrificial layer to release movable mechanical parts of MEMS actuators and sensors, it has as advantages such as its compatibility with IC processes and its excellent etch selectively to silicon and several IC-compatible metals [9]. The main disadvantage of this wet release method is that if the structure is not sufficiently stiff, the capillary forces can result in a permanent stiction of the released microstructure to the substrate. To prevent this phenomenon, a variety of techniques

have been studied ranging from using an oxide etchant that creates an hydrophobic surface [10], a specific rinse-drying approach using low-surface tension alcohols or using supercritical carbon dioxide (CO_2) drying [11], among others.

To deposit this material a Plasma-Therm system have been employed by using reactive gases in an RF (radio frequency) reactive ion plasma. The plasma enhanced chemical vapor deposition (PECVD) system operates at 13.56 MHz, and the specific operating parameters to deposit SiO2 are shown in Table 9.

Table 9. PECVD SiO_2 deposition parameters.

	SiO_2
Power (W)	50
Chamber's temperature (°C)	250
Chuck's temperature (°C)	60
Pressure (mTorr)	800
N_2O flow (sccm)	500
SiH_4 flow (sccm)	110
Deposition rate [μm/hr]	2.3

4.3.2 Photoresist as a Sacrificial Layer

There are several motivations to use photoresist as a sacrificial layer: it is easy to coat; it can be patterned directly; it can be readily dissolved by wet or dry methods without the use of strong acids; it is compatible with the processes used in conventional IC manufacturing; and it have a low processing cost. However, when the photoresist is used as a sacrificial layer, it cannot be processed in the same fashion as in a regular lithography step. Even more, if the subsequent step is to deposit a metallization layer through

68

seeding/electro-plating or physical vapor deposition (evaporation or sputtering), more precautions are needed. The reason behind this is that the after developing the photoresist, it often deforms undesirably after any subsequent heating/baking process that is deemed necessary. Figure 31 shows the profilometer-scaned thickness profile of AZ 1512 photoresist after a regular UV lithography and a standard post-development hard bake at 110 °C for different times. Figure 31a illustrates the patterned thickness profile after development when no extra heating is applied, while Figures 31b, 31c, and 31d show the deformation in the profile's corners after 60, 900 and 2700 second of heating at 110 °C, respectively..
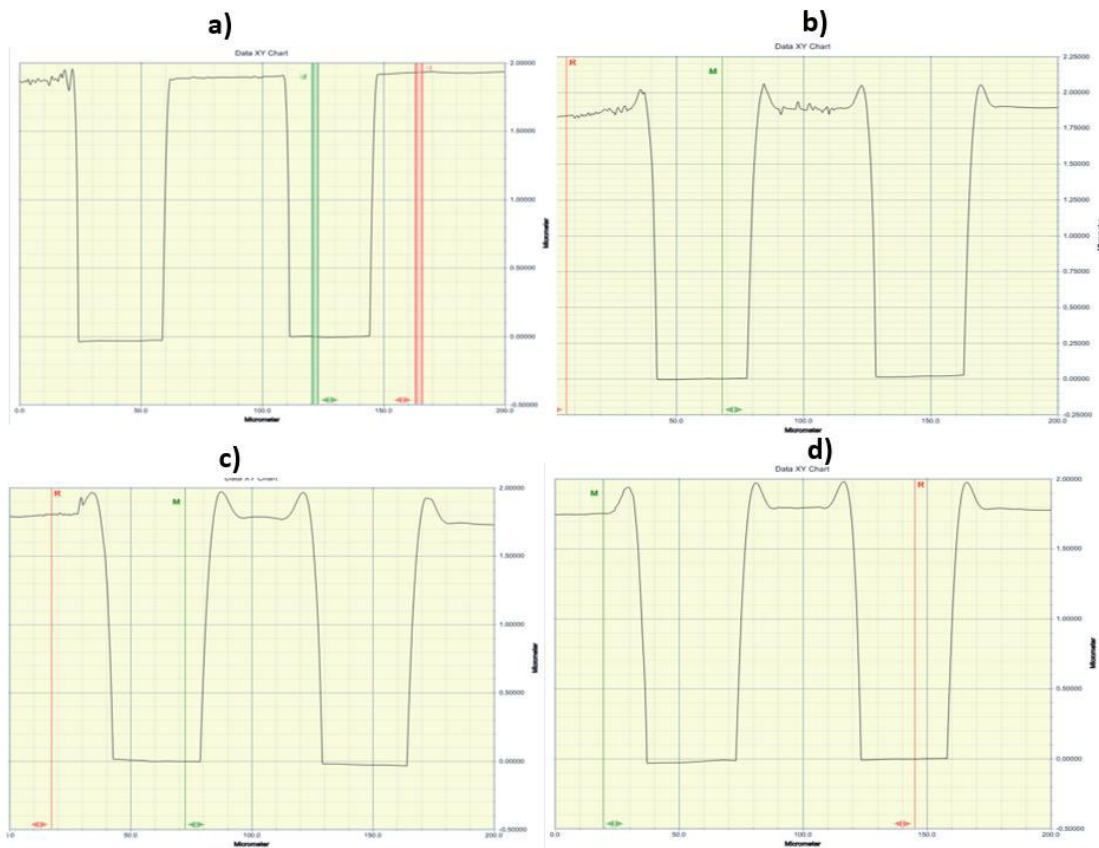
Figure 31. AZ 1512 photoresist profile changes after baking for different time at 110 °C.

These sharp corners in the photoresist's profile become a stress generator after a metallization layer is applied on top of the photoresist, which causes that the metal layer to crack and delaminate either right after the deposition or after any other subsequent heating step. Figure 32 illustrates this phenomenon after a copper layer was sputtered on top of the photoresist and heated to prepare for the next lithography step. It can be seen that the crack grow mainly from the corner of the big alignment bar feature, the alignment marks and the corners of the anchor points. The reason behind this is that the localized stresses present in sharp corners or notches could be several times higher than the average stress in the thin metal layer. In general, the level of stress intensity is higher due to smaller radius of curvature for these sharp edges [12].
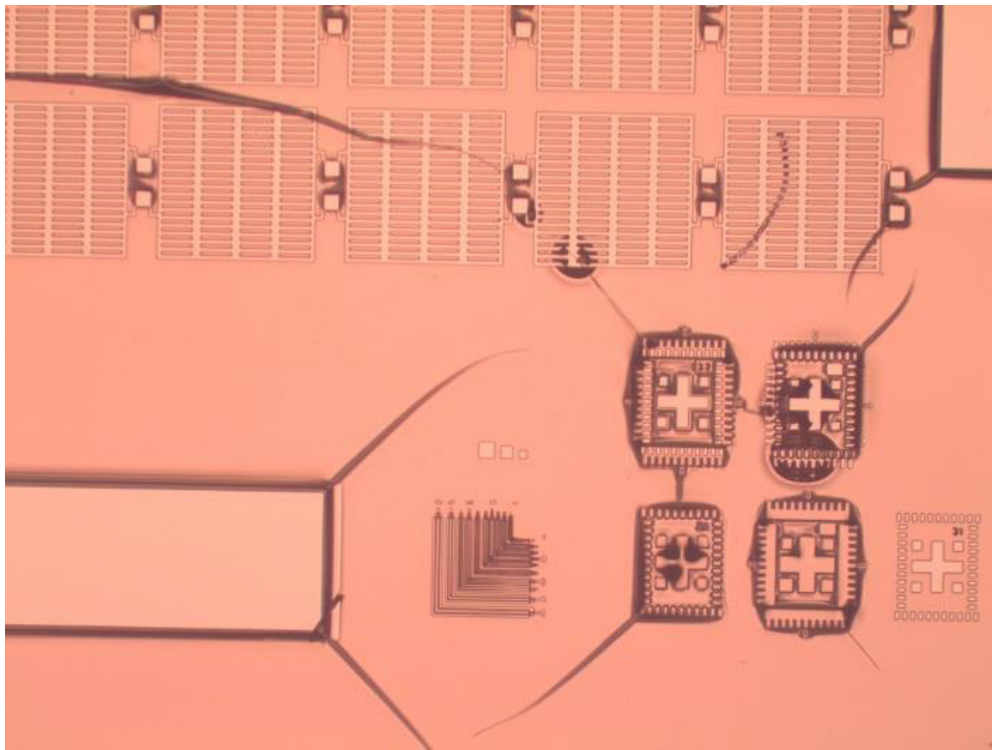
Figure 32. Cracks growth after a heating step on a copper layer over a photoresist sacrificial layer.

To reduce the stress concentration issues in the photoresist layer, it is required to heat it beyond its reflow temperature to cause the sharp edges to smooth out.

After several heat treatment experiments, it was found that the best condition to avoid the metal crack growth is achieved when the photoresist sacrificial layer is heated to 200 °C for 2 minutes. It can be seen in Figure 33 that the patterned photoresist thickness profile changes after this heat treatment. The sharp edges disappeared but it is also evident that there is a visible geometry change in the intended pattern. Fortunately, the fairly small geometrical change is not critical in the fabrication process of the acoustic emission sensors in this work.
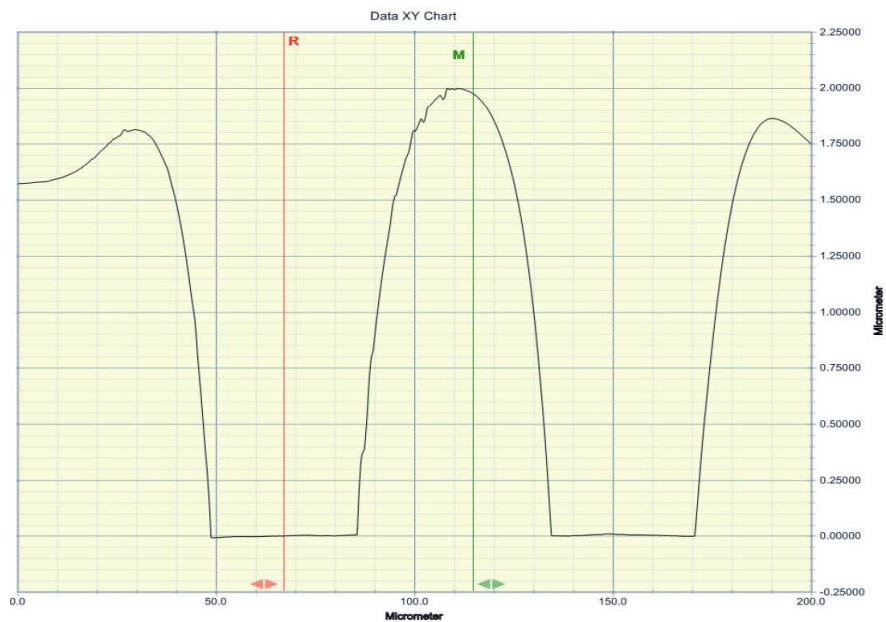
Figure 33. Patterned photoresist profile change after heating it at 200 °C for 2 minutes.

To be used as sacrificial layers, two photoresists were studied that are AZ 1512 and AZ 12XT. The former can achieve a range thickness from 1 to 2 µm, while the latter allows a thickness range from 4 to 14 µm. Figure 34 and Figure 35 presents the

experimental results for these photoresists that correlate the spin speed and the photoresist coating thickness.
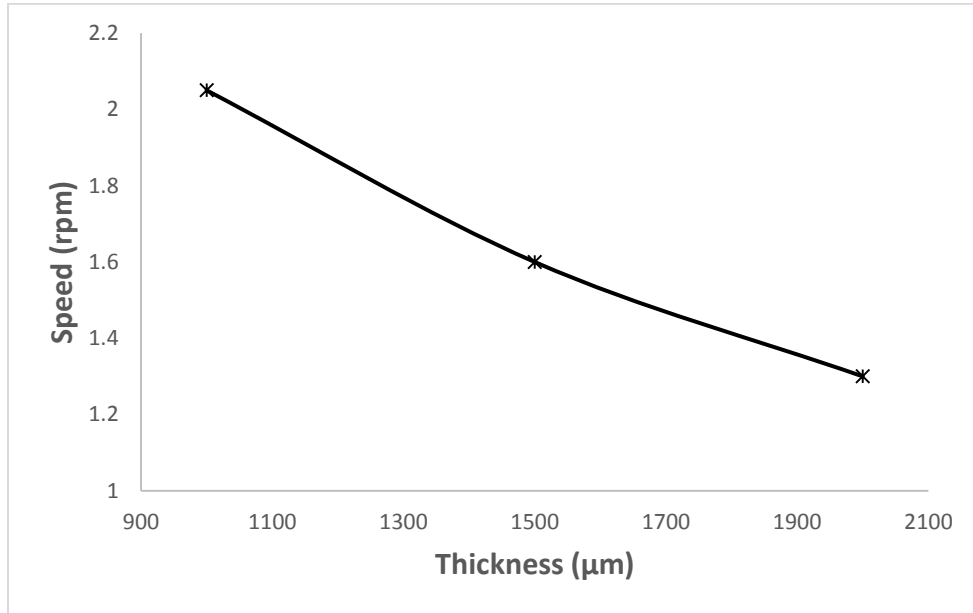
Figure 34. Correlation of the AZ 1512 photoresist thickness vs. spin speed.
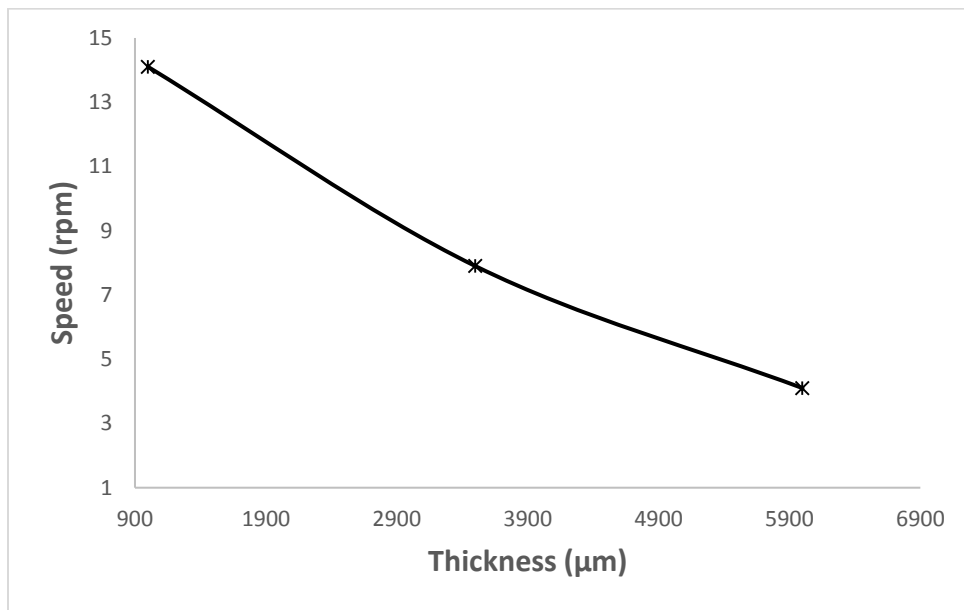
Figure 35. Correlation of the AZ 12XT photoresist thickness vs. spin speed.

4.4 Anchor Patterning

Si   Pt, Mo or Ru Al_2O_3 or HfO_2 SiO_2 or PR
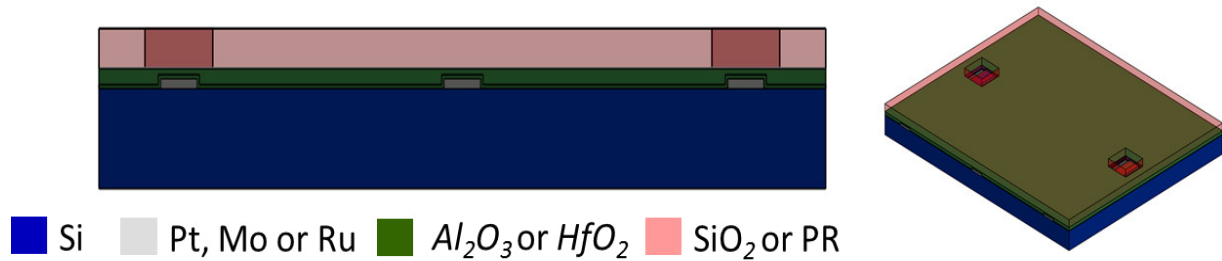
Figure 36. Schematic illustration of the device anchor patterning step.

Once the sacrificial layer is chosen and deposited, it is necessary to pattern the access to define the anchor points that will allow the ohmic contact between the top electrode through the anchor point located on the bottom electrode layer. The processes required to achieve this will depend on the sacrificial layer and the insulation layer selection as follows:

4.4.1 HfO$_2$ and SiO$_2$ Sacrificial Layer

1) For these materials, the fabrication step for the anchor starts with AZ 1512 lithography as is shown in Table 10.

Once the lithography step is completed, the wafer is treated with O$_2$ descum (ashing) at 50 W and 100 mTorr for 2 minutes to remove any residual photoresist.

2) Then a SiO$_2$ wet etch is performed using diluted 6:1 Buffer Hydrofluoric Acid (BOE) in DI water for 5 minutes or until a visible undercut is achieved as shown in Figure 37. Since AZ 1512 is formulated to have the best performance during wet etch applications, it is not required to hard bake the photoresist before the BOE wet etch procedure.

Table 10. UV lithography process conditions for the anchor patterning.

Photoresist	AZ 1512
Spinnig step 1 [rpm]	500
(time [s])	(10)
Spinnig step 2 [rpm]	2500
(time [s])	(45)
Soft bake [ºC]	95
(time [s])	(50)
Dose [mJ/cm²]	57.6
Post bake [ºC]	105
(time [s])	(50)
Developer	AZ 726
(time [s])	(25)
Layer thickness [µm]	1.1

3) After the wet etch step, a reactive ion etching (RIE) process is performed to remove the HfO_2 layer at the anchor locations. This process was done with an Alcatel AMS 100 inductively couple plasma (ICP) etcher. Table 11 presents the RIE parameters to etch the HfO_2 layer.

To verify that the HfO_2 layer is completely etched, a contact resistivity test is performed to check to ensure an ohmic contact between the metal electrodes.

4.4.2 Al_2O_3 and Photoresist Sacrificial Layer

1) For these choice of materials, the fabrication step for the anchor definition starts with the lithography of the either choice of photoresist (i.e., AZ 12XT, AZ 1512) that is used as sacrifice layer as is shown in Table 12.

74

Once the lithography step is completed, the wafer is treated by an O_2 descum (ashing) at 50 W and 100 mTorr for 2 minutes to remove any residual photoresist.

Figure 37. Top-view photo showing undercut observed after 5 minutes of BOE wet etch.

Table 11. Reactive ion etching (RIE) parameter to etch through the HfO2 layer.

	HfO_2
ICP Power (W)	600
Rf Power (W)	200
Pressure (mTorr)	2
Ar flow (sccm)	100
SF_6 flow (sccm)	100
Time (mins)	8

2) Then an Al_2O_3 wet etch is performed using 6:1 Buffer Hydrofluoric Acid (BOE) in DI water for 1 minute or until a contact resistivity test shows an ohmic contact between the metal electrodes.

Figure 38 illustrates the CAD layout of the anchor mask and the fabricated wafer with the explained device anchor definition processing step.

Table 12. Lithography process conditions for the chosen photoresist sacrificial layer.

Photoresist	AZ 12 XT	AZ 1512
Spinnig step 1 [rpm]	500	500
(time [s])	(10)	(10)
Spinnig step 2 [rpm]	6000	2500
(time [s])	(90)	(45)
Soft bake [ºC]	110	95
(time [s])	(120)	(50)
Dose [mJ/cm²]	124.8	57.6
Post bake [ºC]	90	105
(time [s])	(60)	(50)
Developer	AZ 300	AZ 726
(time [s])	(60)	(25)
Layer thickness [µm]	4.0	1.1

4.5 Electroplating Seed Layer Deposition

After the anchor patterning, a seed layer deposition is performed using an AJA Orion 5 sputtering system. The seed layer is made of a thin layer of titanium that acts as

an adhesion layer and a 200 nm-thick copper layer. Table 13 presents the sputtering conditions of these materials.
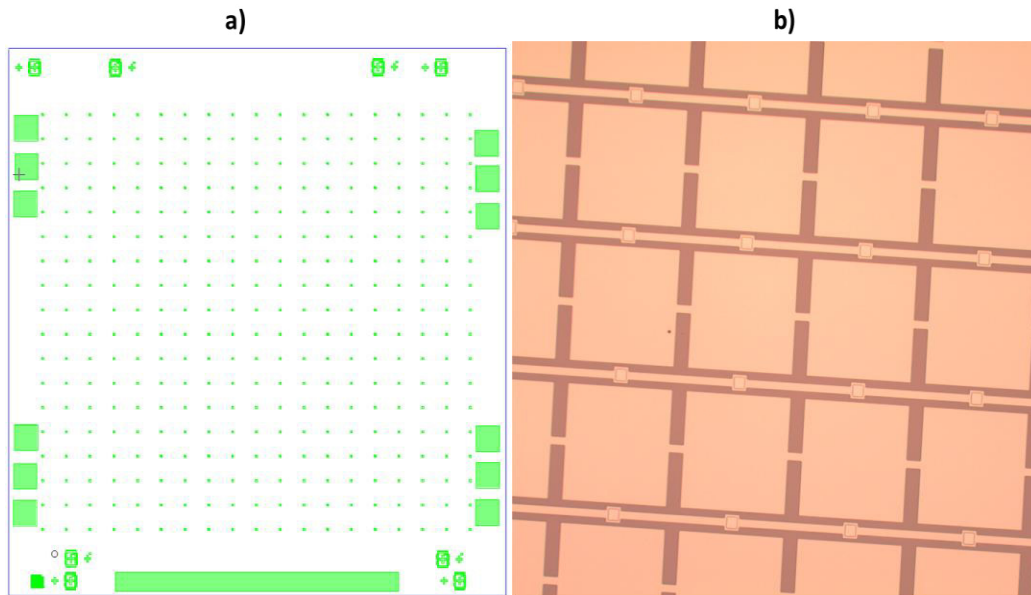
Figure 38. Anchor patterning mask CAD layout and fabrication. a) Anchor mask CAD layout. b) Fabricated device structure with anchor patterns defined.

Si ▮ Pt, Mo or Ru ▮ Al_2O_3 or HfO_2 ▮ SiO_2 or PR ▮ Cu & Ti
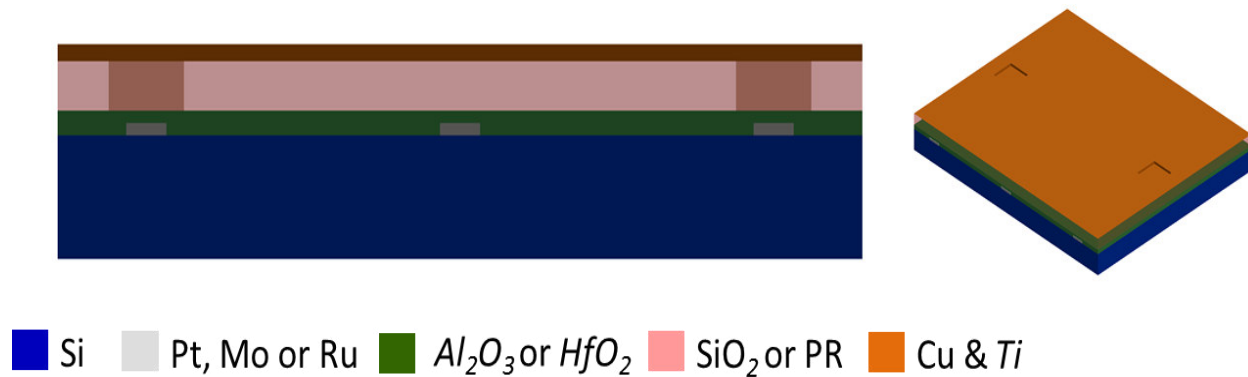
Figure 39. Schematic illustration of the seed layer deposition step.

It is worthwhile mentioning that the chosen seed layer material can be easily oxidized under atmospheric gas environment, thus, a suitable low base pressure needs to be achieved (at least 3 x 10^{-6} Torr or lower) and a pre-sputter of titanium for 10 min as

a form of the gettering process with the shutter closed needs to be performed before sputtering of each material.

Table 13. Sputtering process conditions for the seed layer deposition.

Electrode Material	Pressure (mTorr)	Power (W)	Time (Min)	Thickness (nm)
Titanium	3	150	8	20
Copper	3	100	20	200

4.6 Top Electrode Deposition

The top electrode formation is the most important step for the entire AE sensor fabrication because it will define the resonance frequency of the device and its damping characteristics. For this purpose, two materials and fabrications process have been investigated.
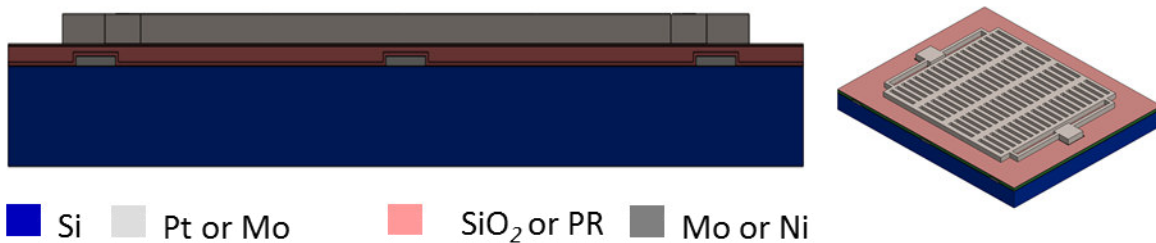
Figure 40. Schematic illustration of the top electrode deposition process.

4.6.1 Sputtered Molybdenum as the Top Electrode

Molybdenum have some interesting electrical and mechanical properties that make it very attractive as the structural material of MEMS acoustic emission sensor. As compared with Nickel, Molybdenum has a higher conductivity, density, and Young's

modulus. This means that molybdenum can achieve similar resonance frequency characteristics by having a considerable less electrode thickness while exhibiting less electrical resistance. To study this alternative, the following processing steps were explored:

1) Initially, a dual layer spinning and lithography was made using LOR 30B and AZ 1512 photoresist. The lithography process parameters are shown in Table 14.

2) Then 2 microns thick of molybdenum were sputtered using an AJA Orion 5 sputtering system. Before this step, a thin layer of Chrome that acts as an adhesion layer was also sputter deposited. Table 15 presents the sputtering process conditions for deposition of these materials.

Table 14. Lithography process parameters for lift-off of the Mo top electrode.

Photoresist	LOR 30B	AZ 1512
Spinnig step 1 [rpm]	500	500
(time [s])	(10)	(10)
Spinnig step 2 [rpm]	1500	2500
(time [s])	(45)	(45)
Soft bake [ºC]	180	95
(time [s])	(510)	(50)
Dose [mJ/cm²]	NA	31.7
Post bake [ºC]	NA	105
(time [s])		(50)
Developer	NA	AZ 726
(time [s])		(25)
Layer thickness [µm]	3	1.1

3) In a similar way to the formation of the bottom electrode (see section 4.1), a lift-off step is performed by immersing the wafer in AZ-400T photoresist stripper solution at 60 °C for 45 mins followed by washing with DI water. Figure 41 shows the molybdenum top electrode after the lift-off procedure.

Table 15. Sputtering process conditions for deposition of the Cr/Mo top electrode.

Electrode Material	Pressure (mTorr)	Power (W)	Time (Min)	Thickness (nm)
Chrome	3	100	14	40
Molybdenum	3	150	95	1045

4.6.2 Nickel Electroplated Top Electrode

For micromachining purposes, Nickel is an attractive material because of its wide range of variation of its alloys' properties like hardness, magnetic permeability, and reflectance. Additionally, when it is deposited by electroplating, a thick layer can be produced at low cost and high yield. This last manufacturing related characteristic make this material a viable choice as the top structural electrode for the AE sensors proposed in this work. Especially for obtain resonance frequencies in the range between 100 kHz to 1 MHz, the thickness of the nickel structural layer must be varied between 5 to 20 µm. Consequently, nickel electroplating is the most practical way to achieve the relatively thick layers to form suspended and perforated top electrode microsctures.

The nickel electroplating process starts from the seed layer deposition step (see section 4.5) as follows:

1) The electroplating mold is made by performing a AZ 12XT lithography using the conditions illustrated in Table 16. Once the lithography step is completed, the wafer is treated with an O2 descum at 50 W and 100 mTorr for 2 minutes to remove any residual photoresist.
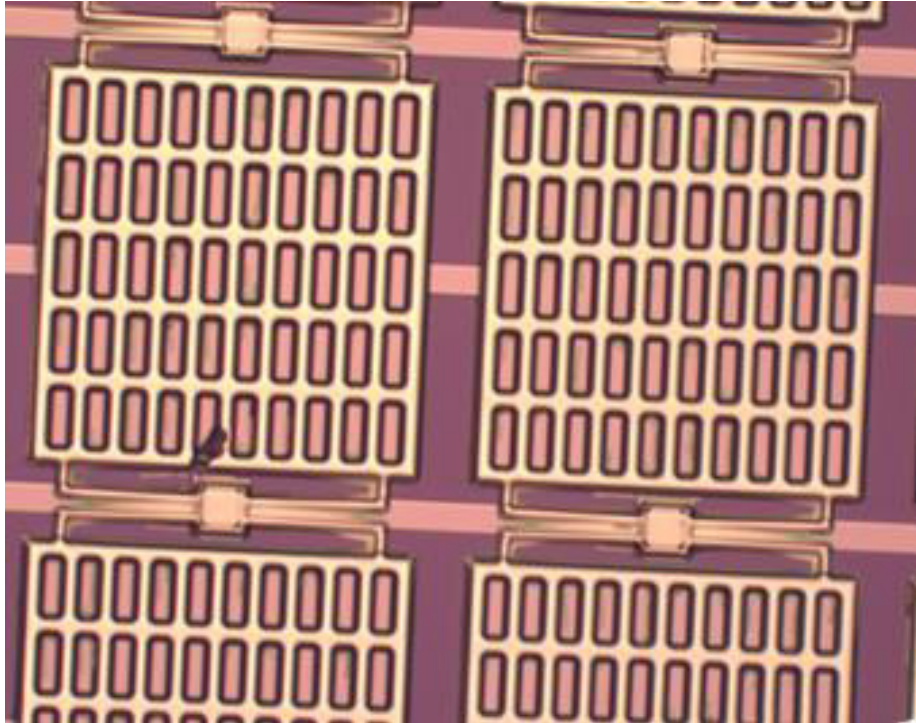
Figure 41. Micro-fabricated Mo top electrode of the AE sensor after the lift-off step.

2) Then one small portion of the photoresist on the edge of the silicon wafer substrate is removed by acetone and methanol in such way that the electroplating electrode fits and make direct contact with the copper seed layer underneath. Following this, the wafer with the lithography-patterned mold is hard baked at 110 °C for 5 minutes.

3) Prior to the electroplating process, the seed layer needs to be activated by removing any oxide residues that can be generated by the O_2 plasma descum (ashing)

process or the exposure of the copper to the environmental air. To do this, a copper oxide wet etch is performed by using a 200:1 solution of DI water to 30% Ammonium Hydroxide (NH_4OH). The activation is done by soaking the wafer in the solution for 30 seconds, followed by washing in abundant DI water. This processing procedures are repeated for three times[13].

Table 16. Lithography process conditions for defining the electroplating mold.

Photoresist	AZ 12XT
Spinnig step 1 [rpm]	500
(time [s])	(10)
Spinnig step 2 [rpm]	1000
(time [s])	(90)
Soft bake [ºC]	110
(time [s])	(120)
Dose [mJ/cm²]	249.6
Post bake [ºC]	90
(time [s])	(60)
Developer	AZ 300
(time [s])	(60)
Layer thickness [µm]	13

4) For the nickel electroplating process, a solution of nickel sulfamate (Ni(SO3NH2)2) was used to achieve low stress and high ductility. As is illustrated in Table 17, the solution was mixed with boric acid to keep the PH value between 3.5 and 4.5 to reduce the roughness and pitting, while nickel chloride and sodium lauryl sulfate are added to improve the conductivity and to improve the brightness, respectively [14]. The

wafer is connected to the cathode or the positive electrode of the current source, while a pure Nickel plate is connected to the anode. In the electroplating process when the current source is running, the Ni2+ ions are attracted and deposited on the cathode.

The approximated deposition thickness can be calculated from the current value and time with the following equation:

$$T = \frac{12.294 \times I \times t}{A}$$

(46)

where A is the area being electroplated in dm^2, T is the thickness (µm) and, I is the current in amperes and t is the time of the process in hours. The ratio I/A is the current density. The deposition rate is highly dependent on the current density and time, while the accuracy of the above equation is affected by the cathode current efficiency that may vary from 90% to 97%. Figure 42 illustrates the AE sensor array after the electroplating process as explained above.

4.7 Seed Layer Wet Etch

Once the electroplating is performed, the seed layer must be removed by wet etching in such way that the etchant has a good selectivity with respect the plated nickel electrode. Initially, the wafer is diced and the die is soaked for 4 minutes in a 1:1 solution of hydrogen peroxide (H_2O_2) and 30% Ammonium Hydroxide (NH_4OH) to remove the copper seed layer. Then it is washed with DI water and soaked for 1 minute in a 10: 1 solution of DI water and Hydrofluoric acid (HF) to also remove the titanium layer. Figure 43 presents the de AE sensor array after the seed layer removal and before the device's release.

Table 17. Composition and processing conditions for nickel electroplating solution based on nickel sulfamate.

Reagent or Condition	Value
Nickel Sulfamate $Ni(SO_3NH_2)_2$	180 g/L (ρ=1.5gr/cc)
Nickel Chloride $NiCl_2.6H_2o$	4.5 g/L
Boric Acid $B(OH)_3$	22.5 g/L
Sodium Lauryl Sulfate $CH_3(CH_2)_{11}OSO_3Na$	2.7 g/L
Temperature	$50 - 55^0C$
Agitation rate	200 rpm
Current density	10 mA/cm^2
pH value	3.5-4.5

4.8 AE Sensor Release

As the last step in the fabrication process, the device must be released and suspened before the subsequent acoustic or electrical performance test as an acoustic emissions sensor. The release procedure varied according to the selection of the sacrificial layer as follows:

4.8.1 PECVD SiO2 Sacrificial Layer Release Process

The PECVD silicon dioxide layer was removed by wet etch using a 6:1 Buffer Oxide Etch (BOE) solution. The solution was mixed with a 1% in a volume amount of Triton-X surfactant, to facilitate the wetting action of BOE in small gaps or geometries, where the surface tension will otherwise limit the access of the etchant or produce a very slow etch rate. The dies are soaked in BOE solution for ten mins, which were then carefully soaked in DI water and dried with N2.
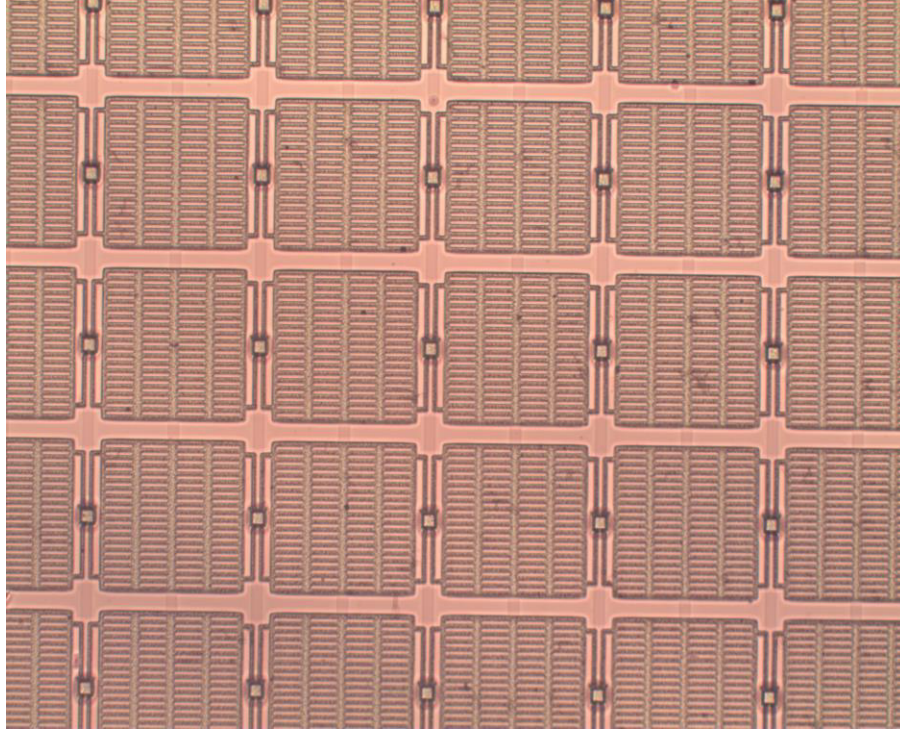
Figure 42. Top-view microscope image of the top electrode of the AE sensor fabricated by nickel electroplating process.

Table 18. O_2 plasma photoresist dry etching parameters by using an ICP etcher.

Parameters	Value
ICP Power (W)	2800
Rf Power (W)	200
Pressure (mTorr)	2
Ar flow (sccm)	100
O_2 flow (sccm)	100
Time (mins)	5

4.8.2 Photoresist Sacrificial Layer Release Process

When the photoresist is chosen as the sacrificial layer, the release process is then performed in two steps as follows:

1) Initially, the bulk photoresist that is not covered by the structural layer is removed using an O2 plasma with an Alcatel AMS 100 inductively coupled plasma (ICP) etcher. Table 18 presents the O2 plasma etching parameters to etch the photoresist layer.
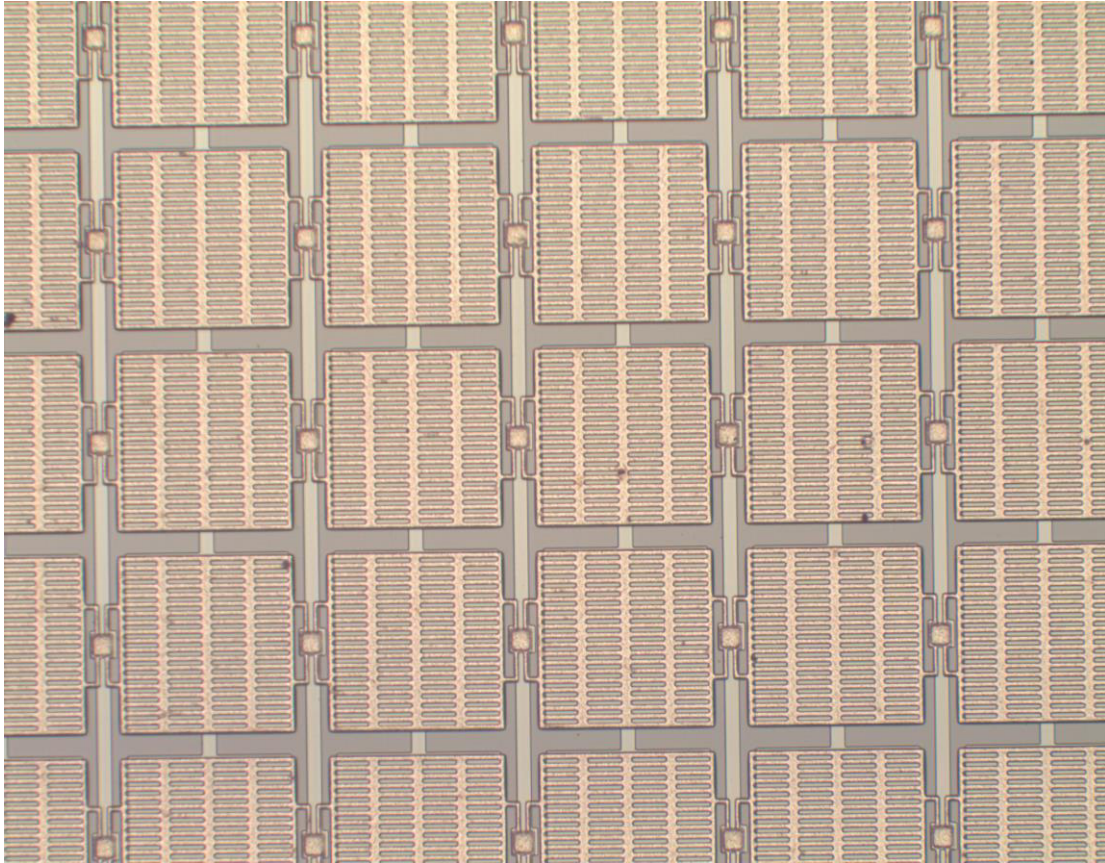
Figure 43. Top-view photo of the AE sensor array after the seed layer removal.

2) Then, to remove the remaining photoresist, a Plasma-Therm RIE system is used in a plasma etching mode (also known as PE mode). This mode utilizes a relatively high pressure to increase the lateral etching rate by shortening the mean free path. Because the photoresist sacrificial layer has to be heated beyond its reflow temperature before the nickel electroplating process, this O2 plasma dry etching of baked and harden photoresist can be fairly slow. It can take around 3 hours for AZ 1512 and more than 9 hours for AZ 12XT to be fully removed to form fully released microstructures. To define the required

time to release the AE sensor device structure, the top electrode of one of the devices is manually removed and checked under the microscope. Figure 44a shows a device with the incomplete release, while Figure 44b shows one device that is fully released. Table 19 shows the etching parameters for the plasma etching system.
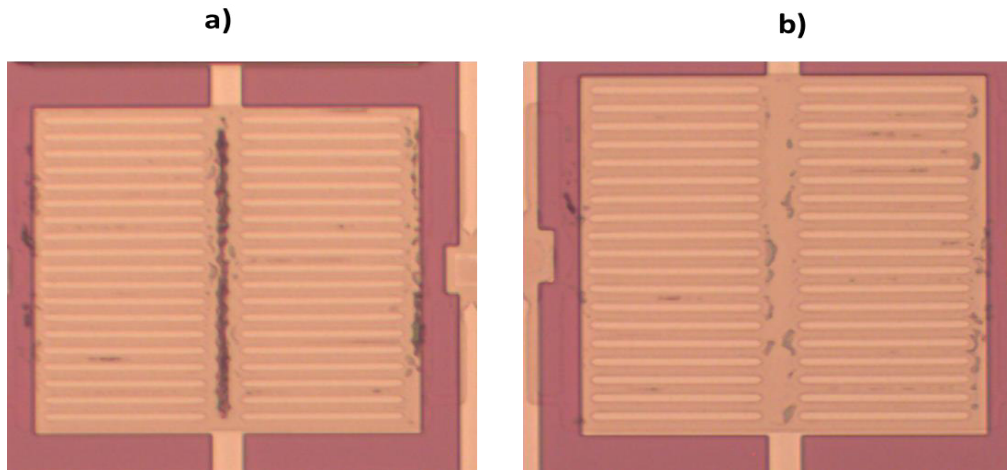
Figure 44. Top-view photos taken during release test. a) The bottom electrode after an incomplete release step; and b) the bottom electrode after a complete release.

Table 19. Photoresist dry etch process parameters under plasma etching mode.

Parameters	Value
Power (W)	400
Chuck's temperature (°C)	25
Pressure (mTorr)	500
O$_2$ flow (sccm)	200
Time (sec)	10000

4.9 References

[1]   I. M. Materials. (2013). *Photoresist adhesion and HMDS (hexamethyldisilazane) processing*. Available: http://www.imicromaterials.com/technical/hmds

[2]   M.   Chem.   (10/5/2017).   *LOR   and   PMGI   Resists*.   Available:
        http://microchem.com/pdf/PMGI-Resists-data-sheetV-rhcedit-102206.pdf

[3]   N.   Setter,   *Electroceramic-Based   MEMS: Fabrication-Technology   and
        Applications*: Springer US, 2005.

[4]   S. D. Senturia, *Microsystem Design*: Springer US, 2007.

[5]   engineeringtoolbox.com. (10/7/2017). *Resistivity and Conductivity - Temperature
        Coefficients   for   Common   Materials*.   Available:
        http://www.engineeringtoolbox.com/resistivity-conductivity-d_418.html

[6]   azom.com.   (10/7/17).   *Silica   -   Silicon   Dioxide   (SiO2)*.   Available:
        https://www.azom.com/properties.aspx?ArticleID=1114

[7]   engineeringtoolbox.com. (10/7/17). *Coefficients of Linear Thermal Expansion*.
        Available: http://www.engineeringtoolbox.com/linear-expansion-coefficients-
        d_95.html

[8]   M. J. Madou, *Fundamentals of Microfabrication: The Science of Miniaturization,
        Second Edition*: Taylor & Francis, 2002.

[9]   J. Bühler, F. P. Steiner, and H. Baltes, "Silicon dioxide sacrificial layer etching in
        surface micromachining," *Journal of Micromechanics and Microengineering,* vol.
        7, p. R1, 1997.

[10]   S. Yasuhiro and M. Masahiko, "Study of HF-Treated Heavily-Doped Si Surface
        Using Contact Angle Measurements," *Japanese Journal of Applied Physics,* vol.
        33, p. 6508, 1994.

[11]   C. W. Dyck, J. H. Smith, S. L. Miller, E. M. Russick, and C. L. J. Adkins,
        "Supercritical carbon dioxide solvent extraction from surface-micromachined
        micromechanical structures," in *Micromachining and Microfabrication '96*, 1996, p.
        11.

[12]   A. C. Fischer-Cripps, *Introduction to Contact Mechanics*: Springer New York, 2000.

[13]   J. J. Kim and S.-K. Kim, "Optimized surface pretreatments for copper
        electroplating," *Applied Surface Science,* vol. 183, pp. 311-318, 2001/11/28/ 2001.

[14]   N. V. Parthasaradhy, *Practical electroplating handbook*: Prentice Hall PTR, 1989.

CHAPTER 5: RESULTS

5.1 Top Electrode Outcome

The main purpose of this work was to fabricate and evaluate the performance of MEMS Acoustic Emission (AE) sensors. In Chapter 3, the design and simulation of MEMS AE sensors were elaborated, followed by discussion of the device microfabrication processes in Chapter 4. Among all the fabrication steps, the top electrode deposition and its release process are the most challenging and critical step for achieving a functional AE sensor. In this chapter, the outcome for the two approaches for the fabrication of AE sensors will be detailed and compared.

5.1.1 Sputtered Molybdenum Top Electrode

In section 4.6.1, the fabrications condition for AE devices with sputtered molybdenum top electrode before the release step was described. However, the built-in residual stress of the sputter deposited molybdenum microstructures are deemed to be problematic. Figure 45 illustrates the release process for the top electrode of AE sensors when sputtered molybdenum is used as the structural material. Figure 45a shows a device before the release process, while Figure 45b shows the partially released device after a SiO2 wet etching step. It can be seen that the top electrodes are starting to bend due to the intrinsic stress of the sputter deposited molybdenum layer. Figure 45c shows fully released device where the stress level causes some delamination of some of the released top electrode microstructures.

Some prior studies have been able to control the stress in sputtered Molybdenum thick films by a post-process annealing [1] or using low-pressure sputtering conditions[2]. In this work, initially several annealing temperatures were tried to reduce the stress level of the sputtered Molybdenum, but as can be seen in Figure 46a and 46b, the annealing process under atmospheric conditions not only oxidized the Molybdenum but also didn't solve the residual stress problem completely.
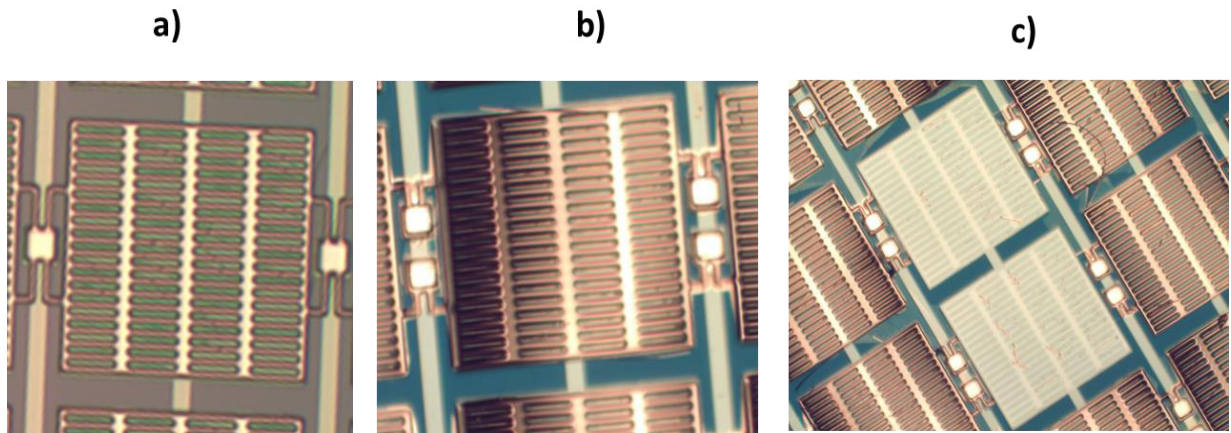
Figure 45. Micro-fabricated device with Mo top electrode after release process. The SiO2 sacrificial layer is etched away by wet etchant.

Subsequently as a new attempt to reduce the built-in residual stress of the sputter deposited Mo layer, the sputtering pressure conditions were changed from 5 mTorr to 3 mTorr, which is the lowest level of pressure that the AJA ORIN 5 sputtering system can be programed. The yield of the top electrode after release improved and the bending was no longer visible under a microscope, but several structures still delaminate after the wet etching of SiO2. Based on prior work by Cuthrell et al., a lower sputtering pressure near 1 mTorr could accomplish a near zero stress level[2].
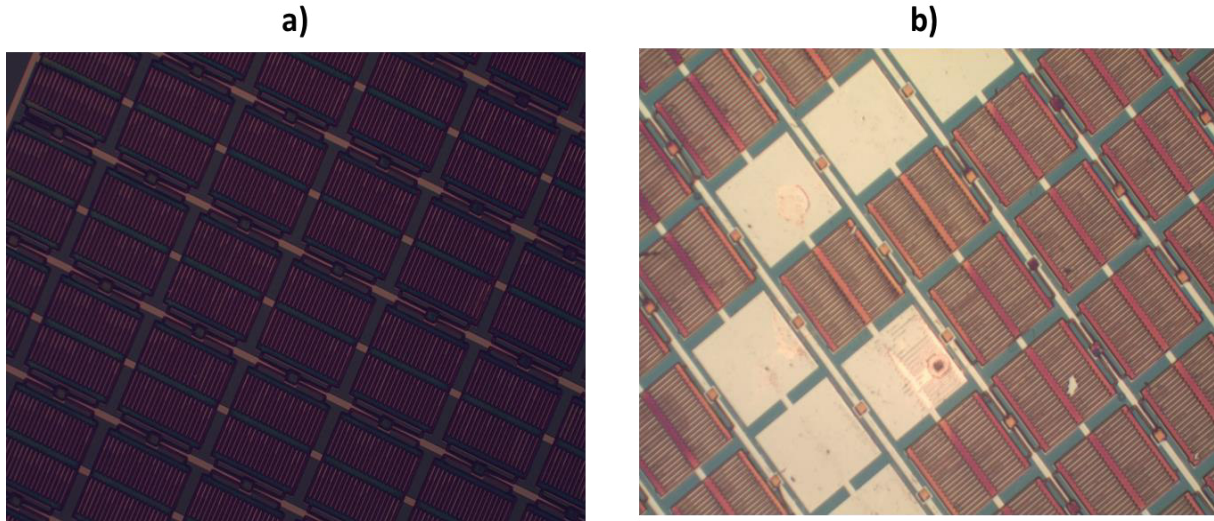
Figure 46. Top-view photos of AE devices after annealing of the Molybdenum top-electrode layer. a) Annealed top electrode before wet release; and b) Annealed top electrode after wet release.

5.1.2 Electroplated Nickel Top Electrode

As opposed to the sputtered Molybdenum, the electroplated Nickel under the process conditions described on section 4.6.2 assured a low-stress deposition. Consequently, this was the fabrication approach selected. Figures 47and 48 present the CAD designs and top-view microscope photos of the fabricated top electrodes for different aspect ratio (AR) and different resonance frequencies.

Figure 49a and 49b shows SEM photos of an array of Acoustic Emission (AE) sensor and the approximated final dimensions of one of the devices with 15:1 perforation aspect ratio are also presented. On the other hand, Figure 50 illustrates the device thickness profile and vertical/lateral dimensions of the fabricated device. There is visible distortion from the designed straight/vertical sidewall profile and the originally 10-µm lateral gap spacing. Those alterations are a direct consequence of the alterations in geometry owing to the patterned photoresist molding and electroplating process,

91

specifically when the photoresist mold requires a hard baking above its reflow temperature and further deformation during the nickel electroplating process.
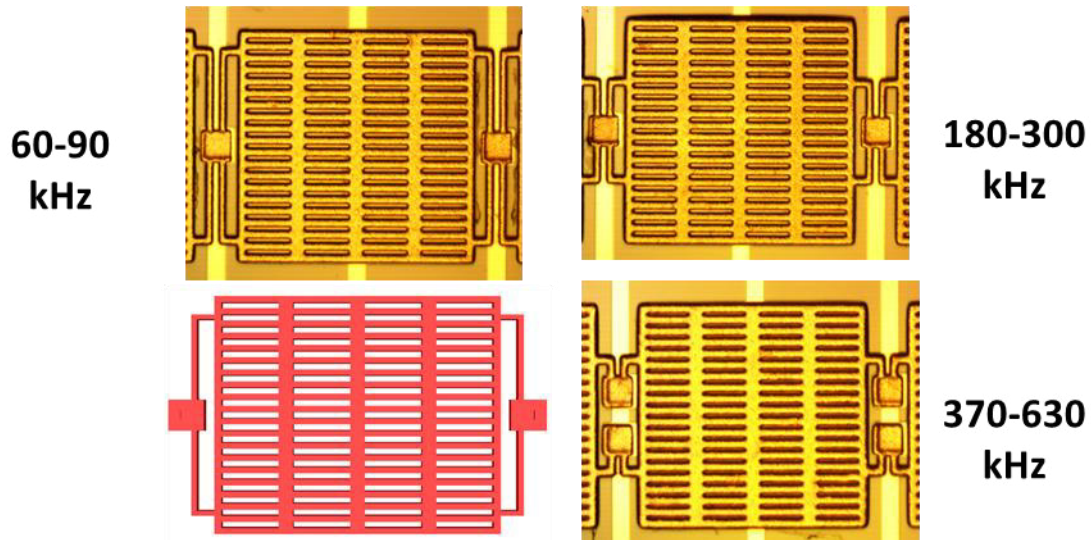
Figure 47. Top electrode designs (CAD layout) and top-view photos microfabricated AE sensors with different resonance frequencies.

5.2 Performance Evaluation of the MEMS Acoustic Emissions Sensor

To evaluate the performance of the MEMS AE sensor, a basic electrical test must be conducted. Figure 51 illustrates the implementation of two test fixtures. Initially, using fixture configuration number 1, a connection between the pads for a top electrode at left and right of the die must be checked to present a short circuit. The same check is conducted for the bottom electrode. This test is performed to verify the integrity of the thin metal lines that connect the pads and the electrodes.

Then, fixture configuration number 2 is used to verify that there is an open circuit between the top and bottom electrodes. And the capacitance between them can be

roughly measured a by using an LCR meter. Usually, the experimental capacitance lies

between 250 pF to 480 pF that matches with the designed values quite well.
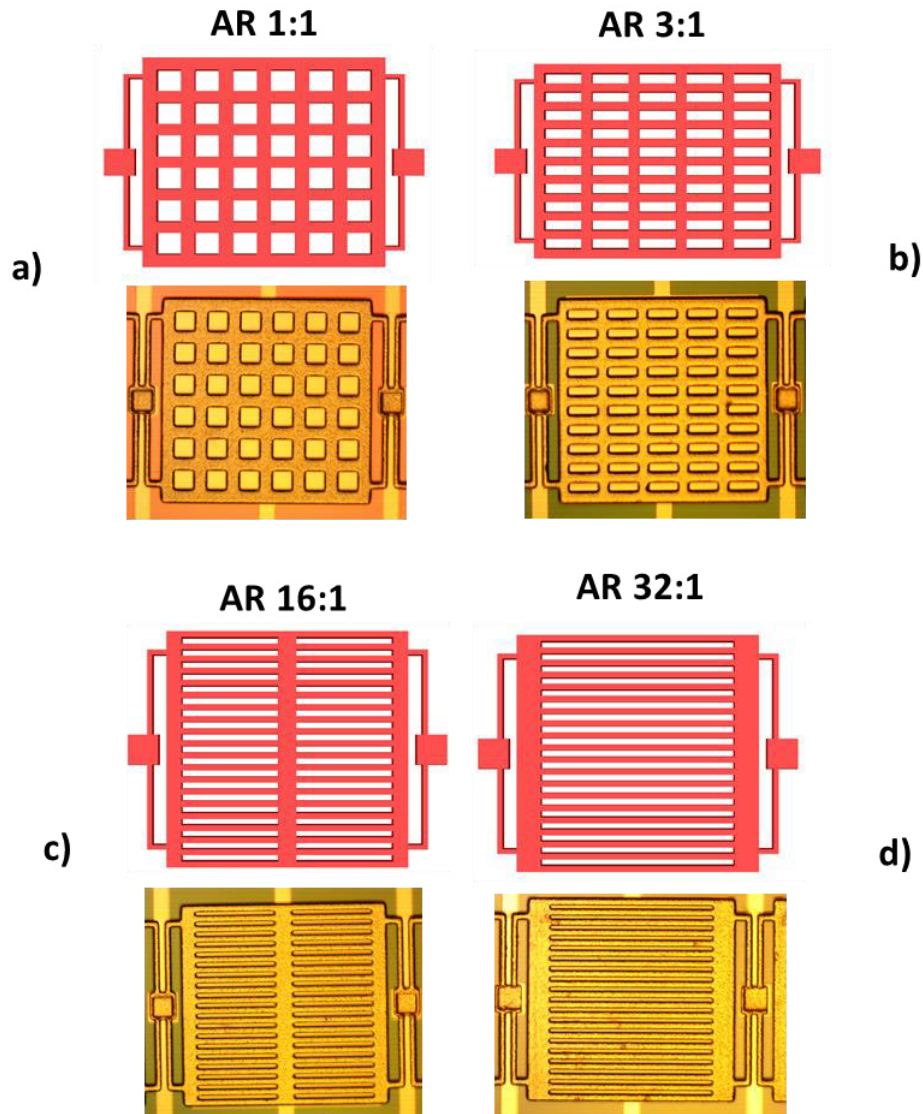
Figure 48. Top electrode designs (CAD layout) and top-view photos microfabricated AE sensors with different perforation AR's.

An additional functionality test is then conducted by performing capacitance-voltage or C-V measurement that measures the capacitance of the device while a varied DC voltage is applied between the top and bottom electrodes. Figure 52 presents the measured C-V characteristics of one of the fully released capacitive MEMS AE sensor

devices. As shown, the measured capacitance increases as the bias voltage increases between the bottom and a top electrode, thus causing the capacitive gap between them to decrease due to the generation of the electrostatic force.

a)

b)
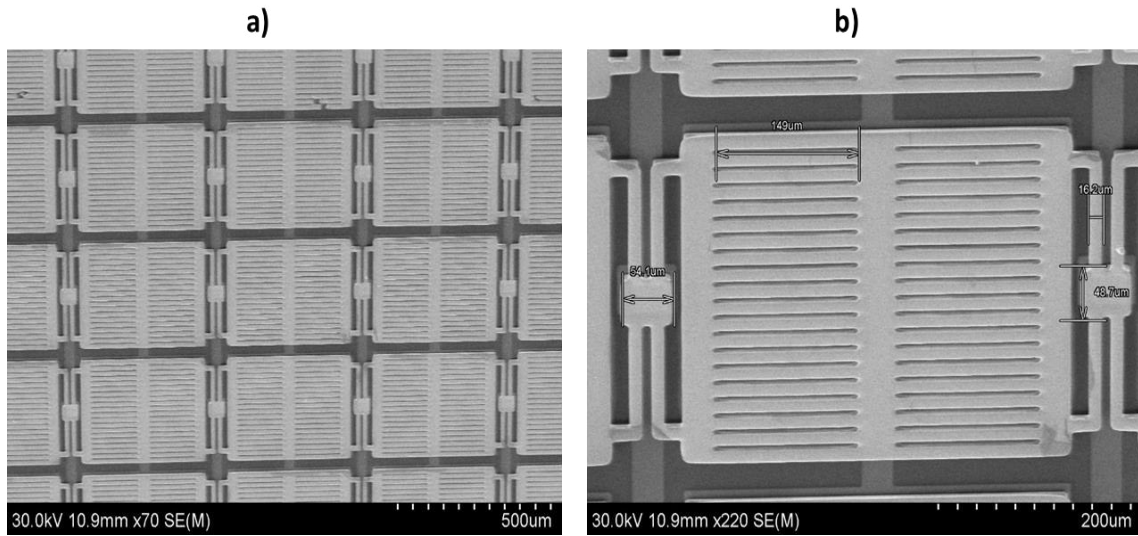
Figure 49. Zoom-out and zoom-in top-view SEM images. a) An array of AR 15:1 AE sensor devices; and b) measured key lateral dimensions of one device with perforation aspect ratio (AR) of 15:1
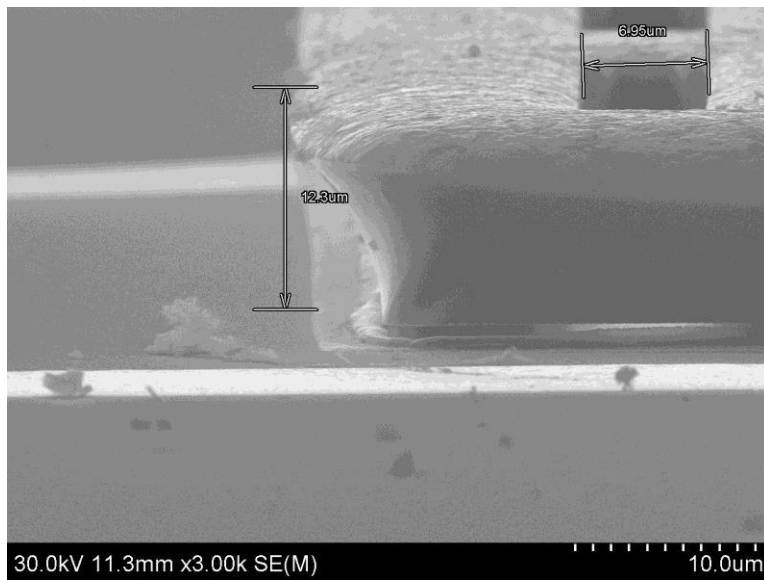
Figure 50. Schematic-view SEM image of a fabricated AE sensor device. It shows its structure, thickness profile, and a key lateral dimension.
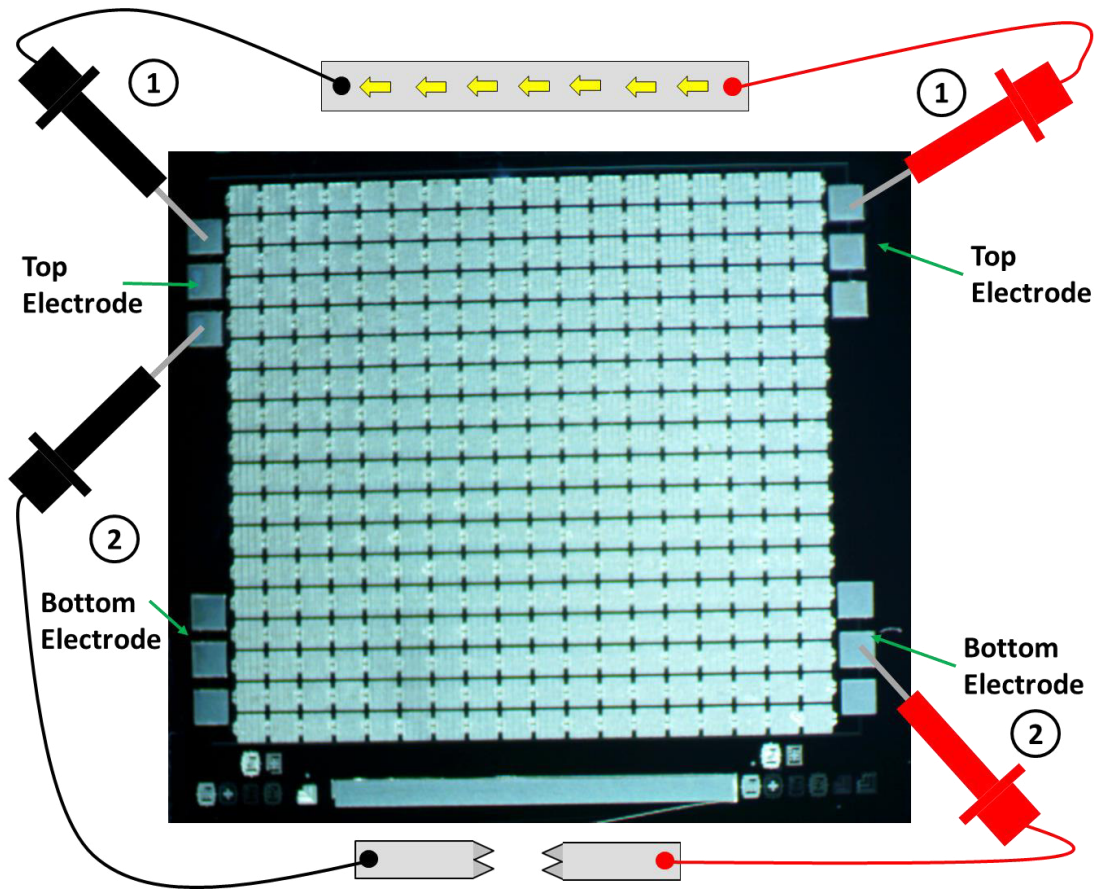
Figure 51. Basic electrical test fixture.

Once the initial electrical test and verification steps are done, the device is taken to a probe station under a test configuration shown in Figure 53. Basically, the top electrode is biased using a Hewlett Packard E3620A power supply, while the bottom electrode is the DC grounded with its AC output goes to a readout circuit and data acquisition unit (i.e. 1283 USB AE node), which is a single channel acoustic emission digital signal processor. This highly specialized AE sensor data acquisition unit can accept single-ended or differential AE sensor output, it also has a built-in internal preamplifier as well as analog and programmable digital filters. Then the specialized software AEwinTM is used for real-time waveform processing and analysis.

95
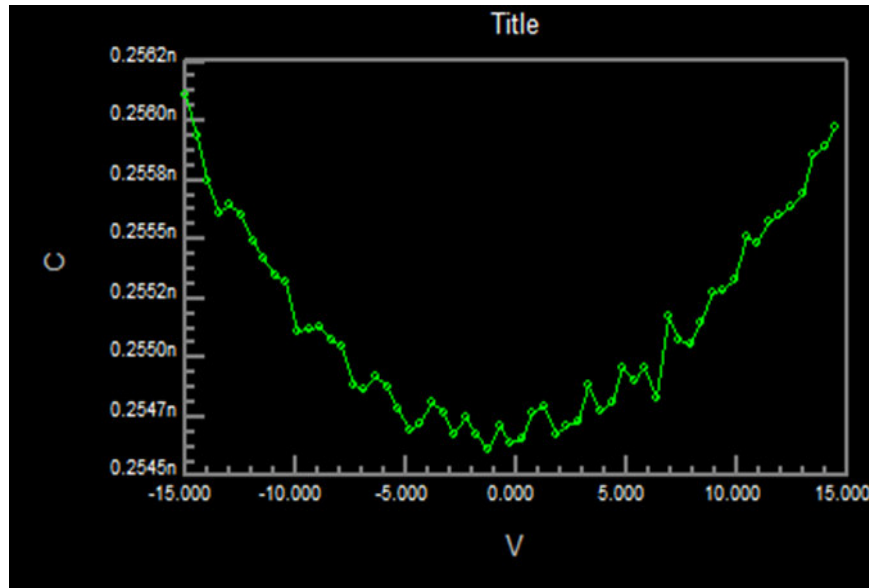
Figure 52. Measured C-V response of one of the fully released capacitive MEMS AE sensors.
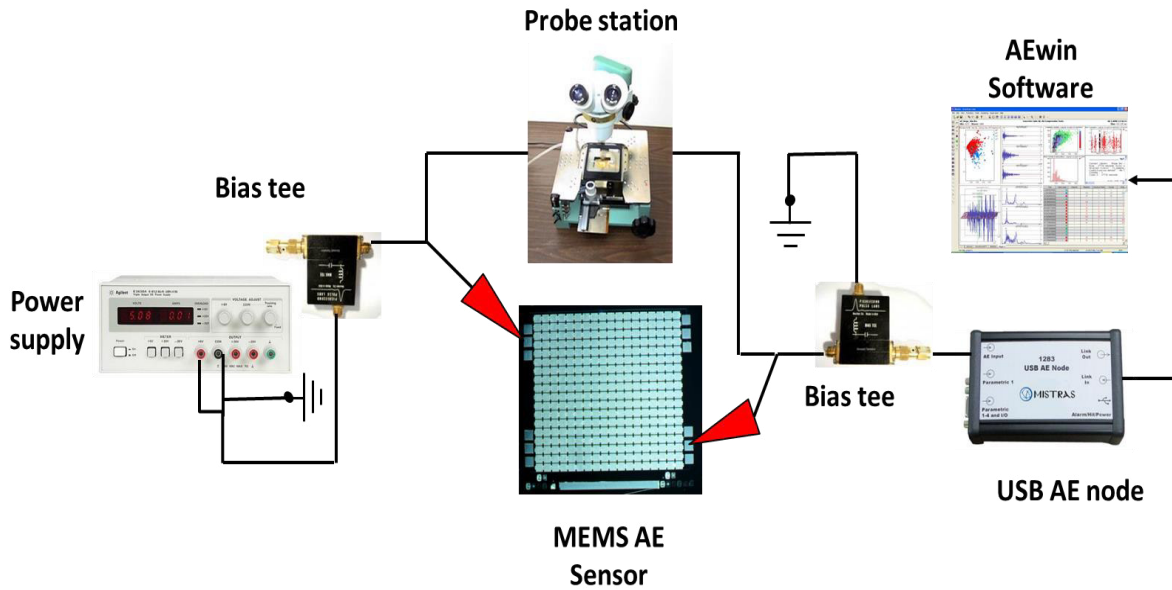
Figure 53. Capacitive MEMS AE sensor testing setup showing its key biasing/readout circuits.

To evaluate the MEMS acoustic emission sensor, an artificial AE signals source is required. Ideally, the AE source should produce a standard acoustic emission in the form

of a short duration pulse with controllable amplitude, at an arbitrarily location [3]. The typical standard acoustics emission sources include electrically driven ultrasonic transducer, a pencil lead break, a gas jet, spark impact, ball impact, a capillary break, between others [4], [5]. Between them, the ball impact source has the advantage that the absolute amplitude of the seismic waves can be associated with the momentum of the ball, that is a function of its mass and drop height.

Figure 54 depicts the acoustic emission testing setup where a ball drop testing fixture is used to generate artificial AE signals. A small steel ball is dropped from a fixed height at less than 2 inches distance away from the acoustic emission sensor, and the induced capacitive MEMS AE senor signals are recorded by the USB 1283 USB AE node and the AEwinTM software for further analysis.
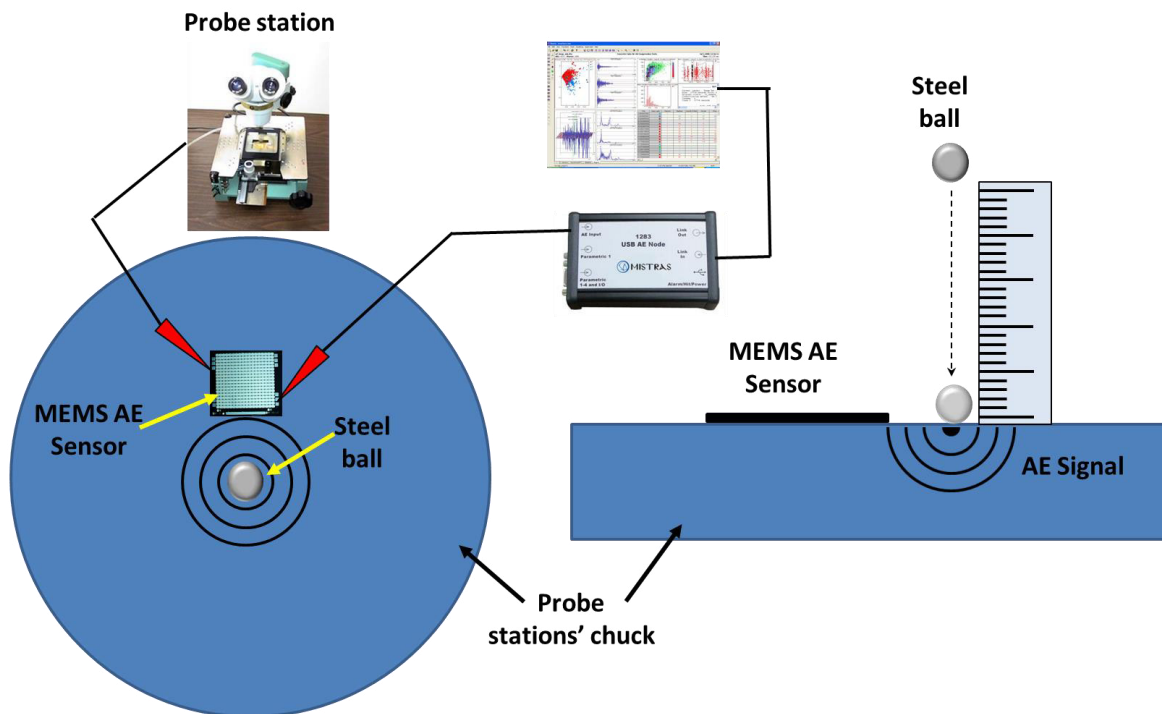
Figure 54. Capacitive MEMS AE sensor testing setup equipped with a ball dropping fixture for artificial AE signal generations.

97

5.2.1 Testing of the MEMS AE Sensor

Initially, the AE acquisition system setup is created by defining the acoustic emission parameters and the detected real-time waveform plots. The setting of the timing parameters, such as Peak Definition Time (PDT), Hit Definition Time (HDT) and Hit Lockout Time (HLT) are not critical for most regular AE tests, and the recommended default values were used. The PDT that measures the rise time was set to 200 μsec, the HDT that defines when a hit has ended was set to 800 μsec and the HLT that defines a "dead time" after the end of a hit, was set to 1000 μsec. Additionally, the Max duration, which sets a limit to a maximum duration allowed for a hit, was set to 1000 μsec. Firstly, the threshold was set to 40 dB, but the amount of noise clearly shows that the probe station is not the ideal setup for characterizing this type of AE sensor device and a senor package must be designed and implemented to reduce the mechanical and electrical noise for the future work. Then to reject the ambient mechanical vibration noise, the threshold was set to 70 Db.

Using the acoustic emission parameters as described above, an R15A Alpha Series piezoelectric sensor is used as a reference device and connected in replacement of the MEMS AE sensor as shown in Figure 54. Then the steel ball drop tests were conducted for several times while recording the signals continuously. Figure 55 shows a 3D scatter plot that illustrates the acoustic emission (AE) hits, its arrival, and its amplitude during the test. Figure 56 shows the power spectrum of the signals while Figure 57 presents the time domain waveforms of the AE event. The same test is performed with the capacitive MEMS AE sensor connected as shown in Figure 53. The same real-time AE signal plots are presented in Figures 57, 58 and 59.

There is a notable difference in the dynamic response of the two kinds of sensors, is evident that the squeeze film damping of the capacitive devices is limiting its ringing behavior. On the other hand, there is also a difference in the frequency spectrum of the studied sensors. Initially is important to highlight that the USB 1283 USB AE node uses an analog passband filter that attenuates any undesired signal outside of the range between 100 to 600 kHz. Comparing figures 55 and 58 is noticeable that there is a more resonant response in piezoelectric sensor around its 150 kHz resonant frequency, while the MEMS AE sensors are showing and wider band signal but with lower power levels. This behavior can be explained by the fact that the resonant frequencies are highly influenced by the thickness of the top electrode structure, and the devices tested in this work have a thickness around ten μm and then a resonant frequency below a 100 KHz.
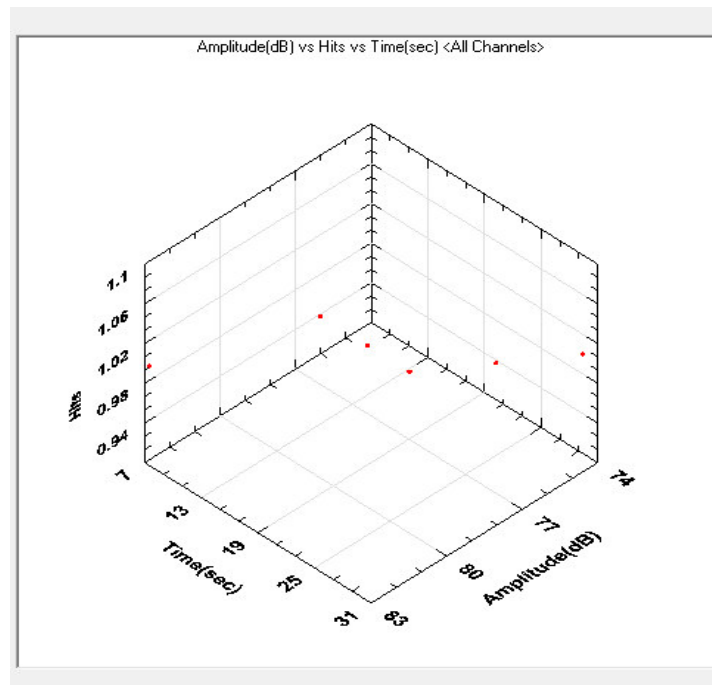
Figure 55. Amplitude (dB) vs hits vs time (sec) of the R15A piezoelectric sensor.
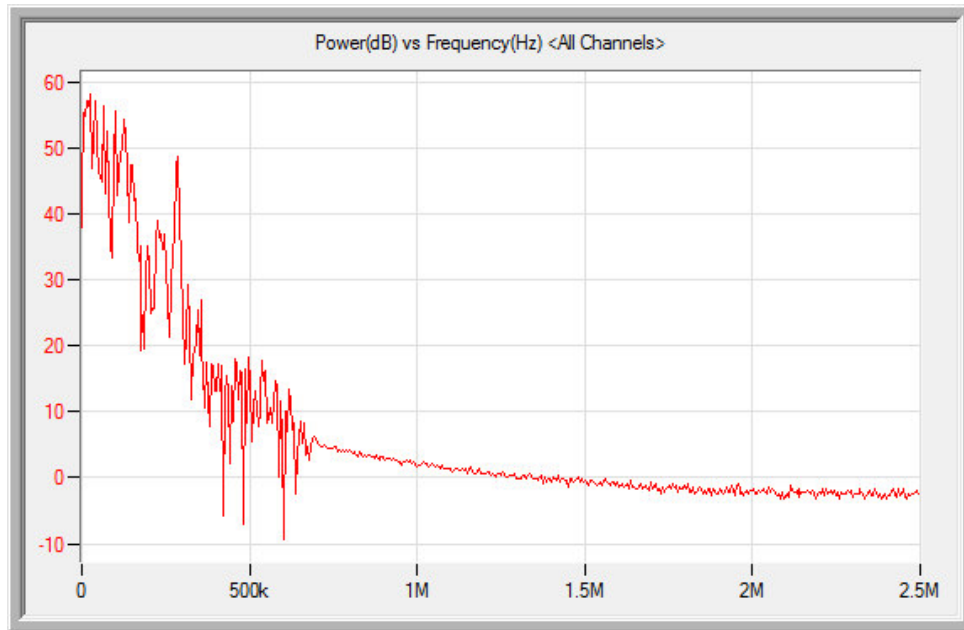
Figure 56. Power spectrum plot of the R15A piezoelectric sensor.
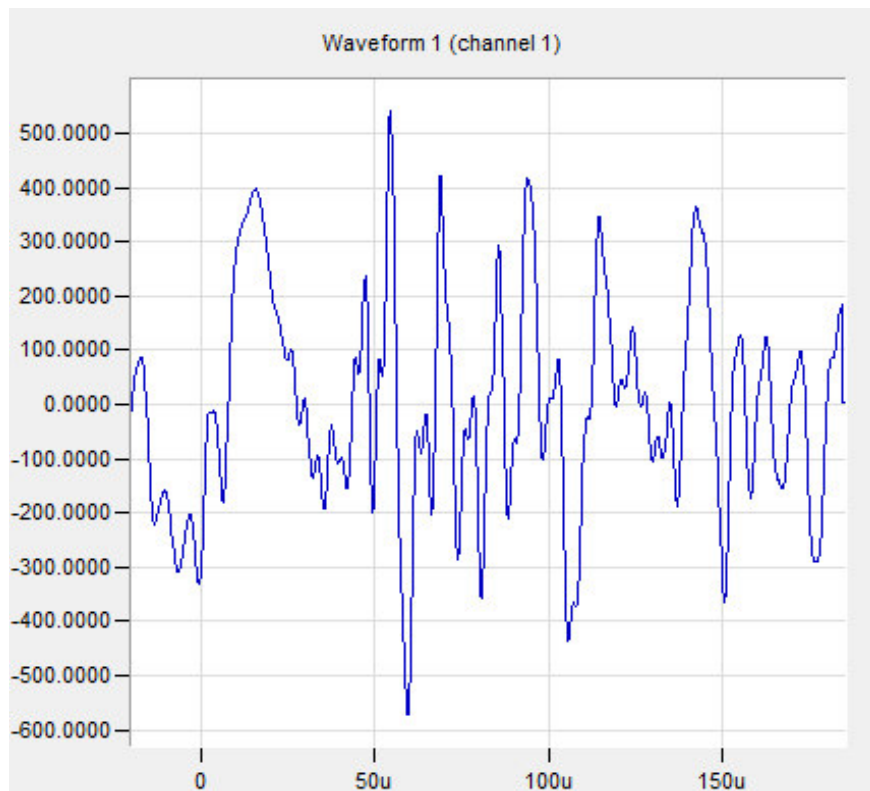
Figure 57. Voltage (mVolts) vs. time (sec) waveform of the R15A piezoelectric sensor.

100
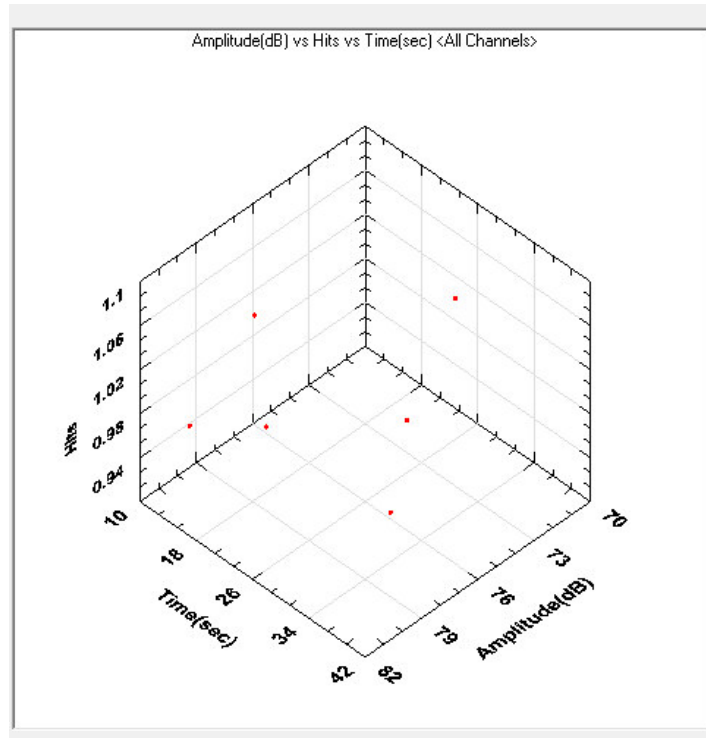
Figure 58. Amplitude (dB) vs. hits vs. time (sec) of one of the MEMS AE sensors
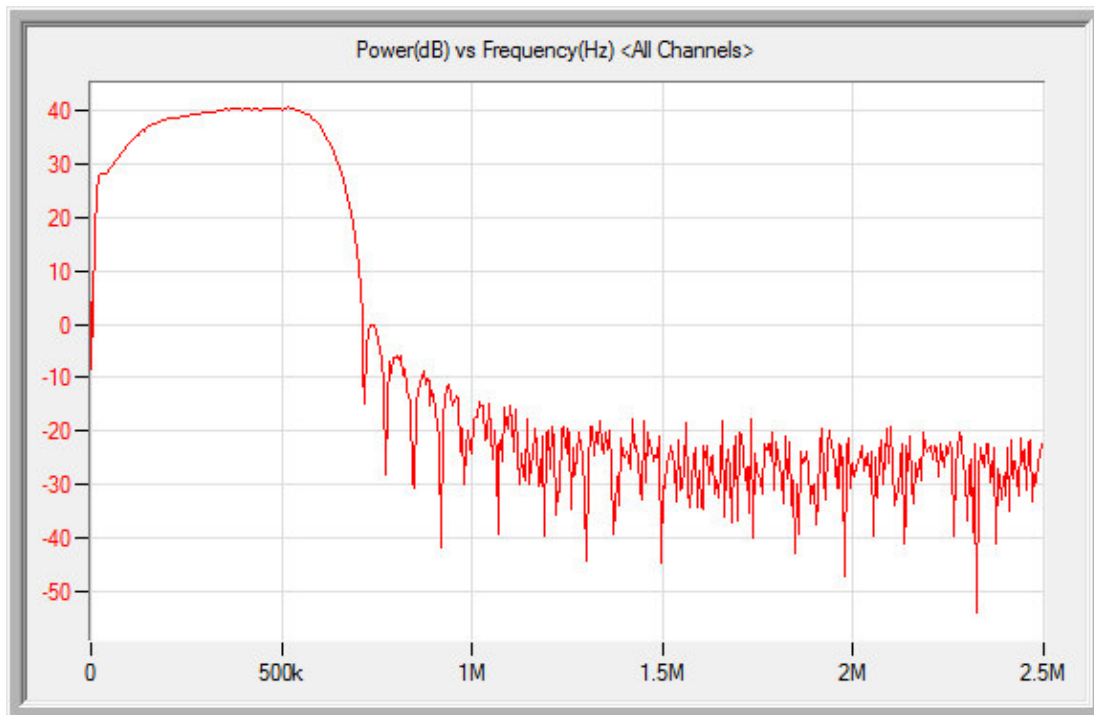
Figure 59. Power spectrum plot of one of the MEMS AE sensor

101
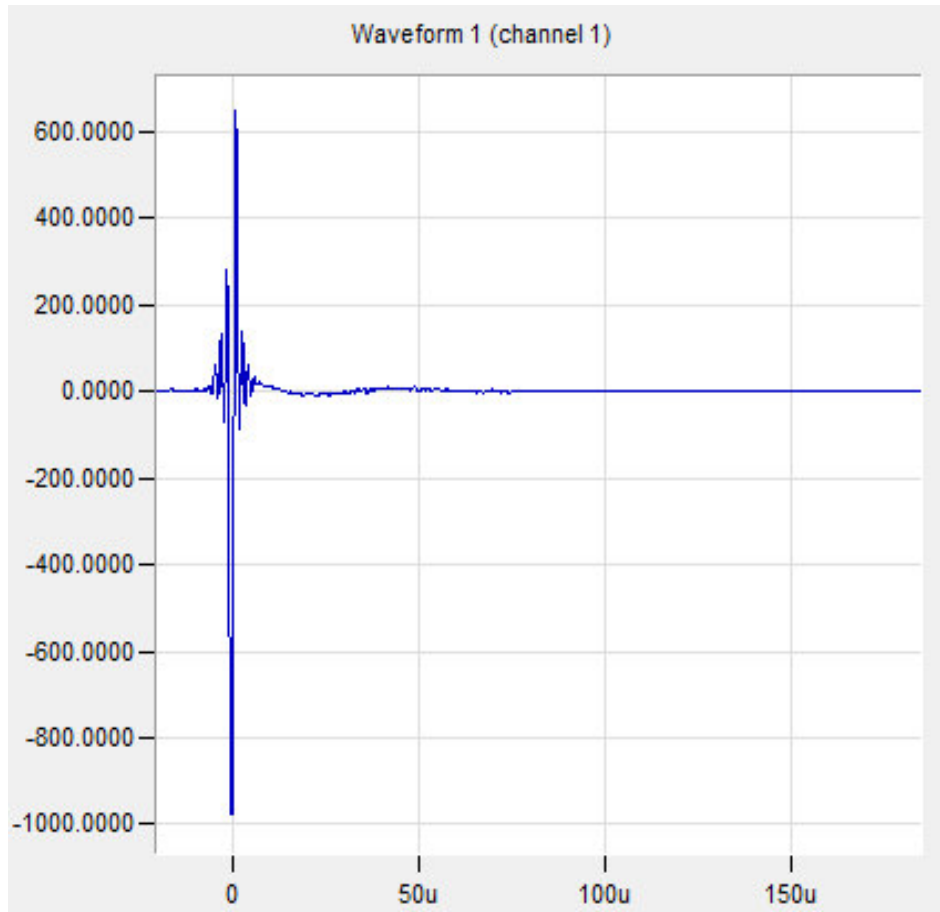
Figure 60. Voltage (mVolts) vs. time (sec) waveform of the MEMS AE sensors

One of the main tasks of this work is to explore how the damping is affecting the performance of the MEMS AE sensor compared with commercial AE sensor. As was stated in chapter 3, to study the damping effect on MEMS AE sensors a top electrode open grill geometry was modified to generate five MEMS AE sensors designs with different perforation aspect ratios. These designs were fabricated as was explained in chapter 4 and experimentally tested as described above. To compare the performance of the commercial AE sensor and the MEMS AE sensor the following parameters were measured:

• The number of Counts or the times that the signal crosses the demarcated trigger threshold.

• Duration is the time difference among the first threshold crossing and the last one.

• Energy or MARSE energy (Measured Area under the Rectified Signal Envelope).

• Amplitude is the highest measured voltage in a waveform.

• Strength is the integral of the rectified voltage signal over the duration of a hit.

• Absolute Energy, The integral of the squared voltage signal above the threshold divided by the reference resistance during a hit.

• SNR or Signal to Noise Ratio.

• Q, or quality factor related to the squeeze damping.

These acoustic emission parameters were selected because are closely related to the signal waveform shape and are typically used to filter out unwanted signal or for post-processing analyses. Between them, the related energy parameters (Energy, Absolute Energy and Strength) are interrelated with the area under the waveform envelope. Then the discrepancies in these parameter between the two types of sensors analyzed in this work could make a high impact in considering the signal a valid acoustic emission event and in the further analysis of the nature of the acoustic emission source.

In table 20 are summarized the simulated and experimental results for the designed MEMS AE sensors with different aspect ratios. Furthermore, in table 21 are presented the differences in the acoustic emission parameters for the designed devices and the commercial piezoelectric sensor (the data for the AR 32:1 couldn't be collected). The signal to noise ratio was calculated using equation 42 from chapter 3, and the Q

factor was calculated using the experimental ring down method (the details of this method are presented in Appendix C).

Table 20. Comparison of the simulated and experimental AE signals

AE sensor	Simulated Signal	Experimental signal
AR 1:1		
AR 3:1		
AR 8:1		

Table 20. (Continued)

Ar 16:1
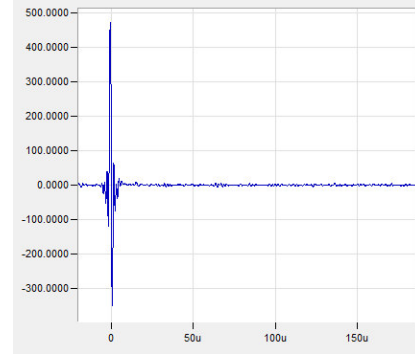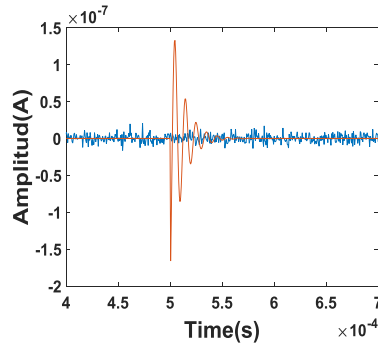
Table 21. Experimental AE parameters of the evaluated sensors.

AE sensor	R-150A	AR 1:1	AR 3:1	AR 8:1	AR 16:1
Counts	8	1	1	5	1
Duration (µs)	412	1	1	7	1
Energy (µV·s)	95	1	1	4	1
Amplitude (dB)	76	72	72	76	71
Strength (pV·s)	595E3	2.53	2.53	27E3	2.34E3
Absolute Energy (aJ)	153E3	700	700	12.4E3	747
SNR	16.2	14.3	14.3	22.16	16.7
Q	15	1.82	1.82	9.06	1.82

This result shows a close fit between the simulated and experimental results that evidence that the squeeze damping between the parallel electrodes is remarkably affecting the dynamic behavior of the device as an AE sensor. This statement is backed up by the AE parameters measurements that show that even that both types of sensors have a similar amplitude, the waveform related parameters are significantly different and

can lead to inconsistencies in AE data interpretation. In essence, the key parameters used to locate and characterize the AE sources, including hit counts, rise time, duration and energy content, can be distorted if the damping behavior of these types of transducers is not correctly tuned.

5.3 References

[1]   Y. G. Wu, E. H. Cao, Z. S. Wang, J. M. Wei, W. X. Tang, and L. Y. Chen, "Stress anisotropy in circular planar magnetron sputter deposited molybdenum films and its annealing effect," *Applied Physics A,* vol. 76, pp. 147-152, February 01 2003.

[2]   R. E. Cuthrell, D. M. Mattox, C. R. Peeples, P. L. Dreike, and K. P. Lamppa, "Residual stress anisotropy, stress control, and resistivity in post cathode magnetron sputter deposited molybdenum films," *Journal of Vacuum Science & Technology A: Vacuum, Surfaces, and Films,* vol. 6, pp. 2914-2920, 1988.

[3]   N. N. Hsu, "Acoustic emissions simulator," ed: Google Patents, 1977.

[4]   E. Longo and F. de Almeida La Porta, *Recent Advances in Complex Functional Materials: From Design to Application*: Springer International Publishing, 2017.

[5]   "ASTM E976-15, Standard Guide for Determining the Reproducibility of Acoustic Emission Sensor Response," ed. West Conshohocken, PA: ASTM International, 2015.

CHAPTER 6: CONCLUSIONS AND FUTURE WORK

This work was concentrated on the design, fabrication and preliminary testing of MEMS acoustic emission (AE) sensors based on capacitive transduction mechanism. A thorough modeling and simulation approach for out-of-plane capacitive MEMS acoustic emission transducers was systematically pursued by using finite element analysis (FEA) models with particular emphasis on their damping characteristics. Additionally, a second order equivalent mass-spring-damper model together with an electrostatic actuation was rigorously programmed using MATLAB/Simulink to evaluate the key parameters under study and to analyze the transient response of this transducer and the key performance limiting factors for several capacitive MEMS AE sensor designs as a detector of acoustic emission signals. To validate these simulation results, customized and highly versatile fabrication method was developed and performed to construct the designed capacitive MEMS AE sensors through a mass-manufacturing amenable process sequence. Then the newly designed MEMS AE sensor devices were tested using a dedicated commercial acoustic emissions signal acquisition module and software to evaluate its performance as AE sensor as compared with a commercial piezoelectric device.

6.1 Conclusions

After this dissertation research study the following conclusions were made:

- The bottom electrode fabrication was fabricated using lift-off technique using an undercut layer in a bi-layer lift-off process. This process is ideal for this purpose, but the

LOR thickness needs to be carefully defined. Because if the layer is too thick, it can generate short circuit problems between nearby electrode features. This is specifically critical when highly conformal depositions techniques such as sputtering is utilized. Moreover, three materials were studied in this work as a viable bottom electrode material, including Molybdenum, Platinum, and Ruthenium. All three of them have low resistivity, and adequate thermal expansion properties. But molybdenum have process compatibility issues when a long exposure to hydrofluoric acid or BOE etchants is necessary.

- Between the bottom and top electrodes, an insulation layer is required. The reason is that AE sensors have a large area, and there is a high probability that residues from the top electrode fabrication such as released or lift-off features, such as parts of the alignment marks, can land near or between the top and bottom electrodes to create a short circuit between them.

- The selection of the sacrificial material will define the releasing process of the suspended and perforated metal membrane as the top electrode of the capacitive MEMS transducers. This is one of the most critical steps in the entire fabrication process of a MEMS capacitive device since its choice will determine the nature of release method (i.e. wet or dry release). In this work, both release methods were studied using the two chosen sacrificial layer materials, which were plasma-enhanced chemical vapor deposited (PECVD) SiO_2 and photoresist. Even though both methods have led to funcational devices, the use of photoresist as a sacrificial layer will require it to be heated beyond its reflow temperature to reduce stress concentration issue to prevent crack formation and delamination during the subsequent metal layer depositions or any other post-deposition heating step.

• Two approaches were studied for the top electrode microfabrication, including sputtered deposited Molybdenum thin film and nickel electroplating. The former was not successful due to the intrinsic stress generated during the Mo sputtering deposition. A higher vacuum deposition condition (1mTorr or below) will be needed to deposit stress-free Mo layer by using this fabrication technique. On the other hand, nickel electroplating process have been successfully demonstrated as a reliable and quick method for the fabrication of top electrode microstructure.

• To evaluate the functionality of the MEMS AE sensor, a basic electrical test must be conducted. A connection between the pads for a top electrode need to be checked to present a short circuit. The same test should done for the bottom electrode. This test is performed to verify the integrity of the thin metal lines that connect the pads and the electrodes. Additionally, a similar test need to be done to verify an open circuit condition between the top and bottom electrodes. , that there is The effective capacitance between the top and bottom electrodes needs to tested by a LCR meter. The measured capacitance for the proposed AE sensor designs should lie between 250 pF to 480 pF.

• There is a notable difference in the dynamic responses of the commercial and the MEMS AE sensor, the squeeze-film damping of the capacitive MEMS devices limits its ringing behavior. Meanwhile, there is also a difference in the frequency characteristics of the studied sensors. There is a detectable resonance response for the piezoelectric sensor around its 150 kHz resonance frequency, while the MEMS AE sensors showing a wider band signal but with lower signal power levels. This behavior can be explained by the fact that the resonance frequencies are highly influenced by the thickness of the released top electrode structure, and the devices tested in this work have a thickness

around 10 µm and a corresponding resonance frequencies below a 100 kHz, which is below the cutoff frequency of (outside the passband) the dedicated AE sensor data acquisition system.

There is a close fit between the simulated and experimental results that serve as a strong evidence that the squeeze-film damping between the parallel electrodes drastically affect the dynamic behavior of the capacitive MEMS device as an AE sensor. This statement is backed up by the measurements of the AE parameters that indicate that even though t both types of sensors have exhibited a similar amplitude, the waveform related parameters are significantly different and can lead to inconsistencies in AE data interpretation. In essence, the key parameters used to locate and characterize the AE sources, including hit counts, rise time, duration and energy content, can be distorted if the damping behavior of these types of capacitive MEMS AE transducers is not correctly tuned to precisely match with the commercial piezo transcuers.

To compare the performance of the commercial AE sensor and the MEMS AE sensors, acoustic emission parameters that are closely related to the signal waveform and typically used to filter out unwanted signal during post-processing analyses were selected. From the results, the following can be concluded on each parameter:

• Counts: the devices with designed perforation aspect ratio (AR) of 1:1, 3:1 and 16:1 had only one count, while the best design with perforation aspect ratio (AR) of 8:1 had rendered 5 counts. As a comparison, the commercial sensor picked up 8 AE counts for the same input signal by the ball-drop test. The squeeze-film damping of MEMS AE sensors still caused a slightly lower Q and more damped ringing characteristic, which could lead to these aforementioned AE signal discrepancies. But, it is quite plausible to

further improve the ambient Q of MEMS AE sensors to match that of the commercial piezoelectric transducers on the order of 15 or so by further optimizing the device perforation patterns and capacitive gaps spacing.

- Duration: All the devices showed a considerable short duration (between 1 to 7 µs) as compared to 412 µs of the commercial sensor. Depending on the type of flaw that the AE analysis is target for in its monitoring task, the short duration can be adjusted by a filtering parameter during post-processing analysis.

- Amplitude: The commercial AE sensor and the MEMS AE sensor showed a similar and quite comparable amplitude when responding to the same signal input.

- Energy, Strength and Absolute Energy are AE parameters used to measure the signal impact energy and they are usually used to identify the type of wave source. All the capacitive MEMS AE devices acquired a very low energy content from the input signal, which can lead to wrong interpretation of the signal source.

It is important to highlight that even though the damping characteristics have a strong influence on the differences in the device behavior based on the captured AE parameters.These differences can be mitigated by setting a higher threshold value during the experiments. If a better insulation of the environmental noise can be achieved most likely from a well packaged sensor that enable direct testing of a packaged sensor without the usage of a probe station, the difference can be decreased. Overall, it is anticipated that the capacitive MEMS AE sensors based on the proposed device configuration with further optimized designs of perforation patterns and capacitive gap spacing to reduce squeeze-film damping can result in AE performance on par with commercial bulky piezo-ceramic AE transducers.

111

6.2 Future Work

The traditional piezo-ceramic AE sensors have a high footprint that makes it difficult to be embedded in structures and costly (a single unit price between $300 and $500), thus preventing high-volume installation and continuing structural health monitoring. On the other hand, Micro-Electro-Mechanical-Systems (MEMS) technologies have the potential to enable mass-production of miniaturized, narrowband, acoustic emission transducers at low cost, which cannot be achieved using conventional bulk piezoelectric materials. Additionally, a MEMS AE sensor could have an electronic integration with amplifiers and antenna for remote monitoring, and more importantly, its small size could remove the aperture problem that exist between the size on the commercials piezoelectric sensors and the input signal wavelength. Several micro-machined AE sensors could be fabricated on the same chip and if they are designed for different resonance frequencies as an AE sensor array. Hence, it will be possible to detect acoustic emission signal at different frequencies, improving the data analysis capabilities to filter undesired noise signals and to have a better understanding of the source of the acoustic emissions events. Moreover, if a capacitive transduction mechanism is used, then AE sensors could be used even under harsh environments (high temperature or corrosive environments) that cannot be accessed by the current sensor technology.

The Capacitive MEMS AE sensor still has plenty of room for improvements. Based on the presented work, the following are the suggestions by the author:

- To improve the dry release method and the top electrode patterning, a better sacrificial layer needs to be used. According to some of the latest preliminary test results

LOR seems to be an interesting alternative, which can be readily removed by wet release without the need of harsh acids.

- The amount of ambient noise pick up by the probe station indicated that it is not the ideal setup for testing the AE responses of the capacitive MEMS AE sensors. A better insulation from the environment to reduce the mechanical noise must be exploited along with a strategically designed package that help to reduce the electrical noise while keeping a suitable acoustic impedance with the analyzed materials. With a fully packaged MEMS AE sensor, direct mounting with an ideal coupling material to the material/structure under test can be performance to allow minimal ambient mechanical noise influence.

- To improve the damping conditions of the devices, the use of vacuum, new geometries, and properly designed gap distances should be explored, to achieve better AE signal levels. The damping should be tuned to guarantee that the MEMS AE sensor acquires the same AE parameter specific information identical to that of the commercial piezo-ceramic AE transducers.

APPENDIX A: COPYRIGHT PERMISSIONS

The permission below is for the use of Figure 2

Dear Adrian,

please find attached pictures of transient and continuous signal together with the data in text-file (picture shows only excerpt on time-scale).
Hope this helps.

Best regards
Herbert

--

Herbert Karzel
Sales
****
Vallen Systeme GmbH, Schäftlarner Weg 26a, 82057 Icking, Germany
Phone: +49 8178 9674-400   sales@vallen.de
****

Von: Adrian Avila [mailto:aeavila@mail.usf.edu]
Gesendet: Donnerstag, 27. April 2017 20:53
An: Vallen/Sales
Cc: gordon@atgndt.com
Betreff: Re: Requesting permissions to use copyright content

114

The permission below is for the use of Figure 3

Re: Requesting permissions to use copyright content   Inbox   x

Boris Muravin boris@ndt.co.il <u>via</u> integritydiagnosticsltd.onmicrosoft.com
to me

Hello
You can use it.

Dr. Boris Muravin
Founder and CEO
Integrity Diagnostics Ltd.
Mobile: <u>+972 544865557</u>
<u>www.ndt.co.il</u>
<u>www.idinspections.com</u>

------ Original message------
From: Adrian Avila
Date: Tue, Apr 11, 2017 06:25
To: <u>boris@muravin.com</u>;
Cc:
Subject: Requesting permissions to use copyright content

Hi Dr. Muravin,

I am writing my Ph.D. dissertation and I would like to use the following figure from the you AE web page content:
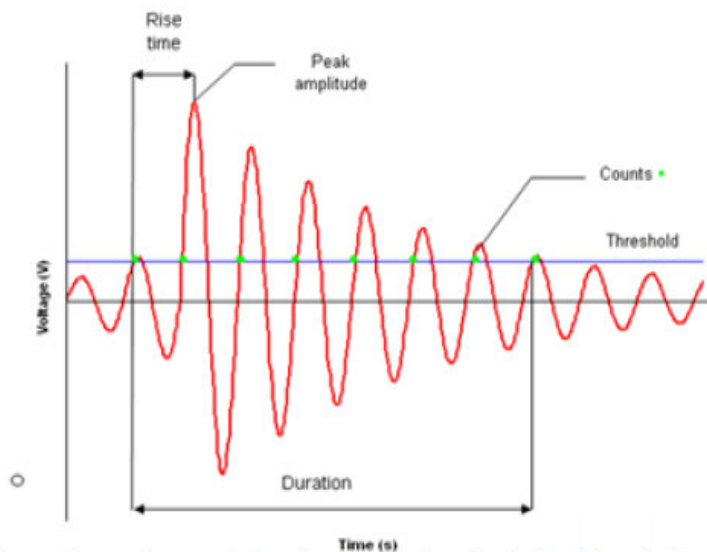
I want to use it as part of my background content. Could you help me with this, please?

Best regards,

115

The permission below is for the use of Figure 3

The permission below is for the use of Figure 5

The permission below is for the use of Figure 6

Copyright Clearance Center

RightsLink®

Home | Account Info | Help | ✉

IEEE

Requesting permission to reuse content from an IEEE publication

Title: Characterization and Noise Analysis of Capacitive MEMS Acoustic Emission Transducers

Conference Proceedings: Sensors, 2007 IEEE

Author: Wei Wu

Publisher: IEEE

Date: Oct. 2007

Copyright © 2007, IEEE

Logged in as:
Adrian Avila
Account #:
3001138152

LOGOUT

Thesis / Dissertation Reuse

The IEEE does not require individuals working on a thesis to obtain a formal reuse license, however, you may print out this statement to be used as a permission grant:

Requirements to be followed when using any portion (e.g., figure, graph, table, or textual material) of an IEEE copyrighted paper in a thesis:

1) In the case of textual material (e.g., using short quotes or referring to the work within these papers) users must give full credit to the original source (author, paper, publication) followed by the IEEE copyright line ◊ 2011 IEEE.
2) In the case of illustrations or tabular material, we require that the copyright line ◊ [Year of original publication] IEEE appear prominently with each reprinted figure and/or table.
3) If a substantial portion of the original paper is to be used, and if you are not the senior author, also obtain the senior author◊s approval.

Requirements to be followed when using an entire IEEE copyrighted paper in a thesis:

1) The following IEEE copyright/ credit notice should be placed prominently in the references: ◊ [year of original publication] IEEE. Reprinted, with permission, from [author names, paper title, IEEE publication title, and month/year of publication]
2) Only the accepted version of an IEEE copyrighted paper can be used when posting the paper or your thesis on-line.
3) In placing the thesis on the author's university website, please display the following message in a prominent place on the website: In reference to IEEE copyrighted material which is used with permission in this thesis, the IEEE does not endorse any of [university/educational entity's name goes here]'s products or services. Internal or personal use of this material is permitted. If interested in reprinting/republishing IEEE copyrighted material for advertising or promotional purposes or for creating new collective works for resale or redistribution, please go to http://www.ieee.org/publications_standards/publications/rights/rights_link.html to learn how to obtain a License from RightsLink.

If applicable, University Microfilms and/or ProQuest Library, or the Archives of Canada may supply single copies of the dissertation.

118

The permission below is for the use of Figure 8

119

The permission below is for the use of Figure 9

Copyright Clearance Center

RightsLink®

Home | Account Info | Help

ANNUAL REVIEWS

Title: PROCESSING AND CHARACTERIZATION OF PIEZOELECTRIC MATERIALS AND INTEGRATION INTO MICROELECTROMECHANICAL SYSTEMS

Author: Dennis L. Polla, Lorraine F. Francis

Publication: Annual Review of Materials Science

Publisher: Annual Reviews

Date: Aug 1, 1998

Copyright © 1998, Annual Reviews

Logged in as:
Adrian Avila
Account #:
3001138152

LOGOUT

Permission Not Required

Material may be republished in a thesis / dissertation without obtaining additional permission from Annual Reviews, providing that the author and the original source of publication are fully acknowledged.

The permission below is for the use of Figure 10

The permission below is for the use of Figure 11

122

APPENDIX B: ATOMIC LAYER DEPOSITIONS (ALD) RECIPES

Table B1 presents the program used by the Savanah Atomic Layer Deposition System to deposit 45 nm of Al_2O_3 thin film.

Table B1. Program steps for the deposition of Al_2O_3 thin film by the Savanah ALD tool.

	Instruction	#	Value
0	heater	9	200
1	heater	8	200
2	stabilize	9	
3	stabilize	8	
4	Wait	5	
5	Flow		20
6	Pulse	0	0.015
7	Wait	15	
8	Pulse	3	0.015
9	Wait	15	
10	goto	6	450
11	heater	9	150
12	heater	8	150
13	Flow		5

Table B2 show the program used the Savanah Atomic Layer Deposition System to deposit 45 nm of HfO_2 thin film.

Table B2. Program steps for the deposition of HfO_2 thin film by the Savanah ALD tool.

	Instruction	#	Value
0	heater	9	200
1	heater	8	75
2	heater	14	75
3	stabilize	9	
4	stabilize	8	
5	stabilize	14	
6	Wait	10	
7	Flow		20
8	Pulse	0	0.015
9	Wait	25	
10	Pulse	4	0.4
11	Wait	25	
12	goto	6	450
13	heater	9	150
14	heater	8	150
15	heater	14	0
16	Flow		5

APPENDIX C: RING DOWN METHOD TO CALCULATE DEVICE Q-FACTOR

Figure C1 presents a damped oscillation waveform u(t), and its envelope amplitude decreases exponentially following the equation below:

$$u(t) = e^{-\frac{\omega}{2Q}t} \qquad \text{(C1)}$$

where U_0 is a constant equal to the maximum peak of the oscillatory waveform at $u(0)$, and Q is the quality factor. Then the time when u(t) equals to the half of the maximum value will be:

$$U_0 e^{-\frac{\omega}{2Q}t} = \frac{U_0}{2} \qquad \text{(C2)}$$

Using the natural logarithm function this expression will be simplified as:

$$\frac{\omega}{2Q}t = Ln(2) \qquad \text{(C3)}$$

If is considered that the number of cycles N in a period T is defined as $N=1/T$, then Eq. (C2) can be rewritten as:

$$\frac{1}{2Q}\frac{2\pi}{T}NT = Ln(2) \qquad \text{(C4)}$$
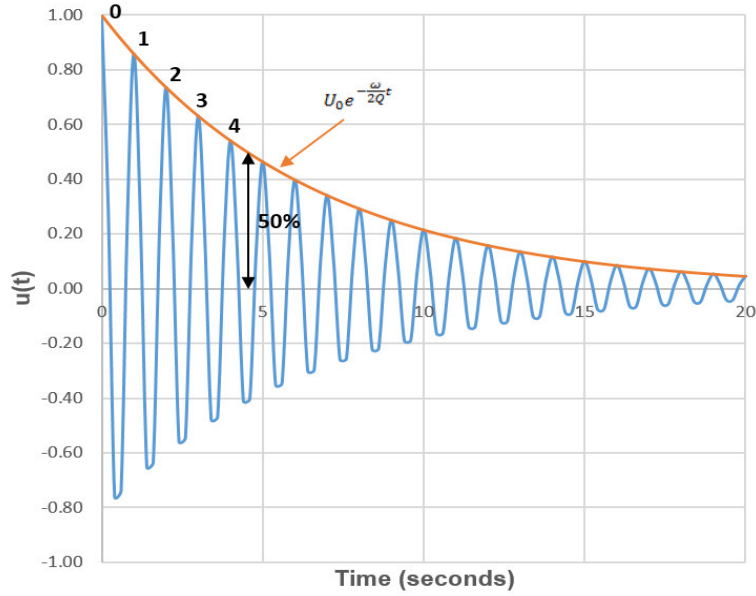
Figure C1. Envelope of a damped oscillation signal in its time-domain waveform.

By solving for Q, the following expression is obtained:

$$Q \cong 4.53N \tag{C3}$$

Using the methodology above, the Q factors for the experimental waveforms were
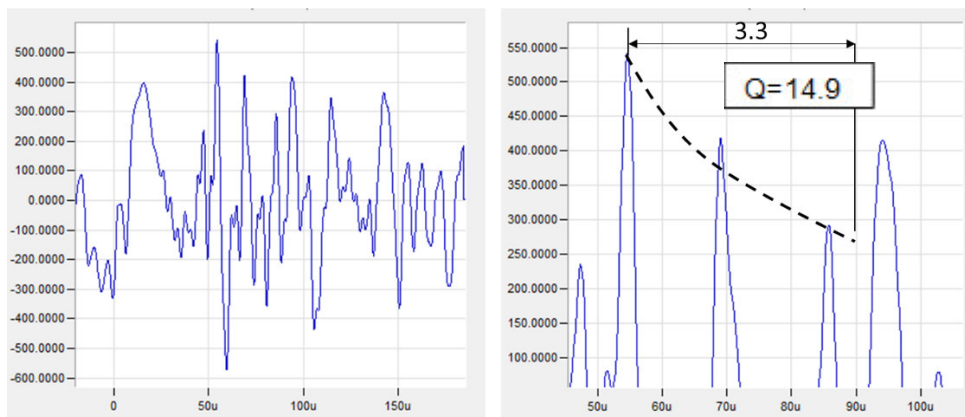
calculated as follows:

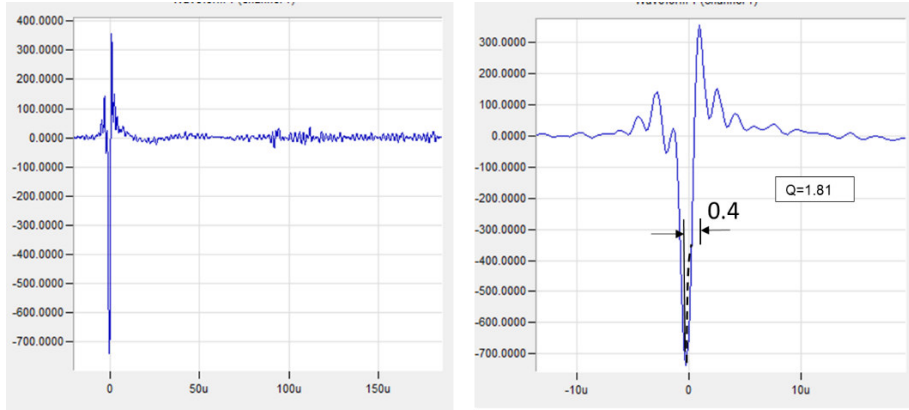Figure C2. Q factor for the R-150A AE sensor.

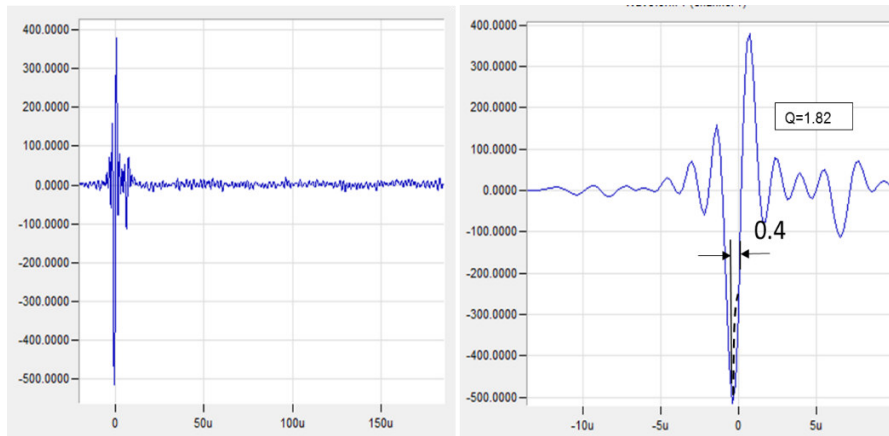Figure C3. Determination of the Q factor for the AR 1:1 AE sensor.

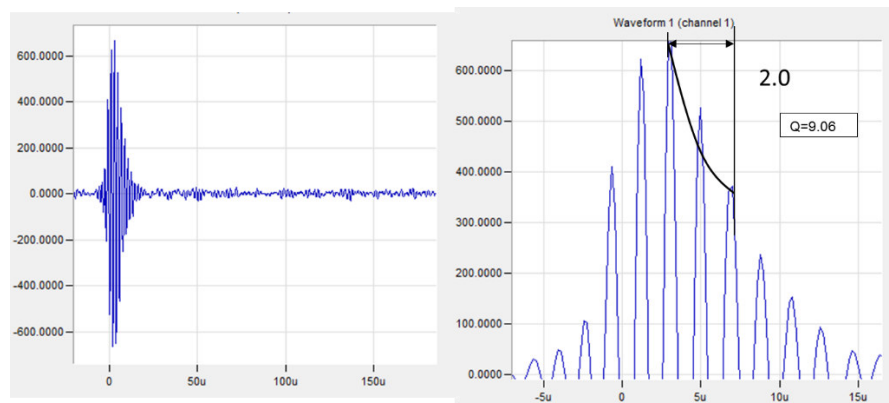Figure C4. Determination of the Q factor for the AR 3:1 AE sensor.

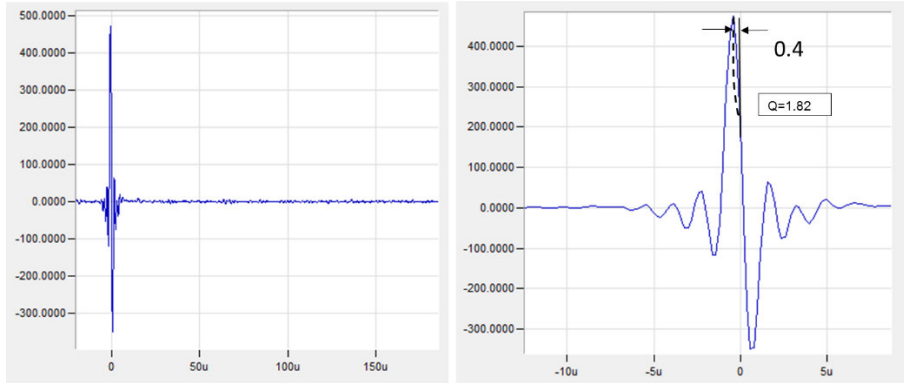Figure C5. Determination of the Q factor for the AR 8:1 AE sensor.

Figure C6. Determination of the Q factor for the AR 16:1 AE sensor.

APPENDIX D: FABRICATION PROCESS FOR THE PLATED NICKEL AE SENSORS

1) Samples cleaning

• A RCA cleaning is performed for newly acquired wafers.

• Solvent cleaning by Acetone, Methanol and Isopropanol can act as an alternative.

2) Bottom Electrode (Mask # 1)

2.1) UV Lithography for patterning LOR and AZ 1512

Spin: Laurell Spinner

LOR 3B: 40 sec @ 2500 RPM

Softbake: 8mim 30 sec @ 180°C

Spin: Laurell Spinner

AZ 1512: 40 sec @ 2500 RPM

Softbake: 50 sec @ 95°C

Exposure: 3.3 sec @ 9.6 mW/cm^2, hard contact

PEB: 50 sec @ 105°C

Develop: 25 sec in AZ 726

2.2) Descum

Equipment: Plasma Therm

O$_2$: 50 sccm

Pressure: 250 mTorr

Power: 50 watts

Time: 2 min

2.3) Chrome Deposition

Equipment: AJA Sputtering

Power: 100 watts RF

Pressure: 3 mTorr

Flow rate: Ar 12 sccm

Time: 14 min (~40 nm)

2.4) Ruthenium Deposition

Equipment: AJA Sputtering

Power: 100 watts RF

Pressure: 3 mTorr

Flow rate: Ar 12 sccm

Time: 33 min (~160 nm)

2.5) Lift-off

Submerge wafer in AZ 400T photoresist stripper heated at 60°C

Water cleaning in DI water

3) Insulation layer deposition

3.1a) Al_2O_3 deposition

Equipment: Savannah 200

Temperature: 200 °C

Number of Cycles: 450 (~45 nm)

3.1b) HfO_2 deposition

Equipment: Savannah 200

Temperature: 200 °C

Number of Cyces: 600 (~60 nm)

4) Sacrificial layer deposition

4.1a) SiO_2 deposition

Equipment: Plasma Therm

N_2O: 500 sccm

SiH_4: 110 sccm

Pressure: 500 mTorr

Power: 50 watts

4.1b) Photoresist deposition

Spin: Laurell Spinner

AZ 1512 spun for 40 sec @ 1000 RPM

Softbake: 50 sec @ 95°C

5) Anchor Lithography (Mask # 2)

5.1a) SiO2 Sacrificial layer

Spin: Laurell Spinner

AZ 1512 spun for 40 sec @ 1000 RPM

Softbake: 50 sec @ 95°C

Exposure: 7 sec @ 9.6 mW/cm^2, hard contact

PEB: 50 sec @ 105°C

Develop: 25 sec in AZ 726

5.1b) Photoresist Sacrificial layer

Exposure: 7 sec @ 9.6 mW/cm^2 with a hard contact

PEB: 50 sec @ 105°C

Develop: 25 sec in AZ 726

Hardbake: 2 min @ 200°C

6) Sacrificial layer etch (SiO2 only)

Solution: BOE 6:1

Submerge wafer in solution for 5 min

Rinse wafer with water and dry in N$_2$

Submerge wafer in acetone for 10 min

Solvent clean

7) Insulation layer etch

7.1a) Al$_2$O$_3$

Solution: BOE 6:1

Submerge wafer in solution for 1 min

Rinse wafer with DI water and dry by N$_2$

7.1b) HfO$_2$

Spin: Laurell Spinner

AZ 12XT 40 sec @ 3000 RPM

Softbake: 1 min @ 110°C

Exposure: 13 sec @ 9.6 mW/cm^2, hard contact

PEB: 1 min @ 95°C

Develop: 1 min in AZ 300

Descum: 2 min

Equipment: AMS 100, Alcatel Vacuum Technology

SF_6/Ar

Ar: 100 sccm

SF_6: 100 sccm

Power: 600 watts

Substrate temperature: 20 °C

Time: 8 min

Submerge wafer in acetone for 10 min

Solvent clean

8) Seed layer deposition

8.1) Titanium Deposition

Equipment: AJA Sputtering

Power: 150 watts RF

Pressure: 3 mTorr

Flow rate: Ar 12 sccm

Time: 8 min (~20 nm)

8.2) Copper Deposition

Equipment: AJA Sputtering

Power: 100 watts RF

Pressure: 5 mTorr

Flow rate: Ar 12 sccm

Time: 20 min (~200 nm)

Solvent clean

9) Top Electrode Deposition

9.1) Lithography AZ 12XT

Spin: Laurell Spinner

AZ 12XT spun for 40 sec @ 1500 RPM

Softbake: 1 min @ 110°C

Exposure: 26 sec @ 9.6 mW/cm2, hard contact

PEB: 1 min @ 95°C

Develop: 1 min in AZ 300

Descum: 2 min

9.2) Nickel electroplating deposition

Equipment: Nickel plating setup

Temperature: 50 °C

Current: 200 mA

Time: 60 min (~10 microns)

Submerge wafer in acetone for 10 min

Solvent clean

Water rinse

Dice the wafer into chip scale samples

9.3) Seed layer etch

9.3.1) Copper etch

Solution: 50:50 H_2O_2: NH_4OH

Submerge wafer in solution for 4 min

Rinse wafer with water and dry

9.3.2) Titanium etch

Solution: BOE 6:1

Submerge wafer in solution for 1 min

Rinse wafer with water and dry

10) Release

10.1a) Photoresist Sacrificial layer

Equipment: Plasma Therm (PE mode)

O_2: 200 sccm

Pressure: 500 mTorr

Power: 400watts

Time: 10000 sec

10.1b) SiO_2 Sacrificial layer

Solution: BOE 6:1

Submerge wafer in solution for 12 min

Rinse wafer with water and dry